Measurement of the Partial Branching Fraction for Inclusive Semileptonic B Meson Decays to Light Hadrons $B \to X_u l \nu$ and an Improved Determination of the Quark-Mixing Matrix Element $|V_{ub}|$

DISSERTATION

zur Erlangung des akademischen Grades
Doctor rerum naturalium
(Dr. rer. nat.)

vorgelegt
der Fakultät Mathematik und Naturwissenschaften
der Technischen Universität Dresden

von
Diplom-Physiker Alexei Volk
geboren am 16. Februar 1978 in Winogradnoje

Gutachter :

Abstract

This thesis presents an analysis of inclusive semileptonic $B \to X_u e\overline{\nu}_e$ decays using approximately 454 million $\Upsilon(4S) \to B\bar{B}$ decays collected during the years 1999 to 2008 with the BABAR detector. The electron energy, E_e, and the invariant mass squared of the electron-neutrino pair, q^2, are reconstructed, where the neutrino kinematics is deduced from the decay products of both B mesons. The final hadronic state, X_u, consists of a sum of many hadronic channels, each of which contains at least one u quark. The variables q^2 and E_e are then combined to compute the maximum kinematically allowed invariant mass squared of the hadronic system, $s_\mathrm{h}^\mathrm{max}$. Using these kinematic quantities, the partial branching fraction, $\Delta\mathcal{B}(B \to X_u l\nu)$, unfolded for detector effects, is measured to be

$$\Delta\mathcal{B}(E_e > 2.0\,\mathrm{GeV}, s_\mathrm{h}^\mathrm{max} < 3.52\,\mathrm{GeV}^2) = (3.33 \pm 0.18 \pm 0.21) \times 10^{-4}$$

in the $\Upsilon(4S)$ and

$$\Delta\tilde{\mathcal{B}}(\tilde{E}_e > 1.9\,\mathrm{GeV}, \tilde{s}_\mathrm{h}^\mathrm{max} < 3.5\,\mathrm{GeV}^2) = (4.57 \pm 0.24 \pm 0.32) \times 10^{-4}$$

in the B meson rest frames. The quoted errors are statistical and systematic, respectively. The CKM matrix element $|V_{ub}|$ is determined from the measured $\Delta\tilde{\mathcal{B}}$ using theoretical calculation based on Heavy Quark Expansion. The result is

$$|V_{ub}| = (4.19 \pm 0.18^{+0.26+0.26}_{-0.20-0.25}) \times 10^{-3},$$

where the errors represent experimental unceratinties, uncertainties from HQE parameters and theoretical uncertainties, respectively.

Kurzfassung

In dieser Dissertation wird eine Analyse von inklusiven semileptonischen $B \to X_u e\overline{\nu}_e$ Zerfällen präsentiert. Die Daten wurden in den Jahren von 1999 bis 2008 mit dem BABAR Detektor aufgezeichnet und entsprechen ungefähr 454 Millionen $\Upsilon(4S) \to B\bar{B}$ Zerfällen. Es werden die Energie des Elektrons, E_e, und das Quadrat der invarianten Masse des Elektron-Neutrino-Systems, q^2, rekonstruiert. Die Kinematik des Neutrinos wird aus den Zerfallsprodukten beider B-Mesonen abgeleitet. Der hadronische Endzustand, X_u, ist eine Summe aus vielen hadronischen Zuständen, von denen jeder mindestens ein u Quark enthält. Die Grössen q^2 und E_e werden zu einer weiteren Variable, $s_\mathrm{h}^\mathrm{max}$, kombiniert, die das Quadrat der invarianten Masse des hadronischen Systems darstellt. Mit Hilfe dieser kinematischen Grössen wird das folgende partielle Verzweigungsverhältnis, $\Delta\mathcal{B}(B \to X_u l\nu)$, gemessen:

$$\Delta\mathcal{B}(E_e > 2.0\,\mathrm{GeV}, s_\mathrm{h}^\mathrm{max} < 3.52\,\mathrm{GeV}^2) = (3.33 \pm 0.18 \pm 0.21) \times 10^{-4}$$

im $\Upsilon(4S)$- und

$$\Delta\tilde{\mathcal{B}}(\tilde{E}_e > 1.9\,\mathrm{GeV}, \tilde{s}_\mathrm{h}^\mathrm{max} < 3.5\,\mathrm{GeV}^2) = (4.57 \pm 0.24 \pm 0.32) \times 10^{-4}$$

in B-Ruhesystem. Die angegebene Fehler sind statistisch und systematisch. Das CKM-Matrixelement $|V_{ub}|$ wird aus der Messung des partiellen Verzweigungsverhältnis, $\Delta\tilde{\mathcal{B}}$, und einer Berechnung im Rahmen der Theorie der “Heavy Quark Expansion” bestimmt. Das Ergebnis ist

$$|V_{ub}| = (4.19 \pm 0.18^{+0.26+0.26}_{-0.20-0.25}) \times 10^{-3},$$

wobei die angegebenen Fehler experimentelle Unsicherheiten, Unsicherheiten aus HQE-Parametern und theoretische Unsicherheiten darstellen.

Contents

List of Figures

List of Tables

1 Introduction

1.1 Overview

This thesis describes the measurement of the partial branching fraction, $\Delta\mathcal{B}(B \to X_u e\overline{\nu}_e)$, and the CKM matrix element $|V_{ub}|$ with semileptonic inclusive B meson decays using the BABAR data sample, corresponding to approximately 454 million $B\overline{B}$ meson pair decays. This analysis is a follow-up of previous studies [1], however it includes five times more statistics and new ideas for background suppression. In addition, compared to the previous analysis, more detailed systematics studies are performed as will be described in the next sections.

The extraction of $|V_{ub}|$ is complicated by the large background from $B \to X_c l\nu$ decays, which have a rate about 50 times higher than that of $B \to X_u l\nu$ decays. Therefore, kinematical cuts are applied in order to suppress $B \to X_c l\nu$ decays. This introduces a theoretical factor ζ, which describes the extrapolation from the partial to the full kinematic phase space: $\Delta\mathcal{B}(B \to X_u l\nu) = \tau_B |V_{ub}|^2 \zeta$. This factor ζ has to be provided by a theoretical calculation and depends on the selected phase space.

The applied kinematic cuts also introduce a sensitivity to the effects of b quark motion inside the B meson, which are described by Shape Functions and are the dominant sources of the theoretical errors. The experimental challenge is to select a kinematic phase space, where the dominant $B \to X_c l\nu$ background is suppressed while the theoretical uncertainties are still on an acceptable level.

In this analysis, the semileptonic decays are identified using the $q^2 - E_e$ technique by reconstructing the electron energy, E_e, and the invariant mass squared of the electron-neutrino pair, q^2. The neutrino kinematics is deduced from the decay products of both B mesons. The dominant $b \to c$ background was suppressed by selecting a $q^2 - E_e$ phase space region where the production of $B \to X_c l\nu$ events is kinematically suppressed. In addition, a special technique is developed to identify and to reject $B \to D^* \ell\nu$ decays which represent the main part of the $B \to X_c l\nu$ background. The selection criteria are optimized to reduce the amount of background and to improve the quality of the neutrino momentum measurement. The partial branching fraction $\Delta\mathcal{B}(B \to X_u e\overline{\nu}_e)$ is measured using the observed yield in data after subtraction of the background and correction for the signal efficiency both estimated from a Monte Carlo simulation. The CKM matrix element $|V_{ub}|$ is then determined from the measured $\Delta\mathcal{B}$ value using a theoretical calculation based on Heavy Quark Expansion.

1.2 Outline

The outline of this thesis is as follows: Chapter 2 gives a brief overview of the Standard Model with emphasis on theoretical aspects associated to the measurement of inclusive $B \to X_u e\overline{\nu}_e$ decays and the determination of the CKM matrix element $|V_{ub}|$. In chapter 3, the setup and the performance of the BABAR experiment are presented. Chapter 4 explains the analysis strategy, the datasets used, and the Monte Carlo simulation used to model the data. The chapters 5 to 7 describe the analysis steps leading to the extraction of the unfolded $B \to X_u e \overline{\nu}_e$ partial branching fractions and the evaluation of the dominant systematic uncertainties. The results and a comparison to results from other experiments are presented in chapter 8. The last chapter closes with a summary and conclusion on the future determination of $|V_{ub}|$.

2 Theory and Motivation

2.1 The Standard Model

The Standard Model (SM) is a gauge field theory with gauge group $SU(3)_C \times SU(2)_L \times U(1)_Y$. It represents today's knowledge about fundamental particles and their interactions. All baryonic matter in the universe is made up of fermions with spin $1/2$ and interactions are mediated by gauge bosons with an integer spin. There are six kinds of quarks and leptons arranged in three generations: the up-type quarks, u, c, t and the down-type quarks, d, s, b, the charged leptons e, μ, τ and corresponding neutral neutrinos ν_e, ν_μ, ν_τ. The strong interaction ($SU(3)_C$ group) is mediated by Color-charged particles, gluons. The $SU(2)_L \times U(1)_Y$ group describes the electroweak interaction as formulated in the Glashow-Weinberg-Salam (GWS) model [2–6]. The $SU(2)_L$ part leads to the coupling between left-handed fermions and $U(1)_Y$ is related to the weak hypercharge $Y = 2(Q - I_3)$, a combination of the third component of the weak isospin I_3 and the electric charge Q. The electroweak interaction is mediated by $W^\pm$, Z^0 bosons, and the photon, γ. The gravitational interaction which is not contained in the SM lacks so far a consistent quantum field theory description and can be neglected in the description of fundamental particle interaction for most purposes due to its weakness.

2.1.1 Symmetry Breaking and Mass Generation

In the GWS theory, the Higgs mechanism [7–9] is used to generate the masses of $W^\pm$, Z^0 bosons, and fermions by spontaneously breaking of $SU(2)_L \times U(1)_Y$ group. It requires the introduction of the Higgs field, represented by a single scalar Higgs doublet $\Phi = (\Phi_1, \Phi_2)$ leading to the terms in the Lagrangian

$$\mathcal{L}_{\text{Higgs}} = (\partial^\alpha \Phi)^\dagger (\partial_\alpha \Phi) - V(\Phi) \quad \text{with} \quad V(\Phi) = -\mu^2 \Phi^\dagger \Phi + \lambda^2 (\Phi^\dagger \Phi)^2. \tag{2.1}$$

The masses of fermions are then generated by Yukawa couplings to the Higgs field

$$\mathcal{L}_{Yuk} = \frac{\eta}{\sqrt{2}} (f^e_{ij} \overline{e}'_{iL} e'_{jR} + f^u_{ij} \overline{u}'_{iL} u'_{jR} + f^d_{ij} \overline{d}'_{iL} d'_{jR}) + h.c, \tag{2.2}$$

where the Higgs doublet is replaced by

$$\Phi \to \Phi(x) = \frac{1}{\sqrt{2}} \begin{pmatrix} 0 \\ \eta + h(x) \end{pmatrix} \tag{2.3}$$

after spontaneous symmetry breaking. The Yukawa coupling (2.2) describes the interaction of eigenstates of left-handed charged leptons, e, and up-type, u, and down-type, d, quarks with their right-handed counter-parts. The right-handed (R) fermions e'_{jR}, u'_{jR}, and d'_{jR} form singlets and the left-handed (L) fermions, $\overline{e}'_{iL}$, $\overline{u}'_{iL}$ and $\overline{d}'_{iL}$ form doublets with respect to the $SU(2)_L$ gauge group. η is the vacuum expectation value ($\langle\Phi\rangle = \eta/\sqrt{2}$) and $f_{ij}^{e,u,d}$ are the Yukawa coupling constants of the $i, j = 1,2,3$ generations. Thus, the mass matrices are given as

$$\mathbf{M}_{i,j}^{k} = -\frac{\eta}{\sqrt{2}} f_{i,j}^{k} \qquad k = e,\ u,\ d, \tag{2.4}$$

which are in general non-diagonal. One can diagonalize the mass matrices $\mathbf{M}^u$ and $\mathbf{M}^d$ using a global unitary transformation:

$$(V_{uL})^\dagger \mathbf{M}^u V_{uR} = \begin{pmatrix} m_u & 0 & 0 \\ 0 & m_c & 0 \\ 0 & 0 & m_t \end{pmatrix}, \qquad (V_{dL})^\dagger \mathbf{M}^d V_{dR} = \begin{pmatrix} m_d & 0 & 0 \\ 0 & m_s & 0 \\ 0 & 0 & m_b \end{pmatrix}. \tag{2.5}$$

There are no restrictions to the choice of the mass matrices $\mathbf{M}^u$ and $\mathbf{M}^d$. In general, the diagonalizing matrices for up-type and down-type quarks are different:

$$V_{uL} \neq V_{dL}, \qquad V_{uR} \neq V_{dR}. \tag{2.6}$$

The electroweak interaction eigenstates $u'_i(d'_i)$ and the mass eigenstates $u_i(d_i)$ are related by

$$\begin{aligned} u'_{iL} &= (V_{uL})_{ij} u_{jL} \qquad & d'_{iL} &= (V_{dL})_{ij} d_{jL} \\ u'_{iR} &= (V_{uR})_{ij} u_{jR} \qquad & d'_{iR} &= (V_{dR})_{ij} d_{jR}. \end{aligned} \tag{2.7}$$

The matrix $V = (V_{ij})$ defined as $V = (V_{uL})^\dagger V_{dL}$ is called the “Cabibbo-Kobayashi-Maskawa” matrix (CKM matrix), V_{CKM}:

$$V_{CKM} = \begin{pmatrix} V_{ud} & V_{us} & V_{ub} \\ V_{cd} & V_{cs} & V_{cb} \\ V_{td} & V_{ts} & V_{tb} \end{pmatrix}. \tag{2.8}$$

2.1.2 Weak Interactions and the CKM Matrix

The CKM matrix relates the weak interaction eigenstates to their mass eigenstates:

$$\begin{pmatrix} d' \\ s' \\ b' \end{pmatrix} = \begin{pmatrix} V_{ud} & V_{us} & V_{ub} \\ V_{cd} & V_{cs} & V_{cb} \\ V_{td} & V_{ts} & V_{tb} \end{pmatrix} \cdot \begin{pmatrix} d \\ s \\ b \end{pmatrix}. \tag{2.9}$$

The square of the CKM matrix element represents the transition probability between different quark flavours (e. g. $P_{b\to u} \propto |V_{ub}|^2$).
V_{CKM} is a product of unitary matrices and therefore has to be unitary itself:

$$V_{CKM} V_{CKM}^\dagger = V_{CKM}^\dagger V_{CKM} = 1. \tag{2.10}$$

The above relation can be expressed in a compact form:

$$\sum_j V_{ji} V_{jk}^* = \delta_{ik}. \tag{2.11}$$

Due to equation (2.10) and the unobservable phases of the quark fields, the number of independent parameters of V_{CKM} is reduced to four parameters. They can be interpreted as three mixing angles and one phase, which is responsible for CP violation in the Standard Model. The representation of the CKM matrix which makes use of experimentally observed hierarchy in the size of matrix elements is the Wolfenstein approximation [10] with the four reel parameters λ, A, ρ and η:

$$V_{\text{CKM}} = \begin{pmatrix} 1-\frac{\lambda^2}{2} & \lambda & A\lambda^3(\rho - i\eta) \\ -\lambda & 1-\frac{\lambda^2}{2} & A\lambda^2 \\ A\lambda^3(1-\rho-i\eta) & -A\lambda^2 & 1 \end{pmatrix} + \mathcal{O}(\lambda^4). \tag{2.12}$$

It is found that $\lambda \approx 0.22$ and $A = 0.82$. The unitarity relation (2.10) requires that $V_{ud}V_{ub}^* + V_{cd}V_{cb}^* + V_{td}V_{tb}^* = 0$. Using this equation combined with Wolfenstein approximation $V_{cd}V_{cb}^* \approx -A\lambda^3$, $V_{ud} \approx 1$, leads to the following expression:

$$(\rho + i\eta) - 1 + (1 - \rho - i\eta) = 0\,. \tag{2.13}$$

The former equation can be represented as a triangle in the complex plane, which is usually referred to as the unitarity triangle, as shown in Figure 2.1. The vectors are given by

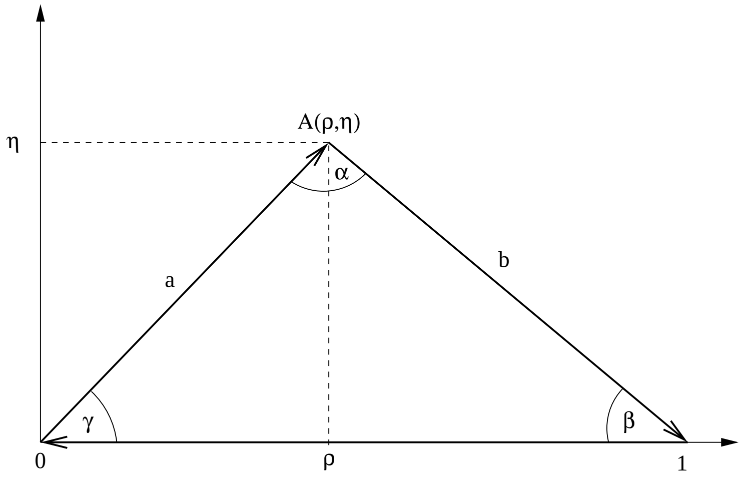

Figure 2.1: The unitarity triangle after division by $|V_{cb}V_{cd}^*|$.

$$\mathbf{a} \equiv \frac{V_{ud}V_{ub}^*}{|V_{cd}V_{cb}^*|} \qquad \text{and} \qquad \mathbf{b} \equiv \frac{V_{td}V_{tb}^*}{|V_{cd}V_{cb}^*|},$$

and three angles by

$$\alpha = \arg\left(-\frac{V_{td}V_{tb}^*}{V_{ud}V_{ub}^*}\right),\ \beta = \arg\left(-\frac{V_{cd}V_{cb}^*}{V_{td}V_{tb}^*}\right),\ \gamma = \arg\left(-\frac{V_{ud}V_{ub}^*}{V_{cd}V_{cb}^*}\right) = \pi - \alpha - \beta\,.$$

A crucial role plays the parameter $sin(2\beta)$, which indicates CP violation in the B meson system. The current world average [11] is $sin(2\beta) = 0.671 \pm 0.023$, which establishes *CP* violation in the B meson system.

The length of the triangle's left side, a, is proportional to the CKM matrix element $|V_{ub}|$. Hence, the measurement of $|V_{ub}|$ in processes that do not violate *CP* symmetry can be compared to measurements of $sin(2\beta)$. The consistency of the Standard Model can be tested, if both independent measurements ($|V_{ub}|$ and $sin(2\beta)$) give a consistent result, meaning that triangle closes at its apex.

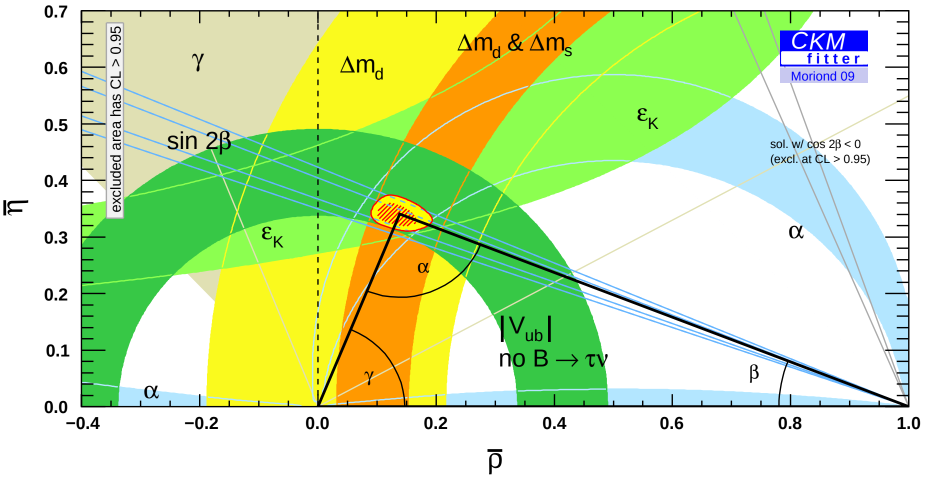

Figure 2.2: The global CKM fit results in the $\overline{\rho}-\overline{\eta}$ plane [12]. The apex is giveb by $\overline{\rho}+i\overline{\eta} = -\frac{V_{ud}V_{ub}^*}{V_{cd}V_{cb}^*}$. The branching ratio $B^+ \to \tau^+\nu_\tau$ is not included.

Figure 2.2 shows the current agreement between measurements and the CKM formalism. Shown are the constraints from semileptonic B decays ($|V_{ub}|$ and $|V_{cb}|$), $B^0\overline{B}^0$ mixing (Δm_d), $B_s^0\overline{B}_s^0$ mixing (Δm_s), *CP* violation in the neutral K system (ε_K), $B \to J/\psi K^{(*)0}$ decays ($sin(2\beta)$ and $cos(2\beta)$), $B \to \pi\pi, \rho\rho, \rho\pi$ decays (α), and $B \to D^{(*)}K^{(*)}$ decays (γ). The location and constraints on the apex of the triangle are also depending on our knowledge of $|V_{ub}|$. As can be seen, the more precise measurement of the CKM matrix element $|V_{ub}|$ can improve the constraint on the apex and also provides a consistency check between $sin(2\beta)$ measurement and constraints obtained from the fit to $|V_{ub}|$ and $|V_{cb}|$.

2.2 Semileptonic *B* Meson Decays

Measurements of semileptonic B meson decays are the most accessible and cleanest way to determine the CKM matrix elements $|V_{cb}|$ and $|V_{ub}|$. These decays also provide experimental access to study the QCD form-factors, heavy quark masses, and HQE parameters. The theoretical description of semileptonic B meson decays at the parton level is very simple, because there is no interaction between leptonic and hadronic currents. At the hadron level one needs to introduce corrections due to the strong interaction between quarks. Especially in the description of the inclusive B meson decays the motion of the b quark inside the B meson plays a crucial role. All these effects are described in the frameworks of Heavy Quark Effective Theory (HQET) and Lattice QCD (LQCD).

To extract precise values of the CKM matrix element $|V_{ub}|$ from measurements of the semileptonic B meson decays, $B \to X_u l \overline{\nu}_\ell$, requires a very good understanding of the decay dynamics. Furthermore, the extraction of $|V_{ub}|$ is complicated by the large background from $B \to X_c l \nu$ decays, which have a rate about 50 times higher than that of $B \to X_u l \nu$ decays. In the following sections, the corresponding physics are described in detail and a method used in this analysis for the determination of $|V_{ub}|$ is presented.

2.2.1 Exclusive Semileptonic Decays

In exclusive $B_{b\overline{q}} \to X_{q'\overline{q}} \ell^- \overline{\nu}$ decays the hadronic $X_{q'\overline{q}}$ system is explicitely reconstructed. The amplitude can be written as a product of a leptonic and a hadronic current

$$\mathcal{M}(B_{b\overline{q}} \to X_{q'\overline{q}} \ell^- \overline{\nu}) = -i \frac{G_F}{\sqrt{2}} V_{q'b} L^\mu H_\mu, \tag{2.14}$$

where G_F is the Fermi constant, $L^\mu = \bar{u}_l \gamma^\mu (1-\gamma_5) \upsilon_\nu$ is the leptonic current written interms of Dirac spinors u_l and υ_ν. The more complicated hadronic current, $H_\mu = \langle X | \overline{q}' \gamma^\mu (1-\gamma_5) b | B \rangle$, can be written in terms of form factors. Hence, the strong interaction effects are isolated inside H_μ. The hadronic current must be constructed from the available four-vectors (momentum and spin-polarization vectors). The so formed Lorentz-invariant quantities have coefficients (form factors) that are functions of q^2:

$$q^2 = (p_l + p_{\overline{\nu}})^2 = (p_B - p_X)^2 = m_B^2 + m_X^2 - 2 m_B E_X, \tag{2.15}$$

where p_B is the four-vector of the B meson, m_B its mass, m_X the mass and E_X the energy of the final state meson X in the rest frame of B. The calculation of H_μ depends on the chosen theoretical model and on the final state meson X (X is a pseudoscalar (P) or vector (V) meson).

The channel $B_{b\overline{q}} \to P_{q'\overline{q}} l \nu$ (for example $B \to \pi \ell \nu$ or $B \to D \ell \nu$)

For this decay channel the hadronic current has no axial vector contribution and can be written as

$$\begin{aligned} \langle P(p) | V^\mu | B(p_B) \rangle &= f_+(q^2) \left[(p_B + p)^\mu - \frac{m_B^2 - m_P^2}{q^2} q^\mu \right] \\ &+ f_0(q^2) \frac{m_B^2 - m_P^2}{q^2} q^\mu, \end{aligned} \tag{2.16}$$

where $f_+(q^2)$ and $f_0(q^2)$ are two form factors, p is the four-momentum of the P meson, and $V^\mu = q' \gamma^\mu b$. In the limit $m_l \to 0$ one has $q^\mu L_\mu = 0$ and hence $B \to P l \nu$ is described by only one form factor $f_+(q^2)$:

$$\langle P(p) | V^\mu | B(p_B) \rangle = f_+(q^2) (p_B + p)^\mu. \tag{2.17}$$

Using this equation one can calculate the differential decay rate:

$$\frac{d\Gamma}{dq^2} = \frac{G_F^2 |V_{q'b}|^2 |\vec{P}_P|^3}{24\pi^3} |f_+(q^2)|^2, \tag{2.18}$$

where $|\vec{P}_P|$ is magnitude of the three-momentum of the final-state meson P in the rest frame of B.

There are various form factor models which are used to predict the differential decay rate. The most relevant models for this analysis are ISGW2 [13], a constituent quark model (e. g. used to model $B \to D\ell\nu$ decays in simulation), and HQET [14, 15] model based on Heavy Quark Symmetry (HQS) (e. g. used for reweighting of simulated $B \to D\ell\nu$ Monte Carlo, as described in section 7.3).

In the HQET model the form factors are $h_+(w)$ and $h_-(w)$, where w is related to q^2 by

$$w = \frac{m_B^2 + m_P^2 - q^2}{2m_B m_P}. \tag{2.19}$$

The differential decay rate for HQET model is given as

$$\frac{d\Gamma^{HQET}}{dw} = \frac{G_F^2 |V_{q'b}|^2 m_B^5}{48\pi^3} r^3 (w^2-1)^{3/2} \left[(1+r)h_+(w)\right]^2, \tag{2.20}$$

where $r = m_P/m_B$. Using the CLN [16] parameterization h_+ can be written as

$$h_+(w) = h_+(1)[1 - 8\rho_D^2 z + (51\rho_D^2 - 10)z^2 - (252\rho_D^2 - 84)z^3] \tag{2.21}$$

with $z = (\sqrt{w+1} - \sqrt{2})/(\sqrt{w+1} + \sqrt{2})$. The slope ρ_D can be measured by experiments and $h_+(1)$ can be given by a Lattice QCD calculation [17].

The differential decay rate for ISGW2 model can be also given as function of w:

$$\frac{d\Gamma^{ISGW2}}{dw} = \frac{G_F^2 |V_{q'b}|^2 m_B^5}{48\pi^3} r^3 (w^2-1)^{3/2} \left[(1+r)Rf_+\right]^2, \tag{2.22}$$

where $R = \frac{2\sqrt{m_B m_P}}{m_B m_P}$.

Hence, in the case of reweighting of simulated events from ISGW2 to HQET model corresponding weights are calculated as:

$$F(w) = \frac{d\Gamma^{HQET}}{dw} \Big/ \frac{d\Gamma^{ISGW2}}{dw}. \tag{2.23}$$

The channel $B_{b\overline{q}} \to V_{q'\overline{q}} l\nu$ (for example $B \to \rho\ell\nu$ or $B \to D^*\ell\nu$)

The expression for the hadronic current in case of small lepton masses can be written in terms of three independent form factors $A_1(q^2)$, $A_2(q^2)$, and $V(q^2)$

$$\begin{aligned} \langle V(p,\varepsilon)|V^\mu - A^\mu|B(p_B)\rangle = {} & \frac{2iV(q^2)}{m_B+m_V} \varepsilon^{\mu\nu\alpha\beta} \varepsilon_\nu^* p_\alpha p_{B,\beta} \\ & - (m_B+m_V)A_1(q^2)\varepsilon^{*\mu} + \frac{A_2(q^2)}{m_B+m_V}(\varepsilon^* \cdot q)(p_B+p)^\mu, \end{aligned} \tag{2.24}$$

where ε is the vector-meson polarization vector, m_V is the vector-meson mass, and p_V its four-momenta. The full differential decay rate is usually expressed in terms of the vector-meson helicity amplitudes $H_+(q^2)$, $H_-(q^2)$, and $H_0(q^2)$

$$\begin{aligned} H_\pm(q^2) &= (m_B+m_V)A_1(q^2) \mp \frac{2m_B|\vec{p}_V|}{m_B+m_V}V(q^2), \\ H_0(q^2) &= \frac{1}{2m_V\sqrt{q^2}}[(m_B^2-m_V^2-q^2)(m_B+m_V)A_1(q^2) \\ &- 4\frac{m_B^2|\vec{p}_V|^2}{m_B+m_V}A_2(q^2)]. \end{aligned} \tag{2.25}$$

The full differential decay rate is then

$$\begin{aligned} \frac{d\Gamma(B\to Vl\nu, V\to P_1P_2)}{dq^2dc_Vdc_Ld\chi} &= \frac{3}{32\pi^4}G_F^3|V_{q'b}|^2\frac{|\vec{p}_V|q^2}{m_B^2}\mathcal{B}(V\to P_1P_2) \\ &\times \{(1-\eta c_L)^2(1-c_V^2)|H_+(q^2)|^2 \\ &+ (1+\eta c_L)^2(1-c_V^2)|H_-(q^2)|^2 \\ &+ 4(1-c_L^2)c_V^2|H_0(q^2)|^2 \\ &- 4\eta\sqrt{1-c_L^2}(1-\eta c_L)\sqrt{1-c_V^2}c_V cos\chi H_+(q^2)H_0(q^2) \\ &- 4\eta\sqrt{1-c_L^2}(1+\eta c_L)\sqrt{1-c_V^2}c_V cos\chi H_-(q^2)H_0(q^2) \\ &- 2(1-c_L^2)(1-c_V^2)cos2\chi H_+(q^2)H_-(q^2)\}. \end{aligned} \tag{2.26}$$

The following notation is used in equation (2.26):

- $c_L \equiv cos\theta_l$: the cosine of the angle of the lepton in the W rest frame with respect to the W flight direction in the B meson rest frame;
- $c_V \equiv cos\theta_V$: the cosine of the angle of one of the pseudoscalar daughters in the rest frame of the vector-meson with respect to the V flight direction in the B meson rest frame;
- χ: the angle between the decay planes of the W and the vector meson;
- η: a factor related to the charge of the b quark ($\eta = +1$ for b charge of $-1/3$).

An example for the decay channel $B \to Vl\nu$ ($V \equiv D^*$) is shown in picture 2.3.
Using the HQET [14, 15] model, after the integration of equation (2.26) over the angular variables and replacing q^2 by w one obtains the differential decay rate $d\Gamma/dw$ depending on a form factor $F(w)$:

$$\frac{d\Gamma}{dw} = \frac{G_F^2}{48\pi^3m_V^3}[m_B-m_V]^2G(w)F^2(w)|V_{q'b}|^2, \tag{2.27}$$

where $G(w)$ is the known phase space factor:

$$G(w) = \sqrt{w^2-1}(w+1)^2\left[1+\frac{4w}{w+1}\frac{m_B^2-2wm_Bm_V+m_V^2}{(m_B-m_V)^2}\right]. \tag{2.28}$$

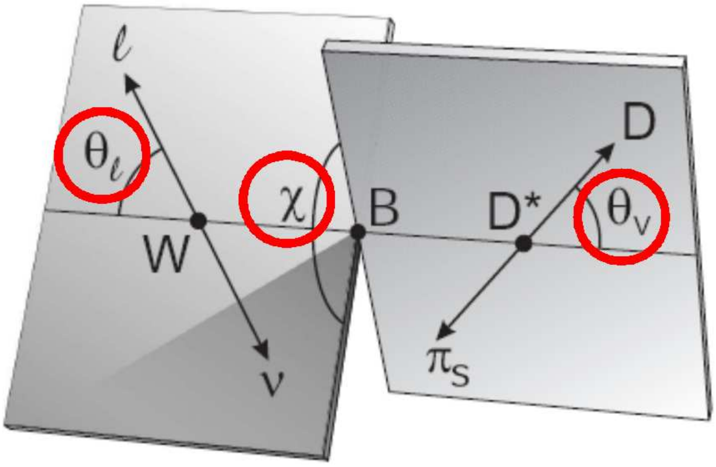

Figure 2.3: θ_l is the polar angle of the lepton in the W rest frame with respect to the W flight direction in the B meson rest frame, and θ_V is the polar angle of the D or the π meson in the rest frame of the D^* with respect to the D^* flight direction in the B meson rest frame. χ is the angle between the decay planes of the W and the D^* meson.

The form factor $F(w)$ can be written in terms of parameters $R_1(w)$, $R_2(w)$, and $h_{A_1}(w)$ using the CLN [16] parameterization

$$\begin{aligned} R_1(w) &= R_1 - 0.12(w-1) + 0.05(w-1)^2 \\ R_2(w) &= R_2 + 0.11(w-1) - 0.06(w-1)^2 \\ h_{A_1}(w) &= h_{A_1}(1)[1 - 8\rho^2 z + (53\rho^2 - 15)z^2 - (231\rho^2 - 91)z^3], \end{aligned} \tag{2.29}$$

where the parameters R_1, R_2 and ρ are measured by experiments.

2.2.2 Inclusive Semileptonic Decays

In the case of inclusive semileptonic decays, $B \longrightarrow X_q l \overline{\nu}$, one considers the sum over all possible final state hadrons, ignoring the detailed breakdown among the individual decay modes that contribute to the semileptonic rate. The inclusive decays of hadrons containing a heavy quark such as a b quark offer two advantages over the exclusive approach. The final hadronic state, X_q, consists of a sum of many hadronic channels, which eliminates bound-state effects related to the properties of individual hadrons. In addition, the bound-state effects related to the initial state, B, can be accounted for in a systematic way using the Heavy Quark Expansion [18, 19] (e. g. Fermi Motion of the b quark inside the B meson).

Figure 2.4 shows the decay topology of $b \longrightarrow q l \overline{\nu}$ transition at the parton level (left diagram), where the dependency of the decay amplitudes on V_{qb} is introduced. The calculated rate at the parton level is proportional to V_{qb}^2 and m_b^5, where m_b refers to the b quark mass. The right diagram in Figure 2.4 provides a more realistic view of $B \longrightarrow X_q l \overline{\nu}$ decays. Due to the presence of the second valence quark ($q \equiv u, d$), the description of the decay dynamics has to be modified such that the perturbative and non-perturbative QCD effects are taken into account. Nevertheless, inclusive semileptonic B meson decays provide a

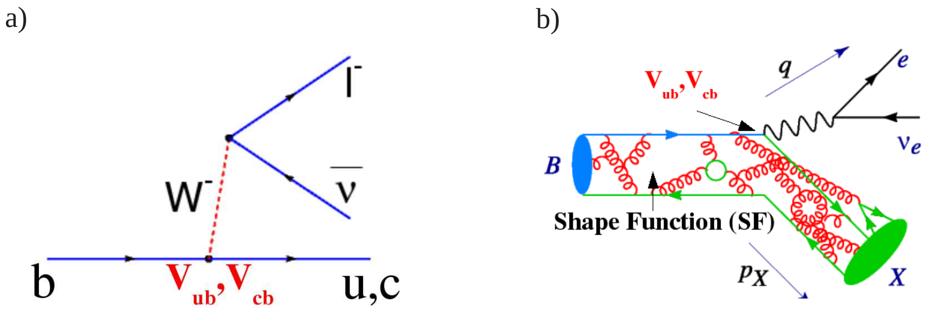

Figure 2.4: Semileptonic B meson decays (a) at the parton level and (b) at the hadron level. The kinematic variables used to describe $B \longrightarrow X_q l \overline{\nu}$ decays are also presented on the right diagram.

very clean environment to measure the CKM matrix elements $|V_{qb}|$ and the study of non-perturbative effects, because there is no strong interaction between the X_q system and the electron-neutrino pair.

The perturbative and non-perturbative corrections can be calculated using various theoretical tools: Heavy Quark Expansion [18,19] (HQE) and QCD [20,21] factorization. Both approaches perform a systematic separation of the perturbative from the non-perturbative quantities and sort terms in powers of $1/m_b$. The HQE is an appropriate approach for the calculation of total inclusive B decay rates and for partial decay rates integrated over sufficiently large regions of phase space where the mass and momentum of the final state hadron are large compared to Λ_{QCD}. QCD factorization is better suited for the calculation of partial rates and spectra near kinematical boundaries where the hadronic mass is small.

The HQE is an effective field theory for the limit $\Lambda_{QCD}/m_b \longrightarrow 0$. Its physics content is characterized by gluon virtualities at energy scales $\Lambda_{QCD} < \mu < m_b$, with the typical scale μ, satisfying $\alpha_s(m_b)/\pi \approx 0.1 \ll 1$ and $\Lambda_{QCD}/m_b < \mu/m_b \sim 0.1 \ll 1$. In HQE, the Lagrangian is written in terms of local operators, the expectation value of which are properties of the b quark inside the B meson. Processes with virtual hard gluons which drive the heavy quark far off shell lead to calculable perturbative corrections in the effective theory to order $\alpha_s(m_b)$. The power corrections lead to terms of order $\Lambda^n = (\Lambda_{QCD}/m_b)^n$. These non-perturbative corrections are difficult to calculate and require the introduction of new phenomenological parameters (e. g. μ_π^2 and μ_G^2 at order Λ^2) whose values must be determined from experiments, e. g. from the global HQE fit to moments of inclusive $B \longrightarrow X_c l \nu$ and $B \longrightarrow X_s \gamma$ events [22].

2.2.2.1 Differential Decay Rates

The hadronic physics in $B \longrightarrow X_u l \nu$ decays is encoded in the hadronic tensor

$$W_{\mu\nu}(p,v) = \frac{1}{\pi}\mathrm{Im}\, T_{\mu\nu}(p,v), \tag{2.30}$$

where

$$T_{\mu\nu}(p,v) = -i\int d^4x e^{i(p-m_b v)\cdot x}\frac{\langle B(v)|T\{J^{\dagger}_{\mu}(x),J_{\nu}(0)\}|B(v)\rangle}{2M_B} \tag{2.31}$$

is the forward scattering amplitude given by the B matrix element of two flavour-changing weak currents $J_\mu = \bar{u}\gamma_\mu(1-\gamma_5)b$. The hadronic tensor, $W_{\mu\nu}$, is characterized by two independent variables: v is the b quark velocity, which can be taken to coincide with the velocity of the B meson, and p is the momentum of the jet of light particles into which the b quark decays. The momentum carried by the leptons is $q = m_b v - p$. The most general Lorentz-invariant decomposition of $W_{\mu\nu}$ contains five invariant structure functions $\tilde{W}_i$

$$\begin{aligned} W_{\mu\nu} &= (p_\mu v_\nu + p_\nu v_\mu - g_{\mu\nu} v\cdot p - i\varepsilon_{\mu\nu\alpha\beta}p^\alpha v^\beta)\tilde{W}_1 \\ &- g_{\mu\nu}\tilde{W}_2 + v_\mu v_\nu \tilde{W}_3 + (p_\mu v_\nu + p_\nu v_\mu)\tilde{W}_4 + p_\mu p_\nu \tilde{W}_5. \end{aligned} \tag{2.32}$$

The triple differential $B \to X_u l\nu$ decay rate can then be written in terms of the $\tilde{W}_i$ functions. In this analysis the most relevant theoretical approaches are from De Fazio and Neubert (DFN) [23] and from Björn O. Lange, Mathias Neubert, and Gil Paz (BLNP) [24].

Triple differential decay rate in the DFN model

The simulation of $B \to X_u l\nu$ decays in this analysis is based on the DFN model. The corresponding triple differential decay rate is

$$\begin{aligned} \frac{d^3\Gamma}{dx\,dz\,d\tilde{p}^2} = 12\Gamma_0\{&(1+\bar{x}-z)(z-\bar{x}-\tilde{p}^2)\frac{m_b^2}{2}\tilde{W}_1 + (1-z+\tilde{p}^2)\frac{m_b}{2}\tilde{W}_2 + \\ &+ [\bar{x}(z-\bar{x})-\tilde{p}^2]\frac{m_b}{2}(\tilde{W}_3 + 2m_b\tilde{W}_4 + m_b^5\tilde{W}_5)\}, \end{aligned} \tag{2.33}$$

where $\bar{x} = 1-x$ and

$$\Gamma_0 = \frac{G_F^2|V_{ub}|^2 m_b^5}{192\pi^3}. \tag{2.34}$$

The three variables x, z, and $\tilde{p}$ have the following meaning at the parton level

$$x = \frac{2E_l}{m_b}, \qquad z = \frac{2(E_{X_u}-\bar{\Lambda}}{m_b}), \qquad \text{and} \qquad \tilde{p}^2 = \frac{m_{X_u}^2 - 2E_{X_u}\bar{\Lambda} - \bar{\Lambda}^2}{m_b^2}, \tag{2.35}$$

where E_{X_u} and m_{X_u} are the energy and mass of the hadronic state X_u, and $\bar{\Lambda} = M_B - m_b$ is the binding energy. The effects of the Fermi motion have to be taken into account, especially in the low mass region where $m_X = \mathcal{O}(\Lambda_{QCD})$. In the DFN model, these effects are parameterized through $\tilde{W}_i$ using a Shape Function (SF) which defines the momentum distribution of the b quark inside the B meson. The form of the SF can be described using one of the following ansätze: exponential, Gaussian and Roman. The exponential SF is parameterized as

$$F(k_+) = N(1-x)^a e^{(1+a)x} \qquad \text{with} \qquad x = \frac{k_+}{\Lambda} \leq 1, \tag{2.36}$$

where the b quark mass, m_b, and dimensionless parameter a are the two free parameters. The Gaussian SF form is given as

$$F(k_+) = N(1-x)^a e^{-b^2(1+x)^2} \qquad \text{with} \qquad b = \Gamma\left(\frac{a+2}{2}\right)(\Gamma\left(\frac{a+2}{2}\right), \tag{2.37}$$

and the Roman as

$$F(k_+) = N\frac{\kappa}{\pi} e^{-\frac{1}{4}(\frac{1}{\kappa}\frac{a}{1-x}-\kappa(1-x))^2} \qquad \text{with} \qquad \kappa = \frac{a}{\pi} e^{a/2} K_1(a/2), \tag{2.38}$$

where K_1 refers to the modified Bessel function of the first kind.
All three ansätze must satisfy conditions imposed on the three k_+ moments,

$$A_n = \int_{-\infty}^{\bar{\Lambda}} dk_+ k_+^n F(k_+), \tag{2.39}$$

where $A_0 = 1, A_1 = 0$, and $A_2 = -\lambda_1/3$. The choice of Shape Function parameter a and m_b depends on current measurement of the HQE parameters $\bar{\Lambda}$ and λ_1 and will discussed in section 4.3.2. The relation between the HQE parameters (defined in the Kagan-Neubert scheme [25]) and the SF parameters is given by

$$m_b = M_B - \bar{\Lambda} \qquad \text{and} \qquad a = \frac{3\bar{\Lambda}^2}{-\lambda_1} - 1. \tag{2.40}$$

Triple differential decay rate in the BLNP approach

The determination of the CKM matrix elements $|V_{ub}|$ from the measured partial branching fraction is performed in this analysis using the BLNP [24] approach. The BLNP model is the one of the theoretical approaches, which is used in the semileptonic comunity to extract $|V_{ub}|$. This model incorporates higher-order power corrections where the leading terms in the HQE are computed at next-to-leading order.
The differential decay rate is described by following three independent kinematic variables:

$$P_l = M_B - 2E_l, \qquad P_- = E_{X_u} + |\vec{P}_{X_u}|, \qquad P_+ = E_{X_u} - |\vec{P}_{X_u}|, \tag{2.41}$$

where E_{X_u} and $\vec{P}_{X_u}$ are the energy and three-momentum of the hadronic state X_u, and E_l is the energy of the charged lepton. In terms of the structure functions, $\tilde{W}_i$, the triple differential $B \rightarrow X_u l \nu$ decay rate reads

$$\begin{aligned}\frac{d^3\Gamma}{dP_+ dP_- dP_l} = \frac{G_F^2 |V_{ub}|^2}{16\pi^3} U_y(\mu_h, \mu_i)(M_B - P_+)\{&(P_- - P_l)(M_B - P_- + P_l - P_+)\mathcal{F}_1 + \\ &+ (M_B - P_-)(P_- - P_+)\mathcal{F}_2 + (P_- - P_l)(P_l - P_+)\mathcal{F}_3\},\end{aligned} \tag{2.42}$$

where relevant combinations of $\tilde{W}_i$ are collected into three functions at the matching scales $\mu_h \sim m_b$ and $\mu_i \sim \sqrt{m_b \Lambda_{QCD}}$

$$U_y(\mu_h, \mu_i)\mathcal{F}_1 = \tilde{W}_1, \qquad U_y(\mu_h, \mu_i)\mathcal{F}_2 = \frac{\tilde{W}_2}{2}, \qquad U_y(\mu_h, \mu_i)\mathcal{F}_3 = \left(\frac{y}{4}\tilde{W}_3 + \tilde{W}_4 + \frac{1}{y}\tilde{W}_5\right).$$

$$\tag{2.43}$$

The variable y is defined as

$$y = \frac{P_- - P_+}{M_B - P_+} \tag{2.44}$$

and is used to parameterize the leading Sudakov factor $U_y(\mu_h, \mu_i)$.
The leading-power expressions for $\tilde{W}_i$ can be calculated in [26] at one-loop order in renormalization group improved perturbation theory. At this level, $\mathcal{F}_2$ vanishes, whereas $\mathcal{F}_1$ and $\mathcal{F}_3$ are factorized as

$$\begin{aligned} \mathcal{F}_1(P_+, y) &= H_u(y, \mu_h) \int_0^{P_+} d\hat{w}\, y m_b\, J(y m_b (P_+ - \hat{w}), \mu_i)\, \hat{S}(\hat{w}, \mu_i), \\ \mathcal{F}_3(P_+, y) &= \frac{C_F \alpha_s(\mu_h)}{4\pi} \frac{2 \ln y}{1 - y} \hat{S}(P_+, \mu_i), \end{aligned} \tag{2.45}$$

where $\hat{S}$ is the leading Shape Function. The definition of hard function H_u and jet function J can be found in Ref. [24]. The HQE parameters $\overline{\Lambda}$ and μ_π^2 are defined in the Shape Function scheme [27] through the $\hat{S}(\hat{w}, \mu_i)$ moment relations as

$$\frac{M_1}{M_0} = \overline{\Lambda} \qquad \text{and} \qquad \frac{M_2}{M_0} = \frac{\mu_\pi^2}{3} \overline{\Lambda}^2, \tag{2.46}$$

where moments of $\hat{S}(\hat{w}, \mu_i)$ are defined as

$$M_N(\hat{w}_0, \mu_i) \equiv \int_0^{\hat{w}_0} d\hat{w}\, \hat{w}^N\, \hat{S}(\hat{w}, \mu_i). \tag{2.47}$$

$\hat{S}(\hat{w}, \mu_i)$ can be modeled from three two-parameter functional forms: an exponential-type function F^{exp}, a gaussian-type function F^{gauss}, and a hyperbolic-type function F^{hyp}. The two independent SF parameters are the dimensionful quantity Λ and a positive number b. The SF forms are defined as

$$\begin{aligned} F^{\text{exp}}(\hat{w}; \Lambda, b) &= \frac{N^{\text{exp}}}{\Lambda} \left(\frac{\hat{w}}{\Lambda} \right)^{b-1} e^{-d_{\text{exp}} \frac{\hat{w}}{\Lambda}}, \\ F^{\text{gauss}}(\hat{w}; \Lambda, b) &= \frac{N^{\text{gauss}}}{\Lambda} \left(\frac{\hat{w}}{\Lambda} \right)^{b-1} e^{-d_{\text{gauss}} \frac{\hat{w}^2}{\Lambda^2}}, \\ F^{\text{hyp}}(\hat{w}; \Lambda, b) &= \frac{N^{\text{hyp}}}{\Lambda} \left(\frac{\hat{w}}{\Lambda} \right)^{b-1} cosh^{-1} \left(d_{\text{hyp}} \frac{\hat{w}}{\Lambda} \right), \end{aligned} \tag{2.48}$$

where

$$\begin{aligned} N^{\text{exp}} &= \frac{d_{\text{exp}}^b}{\Gamma(b)}, \qquad d_{\text{exp}} = b, \\ N^{\text{gauss}} &= \frac{2 d_{\text{gauss}}^{b/2}}{\Gamma(b/2)}, \qquad d_{\text{gauss}} = \left(\frac{\Gamma\left(\frac{1+b}{2}\right)}{\Gamma\left(\frac{b}{2}\right)} \right)^2, \\ N^{\text{hyp}} &= \frac{[4 d_{\text{hyp}}]^b}{2\Gamma(b)[\zeta(b, 1/4) - \zeta(b, 3/4)]}, \qquad d_{\text{hyp}} = \frac{b}{4} \frac{\zeta(1+b, 1/4) - \zeta(1+b, 3/4)}{\zeta(b, 1/4) - \zeta(b, 3/4)}, \end{aligned} \tag{2.49}$$

and ζ is the generalized Riemann function. For the exponential ansatz, the Shape Function parameters Λ and b are related to the HQE parameters $\overline{\Lambda}$ and μ_π^2 (defined in the SF scheme [27] and measured by experiments) via

$$\begin{aligned}\overline{\Lambda} &= \frac{\Lambda}{b}\frac{\Gamma(1+b)-\Gamma(1+b,\frac{b\hat{w}_0}{\Lambda})}{\Gamma(b)-\Gamma(b,\frac{b\hat{w}_0}{\Lambda})},\\ \mu_\pi^2 &= 3\left[\frac{\Lambda^2}{b^2}\frac{\Gamma(2+b)-\Gamma(2+b,\frac{b\hat{w}_0}{\Lambda})}{\Gamma(b)-\Gamma(b,\frac{b\hat{w}_0}{\Lambda})}-\overline{\Lambda}^2\right],\end{aligned} \tag{2.50}$$

where $\hat{w}_0 = M_B - 2\cdot 1.8\,\mathrm{GeV}$.

2.3 The $q^2 - E_l$ Approach

The extraction of $|V_{ub}|$ is complicated by the large background from $B \to X_c l\nu$ decays, which have a rate about 50 times higher than that of $B \to X_u l\nu$ decays. Therefore, kinematical cuts are applied in order to suppress $B \to X_c l\nu$ decays. This introduces a theoretical factor ζ, which describes the extrapolation from the partial to the full kinematic phase space: $\Delta\mathcal{B}(B \to X_u l\nu) = \tau_B |V_{ub}|^2 \zeta$. This factor ζ has to be provided by a theoretical calculation and depends on the selected phase space.
The applied kinematic cuts also introduce sensitivity to the effects of b quark motion inside the B meson, which are described by Shape Functions and are the dominant sources of the theoretical errors. The experimental challenge is to select a kinematic phase space, where the dominant $B \to X_c l\nu$ background is suppressed while the theoretical uncertainties are still on an acceptable level.

One method to extract $|V_{ub}|$ is the selection of a phase space region beyond the lepton-momentum-spectrum endpoint for $B \to X_c l\nu$ processes. The translation of the measured rate in this region into a value of $|V_{ub}|$ leads to significant theoretical uncertainties due to the tiny portion of phase space. As an alternative, one can use hadronic variables such as the mass of the hadronic system, m_X. In this case, the second B must be fully reconstructed, to achieve a good m_X resolution. This requires large statistics, since the efficiency for a full reconstruction of the second B meson is only about half a percent.

The $q^2 - E_l$ approach used in this analysis, makes it possible to select a phase space, which is larger than that of endpoint analyses. The selection efficiency is higher than for m_X analyses, while the signal to background ratio is worse than studies based on m_X.
The semileptonic $B \to X_u l\nu$ decays are selected by reconstructing the lepton energy, E_l, and the invariant mass squared of the lepton-neutrino pair, q^2. The neutrino kinematics is deduced from the decay products of both B mesons. q^2 and E_l are then combined to compute the maximum kinematically allowed invariant mass squared of the hadronic system, $s_\mathrm{h}^\mathrm{max}$ [28]. The definition of $s_\mathrm{h}^\mathrm{max}$ in the B meson rest frame is very simple

$$s_\mathrm{h}^\mathrm{max} = (p_B - (p_\nu + p_l))^2 = (m_B - 2E_l)(m_B - \frac{q^2}{2E_l}), \tag{2.51}$$

where p_B, p_ν, p_l are the four-vectors of the B meson, the neutrino and the lepton. Since the B meson can not be fully reconstructed, the $s_\mathrm{h}^\mathrm{max}$ must be expressed in $\Upsilon(4S)$ rest frame. In the case $\mp E_l > \mp\frac{\sqrt{q^2}}{2\eta_\pm}$, the $s_{\mathrm{h}}^{\mathrm{max}}$ has the form

$$s_{\mathrm{h}}^{\mathrm{max}} = (m_B - 2\eta_\pm E_l)(m_B - \frac{q^2}{2\eta_\pm E_l}) \tag{2.52}$$

with

$$\eta_\pm = \sqrt{\frac{1\pm\beta}{1\mp\beta}} \qquad \text{and} \qquad \beta = \sqrt{1-\left(\frac{2m_B}{m_{\Upsilon(4S)}}\right)^2}, \tag{2.53}$$

otherwise,

$$s_{\mathrm{h}}^{\mathrm{max}} = m_B^2 + q^2 - 2m_B\sqrt{q^2}. \tag{2.54}$$

β represents the speed of the B meson in the $\Upsilon(4S)$ rest frame ($\beta \approx 0.06$).
Figure 2.5 illustrates the meaning of $s_{\mathrm{h}}^{\mathrm{max}}$. The contours in the $q^2 - E_l$ plane refer to constant values of $s_{\mathrm{h}}^{\mathrm{max}}$: the black diagonal contour defined by $s_{\mathrm{h}}^{\mathrm{max}} = 0$ represents the boarder the region containing $B \to X_u l\nu$ events, whereas the blue contour denotes the kinematical threshold ($s_{\mathrm{h}}^{\mathrm{max}} = m_D^2$) for the production of the D meson. Hence, restricting the analysis to the area between the two contours, no events with a true hadronic recoil mass above m_D can enter the $B \to X_u l\nu$ sample unless q^2 or E_l are not correctly reconstructed.

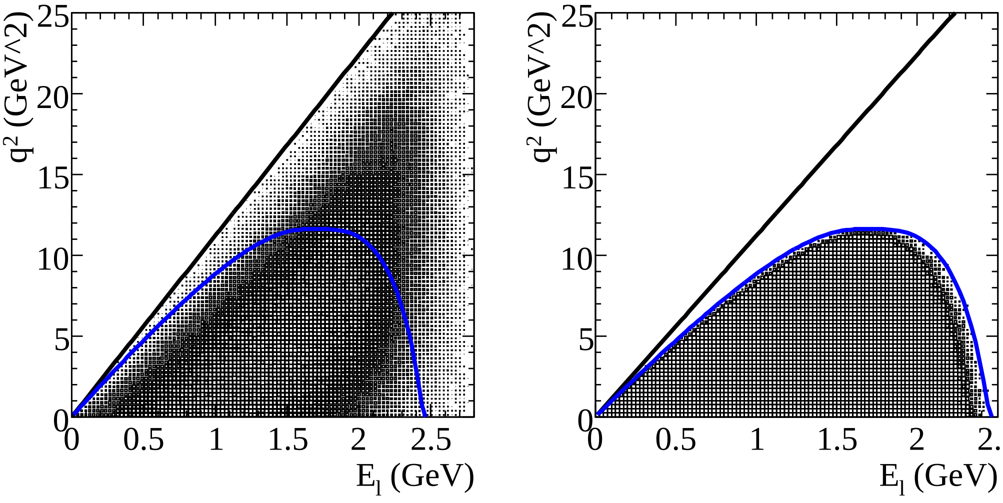

Figure 2.5: Distribution of $B \to X_u l\nu$ (left) and $B \to X_c l\nu$ (right) decays in the $q^2 - E_l$ plane. The distributions are obtained through generator-level Monte Carlo simulation. The solid lines represents constant values of $s_{\mathrm{h}}^{\mathrm{max}}$(see text).

3 The *BABAR* Experiment

3.1 Introduction

The primary goal of the *BABAR* experiment is to discover and precisely and systematically measure the violation of *CP* symmetry in the decays of the neutral B mesons. In addition, a wide range of other B physics studies such as the search for rare or semileptonic B meson decays can be used to overconstrain the unitarity triangle and either confirm a consistent picture within Standard Model or give hints to new physics. Several requirements must be fullfiled to achieve these goals, as described in the following.

At the storage ring PEP-II at the Stanford Linear Accelerator Center (SLAC) 9 GeV electrons are collided with 3.1 GeV positrons. The collision energy of $\sqrt{s} = 10.58\,\mathrm{GeV}$ in the center-of-mass (cms) frame excites the $\Upsilon(4S)$ resonance, which decays almost exclusively, $e^+e^- \rightarrow \Upsilon(4S) \rightarrow B\overline{B}$, to pairs of B mesons ($B^0\overline{B}^0$ or B^+B^-). Table 3.1 shows the various production cross-sections at the energy of the $\Upsilon(4S)$ resonance, $\sqrt{s} = 10.58\,\mathrm{GeV}$, expected within the *BABAR* detector acceptance.
In the $\Upsilon(4S)$ rest frame the B mesons are produced almost at rest ($\beta \approx 0.06$) and have a small life-time. Due to the boost $\beta\gamma = 0.55$ of the center-of-mass frame and an excellent vertex resolution, it is possible to study the $B^0\overline{B}^0$ oscillations and time dependent *CP* violation. Besides asymmetric beam-energies and an excellent vertex-detector, a good charged and neutral particle identification system and very high luminosities are needed to select the interesting decay channels.

During the years 1999 to 2008 an integrated luminosity of $531.43\,\mathrm{fb}^{-1}$ was recorded with the *BABAR* detector. About $433\,\mathrm{fb}^{-1}$ of data were taken at the $\Upsilon(4S)$ resonance (on-peak), $53.82\,\mathrm{fb}^{-1}$ of data were taken 40 MeV below $\Upsilon(4S)$ resonance (off-peak), $30.23\,\mathrm{fb}^{-1}$ at the $\Upsilon(3S)$ resonance, and $30.23\,\mathrm{fb}^{-1}$ at the $\Upsilon(2S)$ resonance. Figure 3.1 shows the integrated luminosities as a function of time.

3.2 The *BABAR* Detector

Figure 3.2 shows the acceleration and storage system at PEP-II. Particles collide in the interaction region, which is slightly shifted in the negative z direction with respect to the center of the *BABAR* detector to take into account of the asymmetric energy configuration of PEP-II. A schematic view of the *BABAR* detector with its sub-detectors is shown in Figure 3.3. The detector is composed of a silicon vertex tracker (SVT), a drift chamber (DCH), a Cherenkov detector (DIRC), an electromagnetic calorimeter (EMC), a magnetic superconducting coil providing a magnetic field of 1.5 T, and finally an instrumented flux return (IFR). These subsystems are described in the following. A detailed description of the *BABAR* detector can be found in [31].

$e^+e^- \longrightarrow$	Cross-section
$b\overline{b}$	1.10 nb
$c\overline{c}$	1.30 nb
$s\overline{s}$	0.35 nb
$u\overline{u}$	1.39 nb
$d\overline{d}$	0.35 nb
$\tau^+\tau^-$	0.94 nb
$\mu^+\mu^-$	1.16 nb
e^+e^-	$\approx$ 40 nb

Table 3.1: Effective cross-sections at the energy of the $\Upsilon(4S)$ resonance, $\sqrt{s} = 10.58\,\text{GeV}$, expected within the *BABAR* detector acceptance. All values are taken from [29] with exception of $b\overline{b}$ [30].

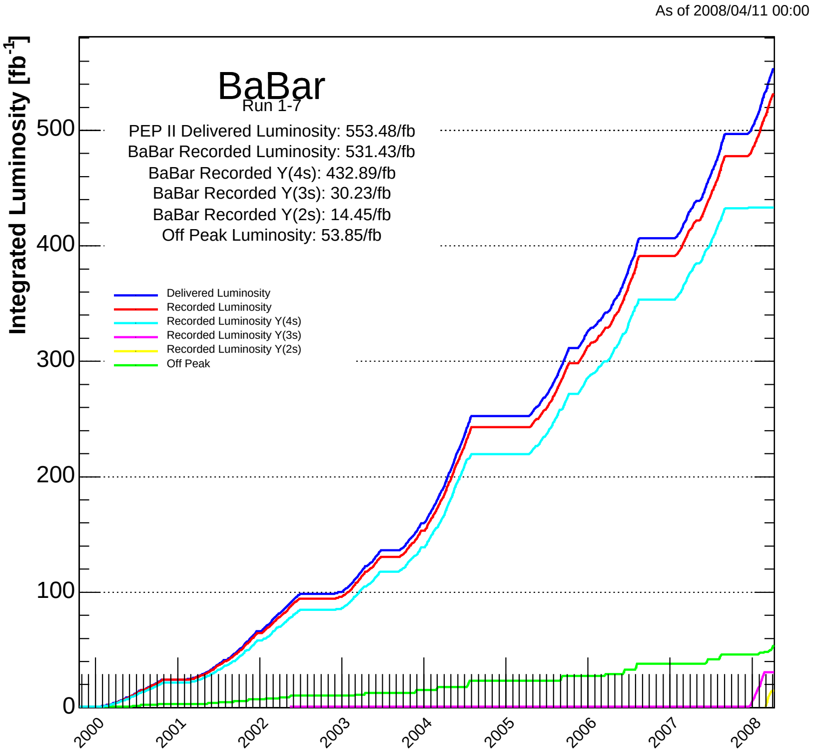

Figure 3.1: Integrated luminosity delivered by PEP-II and recorded by *BABAR* vs. time.

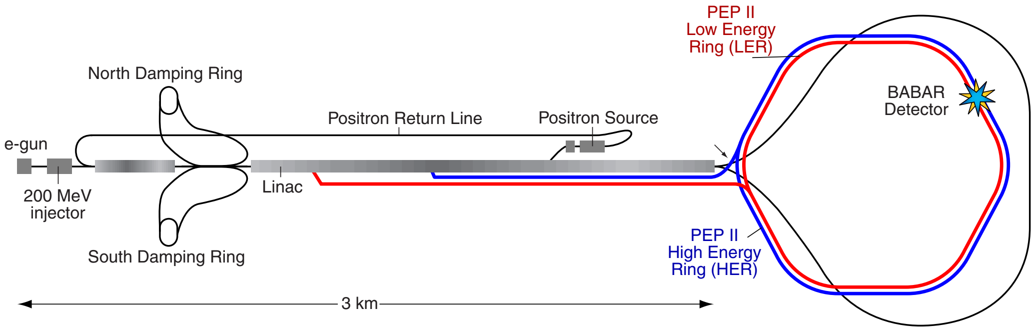

Figure 3.2: Schematic view of the acceleration and storage rings of PEP-II.

3.2.1 The Silicon Vertex Tracker (SVT)

The SVT has been designed to provide precise information of charged particle trajectories and decay vertices close to the interaction region. The vertex resolution must be better than $70\,\mu$m along the z-axis and $100\,\mu$m in the xy-plane to fully reconstruct B mesons. Moreover, the particles with transverse momenta $p_{\mathrm{t}} < 120\,\mathrm{MeV}/c$ can be only reconstructed in the SVT.

The SVT consists of 5 concentric cylindrical layers of silicon microstrip detectors with radii between 32 mm and 144 mm. The inner three layers have a spatial resolution of $15\,\mu$m for perpendicular tracks, while the resolution of the outer two layers is $40\,\mu$m. The SVT covers a polar angle of 350 mrad to 520 mrad. A schematic view of the SVT is shown in Figure 3.4.

3.2.2 The Drift Chamber (DCH)

The drift chamber is designed for the reconstruction of the trajectories and momenta of charged particles with transverse momentum $p_{\mathrm{t}} > 100\,\mathrm{MeV}/c$. It also provides a dE/dx measurement with a resolution of 7% which allows π/K separation up to $700\,\mathrm{MeV}/c$.

The DCH is 276.4 cm long cylinder, which has an inner radius of 23.6 cm and an outer radius of 80.9 cm (see Figure 3.5). The drift chamber consists of 7104 hexagonal drift cells with a typical dimension 12 mm × 18 mm arranged in 40 layers. The sense wires have a diameter of $20\,\mu$m and are made of gold-plated Tungsten-rhenium, surrounded by six field wires with a diameter of $120\,\mu$m, made of gold-platet aluminum. A voltage of nominally 1960 V is applied to the sense wires. The DCH is operated with a mixture of Helium and Isobutane in the ratio 80% : 20%. This mixture has a radiation length of 807 m and drift velocity of $22\,\mu\mathrm{m}/\mathrm{ns}$.

3.2.3 The Cherenkov Detector (DIRC)

The DIRC was desighned for the identification of charged particles with momentum above $700\,\mathrm{MeV}/c$, in particular π/K separation up to $4\,\mathrm{GeV}/c$. The design is shown schematically in Figure 3.6.

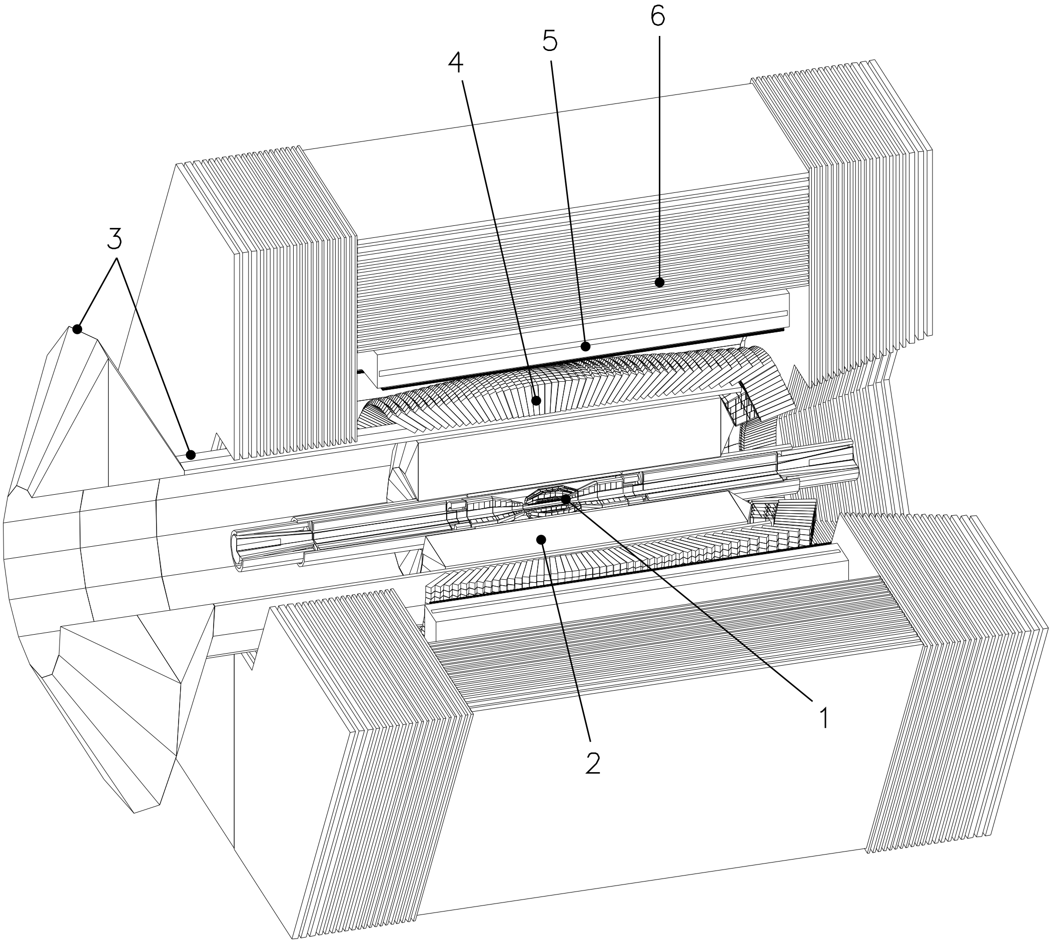

Figure 3.3: Schematic view of the *BABAR* detector with its sub-detectors: (1) SVT, (2) DCH, (3) DIRK, (4) EMC, (5) Magnet Coil, (6) IFR.

The DIRC consists of 144 bars of fused silica arranged in a 12-side polygonal barrel shape. Each bar is 4.9 m long, 17 mm thick, and 35 mm wide. The Cherenkov detector surrounds the drift chamber and its angular coverage is 87% in polar angle and 93% in azimuthal angle.
When charged particles traverse the quartz bars with a velocity larger than the speed of light in the medium, Cherenkov radiation is emitted. The photons are captured by internal total reflection and transported to the Stand Off Box (SOB) at the backward end of the detector, which is filled with 6000 liters of purified water. The rear of the SOB is instrumented with 11000 photo-multiplier tubes (PMTs) with 29 mm diameter. The Cherenkov angle θ_C provides a measurement of velocity $\beta = v/c$:

$$cos\Theta_C = \frac{1}{n\beta} \qquad \text{with } n \approx 1.473. \tag{3.1}$$

Together with the measured momentum from the drift chamber a mass hypothesis for the

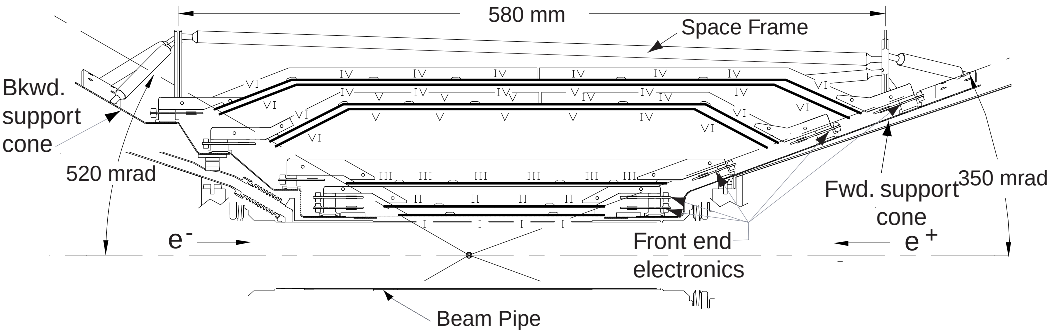

Figure 3.4: Longitudinal section through the SVT

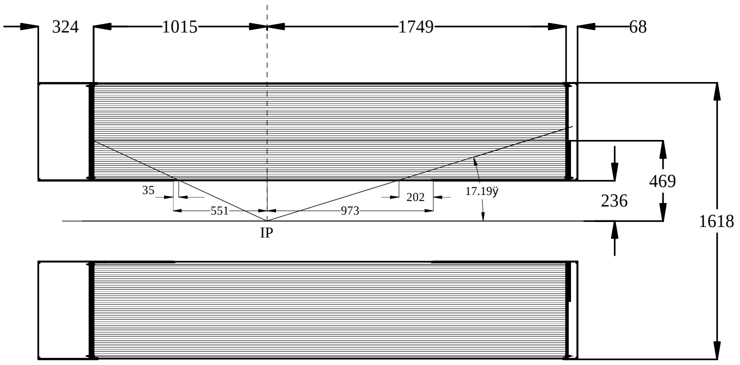

Figure 3.5: The geometry of the DCH.

charged particle can be tested.

3.2.4 The Electromagnetic Calorimeter (EMC)

The electromagnetic calorimeter was designed to measure electromagnetic shower with excellent efficiency, angle resolution and anergy resolution over the energy range from 20 MeV to 9 GeV. In addition, it is used to identify electrons or positrons. The EMC is made of 6580 thallium-doped cesium iodide crystals, which are grouped into a barrel region and an endcap region:

1. The cylindrical barrel section consists of 48 axially symmetric rings of 120 crystals each. The angular coverage is

$$\begin{aligned} -0.775 &\leq \cos\theta_{\mathrm{lab}} \leq 0.962\,, \\ -0.916 &\leq \cos\theta_{\mathrm{cms}} \leq 0.895\,. \end{aligned}$$

2. The forward conic endcap is made of 8 rings. It is composed of two rings of 80 crystals, three rings of 100 crystals , and three rings of 120 crystals. The angular

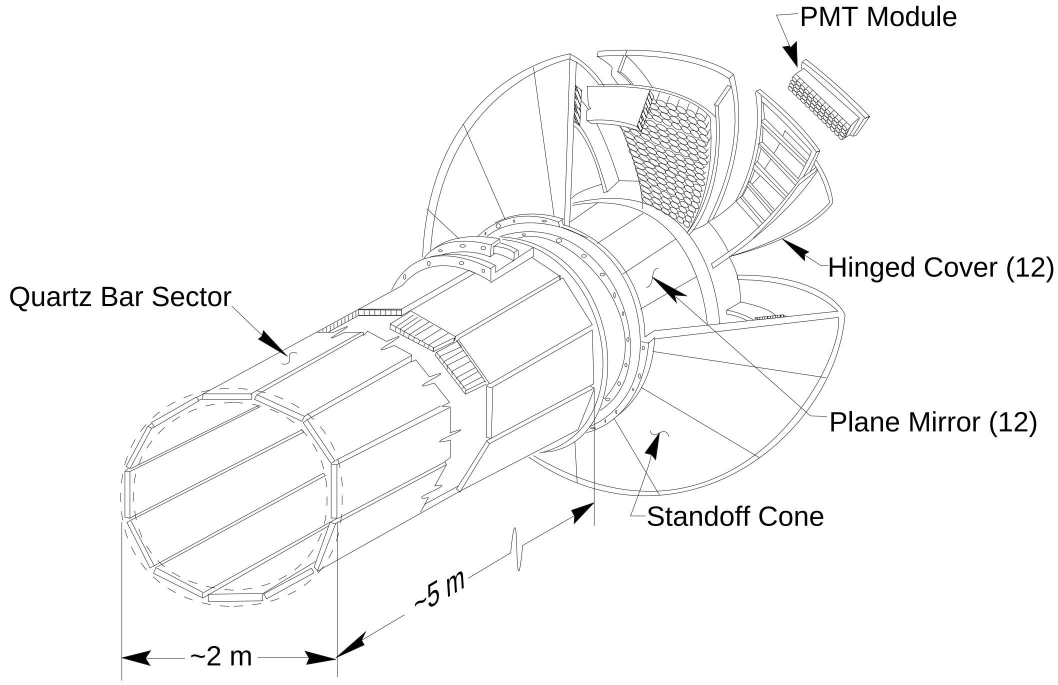

Figure 3.6: Schematic view of the DIRC.

coverage of the endcap is

$$
\begin{aligned}
-0.775 &\leq \cos\theta_{\text{lab}} \leq 0.892\,,\\
-0.916 &\leq \cos\theta_{\text{cms}} \leq 0.715\,.
\end{aligned}
$$

A schematic view of the EMC is shown in Figure 3.7.
Due to the short radiation length, $X_0 = 1.85\,\text{cm}$, and small Moliére radius, $R_m = 3.8\,\text{cm}$, of the crystals electromagnetic clusters are almost fully contained in the detector and can be measured precisely. Mounted on the back of each crystal, two silicon PIN diodes and pre-amplifiers collect the scintillation light. This redundancy makes it possible to read out a chanel even if a single diode or pre-amplifier has failed.

3.2.5 The Instrumented Flux Return (IFR)

All above described sub-detectors are surrounded by a superconducting solenoid coil with an inner radius of 1.42 m, an outer radius of 1.73 m, and a length of 3.85 m. The coil operates at a current of 4.6 kA. It results in a magnetic field of 1.5 T.

The magnetic flux of the solenoid is returned in steel plates which are instrumented with Resistive Plate Chambers (RPC). The thickness of the steel plates varies from 2 cm for the innermost to 10 cm for the outermost plates. This system is called as Instrumented Flux Return (IFR) and is used to identify muons and neutral hadrons such as the K_L^0 meson.

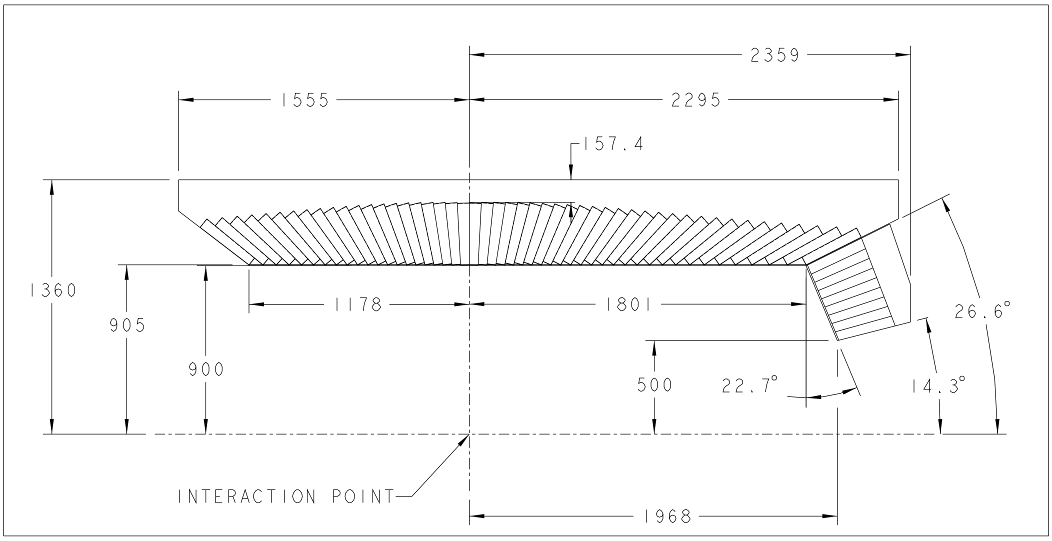

Figure 3.7: Longitudinal section through the EMC. The EMC consists of a cylindric barrel with 5760 CsI crystals and a forward conic endcap with 820 crystals. All dimensions are given in mm.

Due to problems with the linseed oil used in the manufacturing of the RPCs they have lost detection efficiency year by year. Therefore the RPCs have been replaces in two steps by Limited Streamer Tubes (LSTs) [32]. Between August and September 2004 the barrel's top and bottom sextants have been replaced, and during the shutdown between Run 5 and Run 6 (August 2006 to January 2007) the remaining barrel sextants have been replaced. However, data used in this analysis contains of a mix of data taken before and after the LST installation.

4 Analysis Strategy

4.1 Overview

The inclusive partial branching fraction, $\Delta\mathcal{B}$, of $B \to X_u l \nu$ decays will be measured by extracting yields in data and Monte Carlo in a restricted $B \to X_u e \overline{\nu}_e$ phase space region. The signal extraction procedure is described in detail in section 6.1.
The calculation of the $B \to X_u l \nu$ signal efficiency and the estimation of the $B\overline{B}$ background are based on the Monte Carlo simulation. Section 4.3 provides an overview of the modeling of signal and background events.

The main $B\overline{B}$ background contribution arises from $B \to X_c l \nu$ decays. The dominant part of the $b \to c$ consists $B \to D^* \ell \nu$ decays. Therefore, a high priority is to reduce the sensitivity of the partial branching measurement to uncertainties in the modeling of background decays by suppressing the $B \to X_c l \nu$ events. This can be done by selecting the phase space region for $B \to X_u l \nu$ decays where the production of the $B \to X_c l \nu$ events is kinematically suppressed.
In this analysis the region defined in the plane spanned by the electron energy and invariant mass squared of the electron-neutrino system (see Figure 2.5) is used to extract the $B \to X_u e \overline{\nu}_e$ signal yields. The contour in this plane defined as the invariant mass squared of the recoils system, $s_{\mathrm{h}}^{\mathrm{max}}$, represents the kinematical threshold ($s_{\mathrm{h}}^{\mathrm{max}} = m_D^2$) for the production of the D meson. Hence, no events with a true hadronic recoil mass above m_D can enter the $B \to X_u e \overline{\nu}_e$ sample unless q^2 or E_e is mis-reconstructed.

Semileptonic B decays are selected using requirements outlined in section 4.4.1. Refined selection criteria for charged tracks, photons and composite particles are applied to improve the quality of the neutrino reconstruction and to ensure good agreement between data and the Monte Carlo simulation.
A special technique is developed to identify and to remove $B \to D^* \ell \nu$ decays which is described in detail in section 4.6.
Section 4.8 gives an overview of further criteria applied to the events to guarantee a good quality of the neutrino reconstruction and to optimize the signal to background ratio. In addition, the refined selection criteria are optimized to suppress the continuum ($e^+e^- \to q\overline{q}, q = u, d, s, c$) events, estimated from the off-peak data.

An independent control sample (see chapter 5) is used to reduce the dependence of the signal efficiency on the Monte Carlo simulation. The evaluation of the systematic uncertainties is described in detail in chapter 7.

4.2 Data Sets

Table 4.1 shows a summary of all data sets used in this analysis. The integrated luminosity summarized over all runs is 413.0 fb^{-1} on-peak data (corresponding to 454.2 million $B\overline{B}$ meson pairs) and 41.2 fb^{-1} off-peak data. The off-peak data has been recorded 40 MeV/c^2 below the $\Upsilon(4S)$ resonance.

Table 4.1: Summary of all data runs used in this analysis

Dataset	$\mathcal{L}$ [fb^{-1}]	# $B\overline{B}$ pairs [Mio.]
HardElectronFilter-Run1-OnPeak-R22d-v04	20.4	22.4
HardElectronFilter-Run2-OnPeak-R22d-v04	61.1	67.4
HardElectronFilter-Run3-OnPeak-R22d-v04	32.3	35.6
HardElectronFilter-Run4-OnPeak-R22d-v04	100.3	110.4
HardElectronFilter-Run5-OnPeak-R22d-v04	132.9	146.8
HardElectronFilter-Run6-OnPeak-R22d-v04	66.1	71.6
Total On-peak	413.0	454.2
HardElectronFilter-Run1-OffPeak-R22d-v04	2.6	-
HardElectronFilter-Run2-OffPeak-R22d-v04	6.9	-
HardElectronFilter-Run3-OffPeak-R22d-v04	2.5	-
HardElectronFilter-Run4-OffPeak-R22d-v04	10.1	-
HardElectronFilter-Run5-OffPeak-R22d-v04	14.5	-
HardElectronFilter-Run6-OffPeak-R22d-v04	4.6	-
Total Off-peak	41.2	-

4.3 Monte Carlo Simulation

In this analysis the Monte Carlo (MC) simulation is used to understand the performance of the detector and to estimate backgrounds and the $B \to X_u e \overline{\nu}_e$ signal efficiency. Monte Carlo events have been produced by the BABAR collaboration at various computing centers. The GEANT4 [33] simulation package is used to simulate interactions between particles and detector material.
Table 4.2 shows a summary of used Monte Carlo events from a *generic* sample where both B mesons decay generically. The luminosity scaling factor of $B\overline{B}$ events with respect to the on-peak luminosity is $F_{B\overline{B}} = \mathcal{L}_{\text{on}}/\mathcal{L}_{B\overline{B}} = 0.323$. The large *generic* $B\overline{B}$ sample (~ 1400 million $B\overline{B}$ pairs) contains $B \to X_u l \nu$ signal events as well as an admixture of background events. The next subsections will describe both event categories and their simulation in more detail.

4.3.1 Simulation of Signal Events

The resonant as well as the non-resonant $B \to X_u l \nu$ decays are simulated as a part of generic $B\overline{B}$ Monte Carlo.
The branching fractions for various resonant (X_u is explicitly reconstructed) decay modes used in the simulation are listed in Table 4.3. These decays are generated using the ISGW2 model [13]. The branching fraction of the resonant decay modes in SP8 simulation were then reweighted to the latest values obtained from world average [34] and results proposed by the semileptonic Analysis Working Group (AWG) [35] of the BABAR collaboration.

A non-resonant part of $B \to X_u l \nu$ decays is generated according to the triple differential decay width $\frac{d\Gamma_{ul\nu}}{dm_{X_u} dE_l dq^2}$ described in section 2.2.2.1. The hadronization of the X_u system is treated by the JETSET Monte Carlo generator [36]. It is not able to produce neither

Table 4.2: Summary of all Monte Carlo datasets used in this analysis

Dataset	$\mathcal{L}$ (fb^{-1})	# $B\bar{B}$ pairs [Mio.]
SP-1235-HardElectronFilter-Run1-R22d-v04	66.7	36.7
SP-1235-HardElectronFilter-Run2-R22d-v04	87.5	103.1
SP-1235-HardElectronFilter-Run3-R22d-v04	90.5	49.8
SP-1235-HardElectronFilter-Run4-R22d-v04	305.4	168.0
SP-1235-HardElectronFilter-Run5-R22d-v04	444.0	244.2
SP-1235-HardElectronFilter-Run6-R22d-v04	183.3	100.8
Total $B^+ B^-$	1277.4	702.6
SP-1237-HardElectronFilter-Run1-R22d-v04	67.6	37.2
SP-1237-HardElectronFilter-Run2-R22d-v04	187.9	103.4
SP-1237-HardElectronFilter-Run3-R22d-v04	88.1	48.5
SP-1237-HardElectronFilter-Run4-R22d-v04	304.2	167.3
SP-1237-HardElectronFilter-Run5-R22d-v04	438.6	241.2
SP-1237-HardElectronFilter-Run6-R22d-v04	192.3	105.2
Total $B^0 \bar{B}^0$	1278.8	702.8

hadronic states with masses below $2m_\pi$ nor any resonant structure in the hadronic mass spectrum.

Since neither the resonant nor the non-resonant generators alone provide a realistic simulation of $B \rightarrow X_u l \nu$ decays the so-called Hybrid Model is used to achieve a more realistic simulation. According to this model the sample of simulated $B \rightarrow X_u l \nu$ events contains a mix of resonant and non-resonant $B \rightarrow X_u l \nu$ decays.

The Hybrid Model is defined by:

$$H_i = R_i + \omega_i N_i, \tag{4.1}$$

where ω_i is a weight and H_i, R_i, and N_i give the numbers of total (hybrid), resonant and non-resonant $B \rightarrow X_u l \nu$ events for each bin i, respectively. The bins correspond to a $8 \times 8 \times 8$ array defined in the three dimensional phase space of the invariant mass of X_u system, m_{X_u}, lepton energy, E_l, and lepton-neutrino invariant mass squared, q^2. Table 4.4 shows the segmentation of the phase space.

The weights ω_i have to be evaluated in such a way that the equation (4.1) is satisfied for each bin i. In addition, the total $B \rightarrow X_c l \nu$ production rate (resonant plus non-resonant) in generic $B\bar{B}$ simulation is corresponding to the total branching fraction, $\mathcal{B}_{\mathrm{tot}}^{X_u l \nu}$, listed in Table 4.3.

In order to determine the weight ω_i, a generator-level Monte Carlo simulation[1] is used. In this context two $B \rightarrow X_u l \nu$ samples, resonant and non-resonant, are generated. The branching fractions of resonant decays were set to reflect the most recent values listed in Table 4.3. The overall normalization of the resonant and non-resonant components of the hybrid model is adjusted to reproduce the total $B \rightarrow X_u l \nu$ branching fraction (see also Table 4.3). The two Monte Carlo samples are then mixed such that the fraction of hybrid events

---

[1] Detector simulation is not included

Table 4.3: Summary of branching fractions of $B \to X_u l\nu$ decay modes. Nominal (SP8) branching fractions in simulation are reweighted to the most recent (new) obtained from world average [34] and results proposed by semileptonic AWG [35]. All branching fractions are expressed in units of $\times 10^{-4}$.

Decay mode	$\mathcal{B}_{SP8}(B^+)$	$\mathcal{B}_{new}(B^+)$	$\mathcal{B}_{SP8}(B^0)$	$\mathcal{B}_{new}(B^0)$
$B \to \pi l\nu$	0.72	0.75 ± 0.05	1.33	1.39 ± 0.09
$B \to \rho l\nu$	1.45	1.29 ± 0.20	2.69	2.38 ± 0.38
$B \to \eta l\nu$	0.84	0.84 ± 0.34	–	–
$B \to \eta' l\nu$	0.84	0.84 ± 0.84	–	–
$B \to \omega l\nu$	1.45	1.30 ± 0.54	–	–
$B \to X_u l\nu$ (non res.)	19.48	19.72 ± 3.35	18.92	18.29 ± 3.26
Total $B \to X_u l\nu$	24.78	23.74 ± 3.52	22.94	22.06 ± 3.28

Table 4.4: Segmentation of the $B \to X_u l\nu$ phase space in m_{X_u}, E_l and q^2. The phase space is divided in $8 \times 8 \times 8$ bins. The shown values correspond to the lower edge of a given bin.

	1	2	3	4	5	6	7	8
m_{X_u} [GeV/c^2]	0.0	1.4	1.6	1.8	2.0	2.5	3.0	3.5
E_l [GeV]	0.00	0.50	1.00	1.25	1.50	1.75	2.00	2.25
q^2 [(GeV/c^2)^2]	0.0	2.5	5.0	7.5	10.0	12.5	15.0	20.0

for a given bin i, $H_i/\sum_k H_k$, is the same as for the non-resonant sample, $N_i/\sum_k N_k$. This gives

$$\mathcal{B}_{\text{res}}^{X_u l\nu} R_i + \omega_i \mathcal{B}_{\text{non-res}}^{X_u l\nu} N_i = \mathcal{B}_{\text{tot}}^{X_u l\nu} N_i, \tag{4.2}$$

where $\mathcal{B}_{\text{res}}^{X_u l\nu}$ is the sum of all resonant, $\mathcal{B}_{\text{non-res}}^{X_u l\nu}$ the non-resonant and $\mathcal{B}_{\text{tot}}^{X_u l\nu}$ the total $B \to X_u l\nu$ branching fractions. The weight ω_i is then evaluated for B^0 as well as for B^+ decays.

Figures 4.1 to 4.3 show kinematic distributions of the hybrid model compared to those of the non-resonant sample.

The above described technique has been implemented as a WebTool [37] which allows to compute all weights depending on the input parameters such as branching fractions or Shape Function parameters used to generate the non-resonant and resonant $B \to X_u l\nu$ events. The WebTool is used in this analysis in particular in the systematic studies described in section 7.2.

4.3.2 HQE parameters

The non-resonant part of the $B \to X_u l\nu$ events in Monte Carlo simulation is generated using Shape Function parameter values $a = 2.27$ and $m_b = 4.62$. Following the suggestion of the semileptonic AWG [35], more recent values of the HQE parameters λ_1 and $\overline{\Lambda}$ are to be

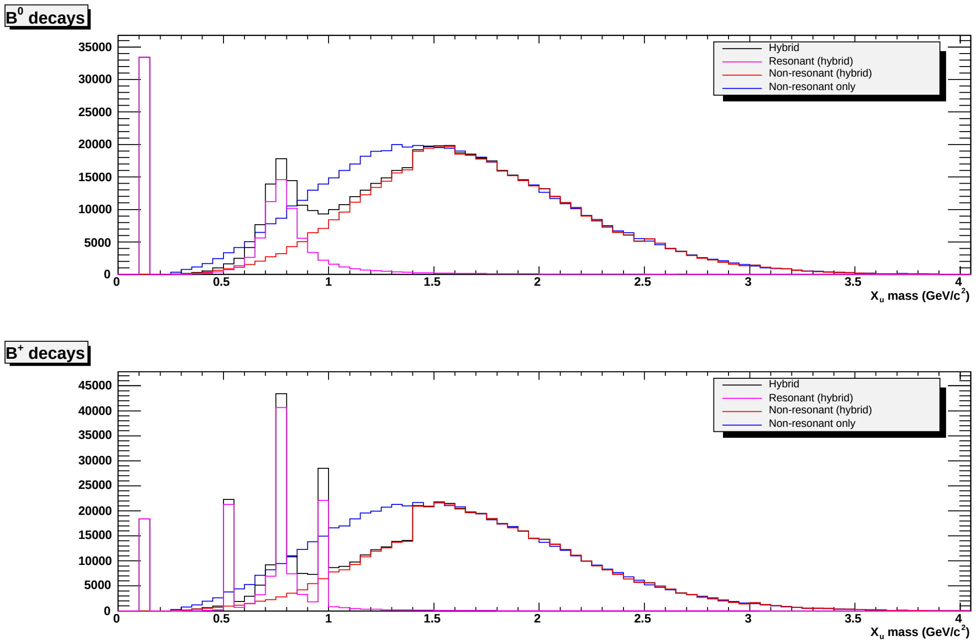

Figure 4.1: Mass spectrum of X_u system for B^0 and B^+ decays in hybrid Monte Carlo events.

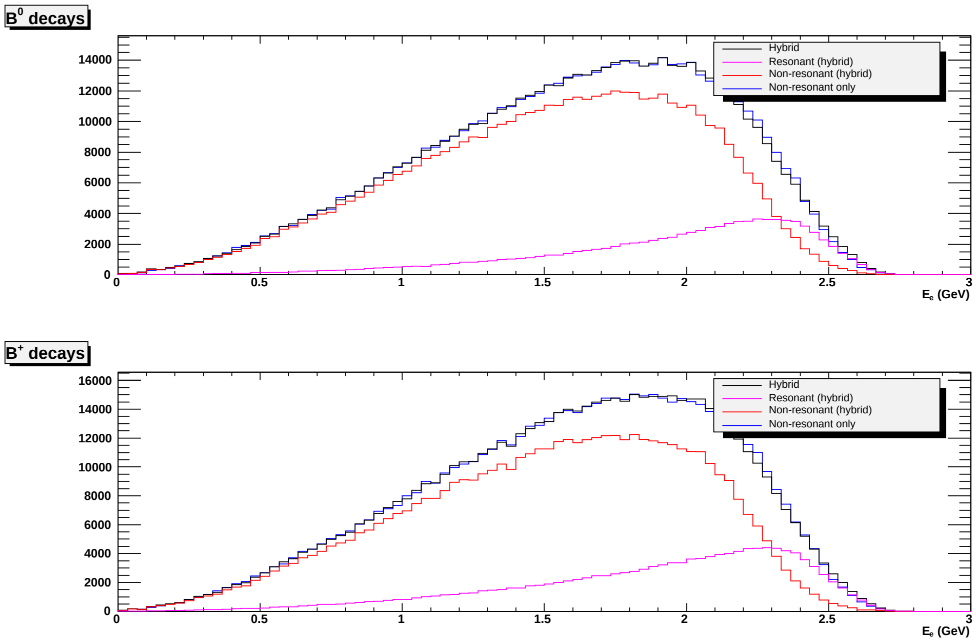

Figure 4.2: Electron energy spectrum for B^0 and B^+ decays in hybrid Monte Carlo events.

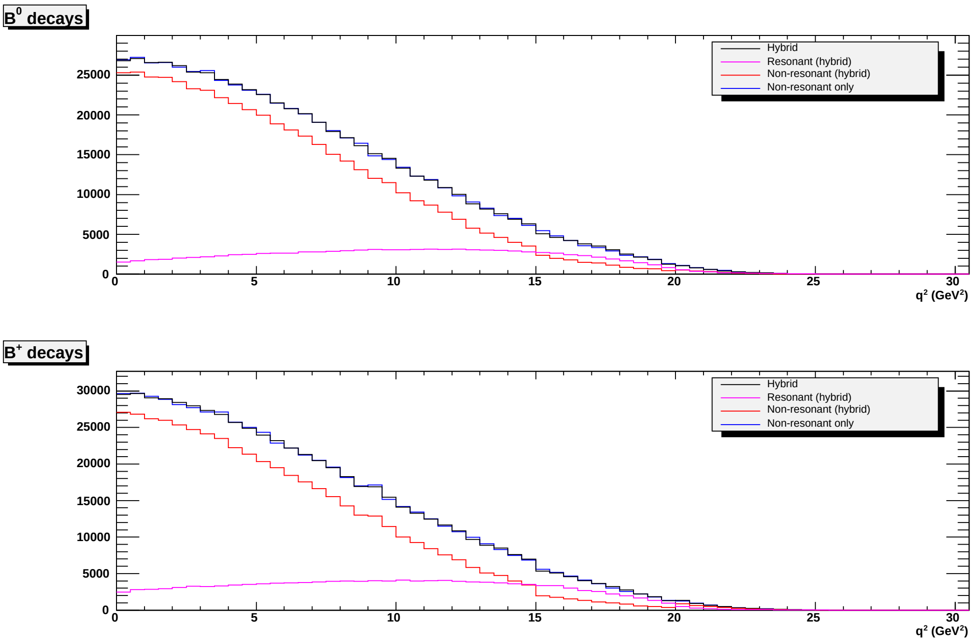

Figure 4.3: q^2 spectrum spectrum for B^0 and B^+ decays in hybrid Monte Carlo events.

used. These results are obtained from the global HQE fit to moments of inclusive $B \to X_c l \nu$ and $B \to X_s \gamma$ events [22]. The values of this fit in the Kagan-Neubert scheme [25] are

$$\overline{\Lambda} = (0.621 \pm 0.041)\,\mathrm{GeV}, \qquad \lambda_1 = (-0497 \pm 0.086)\,\mathrm{GeV}^2, \qquad \rho = -0.17,$$

where ρ is the linear correlation coefficient between $\overline{\Lambda}$ and λ_1. Using equation (2.40), the HQE parameters were translated into Shape Function parameters $a = 1.33$ and $m_b = 4.66$ which are used to reweight the non-resonant part of $B \to X_u l \nu$ events using the WebTool [37].

4.3.3 Background Simulation

In order to estimate the $B\bar{B}$ background in this analysis, the generic $B\bar{B}$ Monte Carlo simulation is used. The background may be classified into four categories: $B \to D^* \ell \nu$, $B \to D \ell \nu$, $B \to X_c^{\mathrm{rest}} l \nu$, and $B \to X_{\mathrm{other}} l \nu$ (other) backgrounds. The other background consists of events where charged tracks have been misidentified as leptons (fakes) or leptons are produced in secondary decays (cascades). The events denoted as $B \to X_c^{\mathrm{rest}} l \nu$ events are resonant $B \to D^{**} l \nu$ and non-resonant $B \to D^{(*)} \pi l \nu$ decays. The D^{**} states are either: narrow D_1 and D_2^* or broad D_0^* and $D_1^{'}$ types.
Table 4.5 gives the overview of relevant branching fractions of $B \to X_c l \nu$ decays in nominal (SP8) Monte Carlo simulation and values used to modify the simulation in order to reflect the most recent measurements.

Table 4.5: Summary of branching fractions of $B \to X_c l \nu$ decay modes. Nominal (SP8) branching fractions in simulation are reweighted to the most recent values (new) obtained from world average [34] and results reported in [38]. All branching fractions are expressed in units of $\times 10^{-2}$.

Decay mode	$\mathcal{B}_{SP8}(B^+)$	$\mathcal{B}_{new}(B^+)$	$\mathcal{B}_{SP8}(B^0)$	$\mathcal{B}_{new}(B^0)$
$B \to D l \nu$	2.24	2.28 ± 0.11	2.07	2.17 ± 0.12
$B \to D^* l \nu$	6.17	6.09 ± 0.29	5.70	5.16 ± 0.11
$B \to D_1 \ell \nu$ (narrow)	0.56	0.50 ± 0.08	0.52	0.54 ± 0.06
$B \to D_2^* \ell \nu$ (narrow)	0.3	0.39 ± 0.07	0.23	0.42 ± 0.08
$B \to D_0^* \ell \nu$ (broad)	0.49	0.43 ± 0.09	0.45	0.45 ± 0.09
$B \to D_1' \ell \nu$ (broad)	0.9	0.40 ± 0.20	0.83	0.45 ± 0.20
$B \to D^0 \pi \ell \nu$	0.10	0.40 ± 0.12	0.20	0.20 ± 0.06
$B \to D^{\pm} \pi \ell \nu$	0.19	0.19 ± 0.06	0.10	0.40 ± 0.12
$B \to D^{*0} \pi \ell \nu$	0.03	0.12 ± 0.04	0.07	0.06 ± 0.02
$B \to D^{*\pm} \pi \ell \nu$	0.06	0.06 ± 0.04	0.03	0.12 ± 0.04
$B \to X_c l \nu$	11.04	10.89 ± 0.16	10.2	10.15 ± 0.16

4.4 Event Selection

4.4.1 Event Preselection

All events in this analysis have to pass a loose preselection to satisfy the L3 trigger and the background filter criteria:

- $N_{\text{tracks}} \geq 3$: number of charged tracks in the event.
- $R_2 < 0.98$: ratio of the second to first Fox-Wolfram moment [39]. The cut on R_2 is a powerful method to discriminate $B\bar{B}$ events from lepton-pair background and light-quark $e^+e^- \to q\bar{q}$ $(q = u,d,s,c)$ continuum events, where the latter have jet-like event shapes and tend to have large R_2 values.
- at least one electron (further called signal electron) must be identified with an electron energy, $E_e > 1.4\,\text{GeV}$, in the $\Upsilon(4S)$ rest frame. Because of the larger fake rates in muon reconstruction, only semileptonic $B\bar{B}$ decays to electrons are considered.

In order to reject Bhabha events ($e^+e^- \to e^+e^-$) , the veto developed in [40] is applied. It requires the event to have a multiplicity, N_{tot}, greater than five objects

$$N_{tot} = N^{'}_{\text{tracks}} + N^{'}_{\gamma}/2 > 5,$$

where $N^{'}_{\gamma}$ is the number of photons with a single photon energy of $E_\gamma > 80\,\text{MeV}$ and identified as $\gamma \to e^+e^-$ pairs, and $N^{'}_{\text{tracks}}$ is the number of tracks which are not a part of identified $\gamma \to e^+e^-$ pairs. The events where Bhabha electrons interact with detector material and produce an electromagnetic shower can not be rejected using the veto described above. For such an event, an additional requirement is applied

$$\frac{\sum_i E_i^{show}}{\sum_i |\vec{P}_i|} < 0.9,$$

where E_i^{show} is the shower energy in the EMC and $|\vec{P}_i|$ the momentum of the i-th charged track in the event. In case of high multiplicity Bhabha events, where most of the charged particles are electrons, this ratio is close to 1. Alternatively, the more restricted requirements on R_2 can be used to eliminate such high multiplicity Bhabha events. However, this can be result in higher systematic uncertainties, as has been shown in Ref. [41].

4.4.2 Charged Track Selection

The reconstruction of charged tracks is based on the information from the SVT and the DCH. The standard track lists were defined at a very early stage in BABAR before the performance of the detector was fully understood. Therefore a refined tracks selection is needed to improve the quality of the track reconstruction. All data as well as all Monte Carlo data sets used in this analysis have to pass the *TrkFixup* procedure developed in [42]. The *TrkFixup* algorithm provides a charged tracks list based on detailed tracking information with a higher tracking efficiency and low fake rate. In this context the background tracks, so-called “ghost” tracks, looper tracks and tracks from material interaction are identified and removed from the analysis. Nevertheless, additional requirements are made at the analysis level to improve the track selection:

- $0.41 < \theta_{lab} < 2.54$ (radians), the angle of the track in the lab frame;
- $p_{lab} < 10\,\mathrm{GeV}/c$, the momentum of the track in the lab frame;
- $p_{t,lab}^{DCH} > 0.06\,\mathrm{GeV}/c$, the transverse momentum of the tracks with DCH hits;
- $0.06\,\mathrm{GeV}/c < p_{t,lab}^{SVT} < 0.2\,\mathrm{GeV}/c$, the transverse momentum of the tracks with SVT hits only;
- $|DOCA| < 1.5\,\mathrm{cm}$, the distance of closest approach of the track to the z axis;
- $|z_0| < 5\,\mathrm{cm}$, the distance in the z direction from the origin of the coordinate system;
- track is not a looper (see below);
- track is not a “ghost” (see below).

Looper tracks: charge particles with low momenta that loop within the DCH and do not reach the EMC. Looping tracks with a radius of half of the DCH radius ($r_{\mathrm{loop}} \approx 40\,\mathrm{cm}$) are possible for tracks originating from the interaction point with transverse momenta $p_t \lesssim 200\,\mathrm{MeV}$. The tracking algorithms, however, usually reconstruct loop tracks as several smaller segments, each of them describing one half-turn of the helix. Thus, multiple reconstructed tracks originate from one physical particle, which need to be reduced to one single track. In order to identify loopers a set of tracks must satisfy the following criteria:

- $p^i_{t,lab} < 0.25\,\mathrm{GeV}/c$
- $|\Delta p_{t,lab}| = |p^i_{t,lab} - p^j_{t,lab}| < 0.12\,\mathrm{GeV}/c$
- $|cos\theta^i_{lab}| < 0.2$
- $|\Delta\phi_{lab}| < 0.1$
- $|\Delta\theta_{lab}| < 0.1$ for same-charge pairs
- $|\pi - |\Delta\theta_{lab}|| < 0.1$ for opposite-charge pairs.

Finally, only a track produced closest to the interaction point is retained while the remaining looper tracks are rejected.

"Ghost" tracks: In the case of "ghost" tracks the hits in DCH left by only one charged particle are associated with two or more charged tracks. "Ghost" tracks are identified if a pair of tracks satisfies the following:

- $p^i_{t,lab} < 0.35\,\mathrm{GeV}/c$
- $|\Delta p_{t,lab}| = |p^i_{t,lab} - p^j_{t,lab}| < 0.15\,\mathrm{GeV}/c$
- $|cos\theta^i_{lab}| < 0.2$
- $|\Delta\phi_{lab}| < 0.1$
- $|\Delta\theta_{lab}| < 0.1$
- N^{DCH}_{hits}(track i)+N^{DCH}_{hits}(track j)< 45.

For such pairs of tracks, only the track with the greatest number of DCH hits is used in the analysis.

The above described refined track selection is a result of detailed studies performed in [43] and in [44] particularly for semileptonic B decays. All charged tracks not passing the above described selection cuts are not used in the further analysis.

4.4.3 Neutral Candidate Selection

All neutral clusters measured in the EMC and not matched to any charged track are considered in this analysis as photons. The selection criteria for neutral candidate selection is detailed in [43] and is summarized below. Requirements are made for:

- $N_{\mathrm{crystal}} > 2$, the number of crystals in the cluster;
- $E_{\mathrm{crystal}} > 0.05\,\mathrm{GeV}$, the energy of the cluster in the lab frame;
- $LAT < 0.6$, the cluster lateral moment [45];
- $0.32 < \theta_{cluster} < 2.44$ (radians), the angle of the cluster in the lab frame;
- $\Delta\alpha = arccos[cos\theta_{clus}cos\theta_{trk} + sin\theta_{clus}sin\theta_{trk}cos(\phi_{clus} - \phi_{trk})] < 0.08$, the $3D$ angle difference $\Delta\alpha$ between the position of the cluster and the impact point of the nearest charged track which is not identified as an electron at the EMC surface.

All photons not satisfying the above selection are removed from the analysis.

4.4.4 Selection of Composite Particle Candidates

The study in [43] has shown that the quality of reconstruction of the visible energy and hence the neutrino reconstruction can be improved by using composite particles instead of their daughter track(s). The reconstructed composite particles are:

- $K_S^0 \rightarrow \pi^+\pi^-$, with decay a length $> 2\,\mathrm{mm}$ and invariant mass within $0.4906\,\mathrm{GeV}/c^2 < m_{\pi^+\pi^-} < 0.5047\,\mathrm{GeV}/c^2$;
- $\Lambda \rightarrow p\pi^-$, with a decay length $> 5\,\mathrm{mm}$ and a mass satisfying $1.112\,\mathrm{GeV}/c^2 < m_{p\pi^-} < 1.120\,\mathrm{GeV}/c^2$;
- $\gamma \rightarrow e^+e^-$, with $m_{e^+e^-} < 0.03\,\mathrm{GeV}/c^2$;
- $J/\psi \rightarrow l^+l^-$, using cuts defined for the reconstruction of the default J/ψ candidate list [46].

The set of composite particle candidates satisfying the selection criteria described above are then examined. If the association between a daughter track making a composite particle candidate to a track in the charged track list was lost the composite candidate is rejected. In addition, if composite particles are found to share a common daughter tracks, then these composites are rejected. Finally, all daughter tracks from the final set of accepted composite particle candidates are removed from the charged track list.

4.4.5 Particle Identification

The neutrino reconstruction requires a best mass hypothesis for each accepted track. In order to identify electrons, muons, protons and kaons, standard BABAR particle identification algorithms are used. To assign the best particle hypothesis to a given charged track the selectors in the order described below are examined. In the case of a positive response the corresponding mass hypothesis is applied:

1. Is a track in the list of electrons defined by the electron selector, *PidLHElectronSelector* [47]?
2. Is a track in the list of kaons defined by the kaon selector, *VeryTightNNKaonMicroSelection* [48]?
3. Is a track in the list of muons defined by the muon selector, *NNVeryTightMuonSelection* [49]?
4. Is a track in the list of protons defined by the proton selector, *VeryTightLHProtonSelection* [50]?

The tracks not found in the lists described above are assumed to be pions.

4.5 Neutrino Reconstruction

The four-momentum of the neutrino, p_ν, is reconstructed from all of the decay products of the $\Upsilon(4S)$. The visible four-momentum, p_{vis}, can be computed as the sum of momenta of all accepted charged tracks, photons and composite particles in the $\Upsilon(4S)$ rest frame

$$p_{\text{vis}} = \sum_i p_{i,\text{track}} + \sum_i p_{i,\text{photon}} + \sum_i p_{i,\text{comp}}. \tag{4.3}$$

The missing four-momentum is then calculated as

$$p_{\text{miss}} = (E_{\text{miss}}, P_{\text{miss}}) = p_{\Upsilon(4S)} - p_{\text{vis}} \tag{4.4}$$

where $p_{\Upsilon(4S)}$ is the $\Upsilon(4S)$ four-momentum with $|P_{\Upsilon(4S)}| = 0$ and energy equal to to the $\sqrt{s}$ of the e^+e^- initial state.
To obtain a better estimator for the neutrino four-momentum the magnitude of the missing momentum, $|P_{\text{miss}}|$, is used instead of the missing energy, E_{miss}. $|P_{\text{miss}}|$ is less sensitive than E_{miss} to the effects caused by additional or missing particles because it involves the vector sum of the true missing momentum and the momentum vectors of additional missing particles. Some cancellations can occur in the vector sum that do not occurr in the scalar sum, E_{miss}. Nevertheless, the missing momentum vector is a biased estimator of the true neutrino momentum. Studies performed in [1] have shown that this bias is arising mainly from the presence of K_L^0 or additional neutrinos in an event. Due to a low identification efficiency of K_L^0 mesons no dedicated veto is applied to these particles. Additional neutrinos are partially removed by requiring that the signal electron was to be the only identified lepton in the event ($N_{\text{lep}} = 1$). The remaining bias originates from sources such as misreconstructed or lost particles, double counting of deposited energy (e. g. looper and ghost tracks), etc. To reduce this bias and to improve the neutrino four-momentum estimate, detailed studies using $B \to X_u e \overline{\nu}_e$ Monte Carlo simulation are performed. Figure 4.4 shows the observed bias from Monte Carlo studies for signal $B \to X_u e \overline{\nu}_e$ events after applying the selection requirements outlined in section 4.8 with exception of E_e and $s_{\text{h}}^{\text{max}}$cuts. Two linear functions are fitted, $f_1(|P_{\text{miss}}|)$ and $f_2(|P_{\text{miss}}|)$, in the regions $|P_{\text{miss}}| < 2.125\,\text{GeV}/c$ and $|P_{\text{miss}}| > 2.125\,\text{GeV}/c$, respectively:

$$f_1(|P_{\text{miss}}|) = 0.179 - 0.244|P_{\text{miss}}| + |P_{\text{miss}}| \tag{4.5}$$

$$f_2(|P_{\text{miss}}|) = 1.569 - 0.907|P_{\text{miss}}| + |P_{\text{miss}}| \tag{4.6}$$

These functions can be used to remove the bias observed in the simulation. However, using both correction functions for the corresponding P_{miss} regions leads to an artificial peak[2] at $|P_{\text{miss}}| \approx 1.8\,\text{GeV}/c$ (see Figure 4.5) and hence to a non-physical distribution of the neutrino momentum, $|P_\nu|$, which is defined as $|P_\nu| = f_1(|P_{\text{miss}}|)$ for $|P_{\text{miss}}| < 2.125\,\text{GeV}/c$ and $|P_\nu| = f_2(|P_{\text{miss}}|)$ for $|P_{\text{miss}}| > 2.125\,\text{GeV}/c$. Since about $\sim 72\%$ of all $B \to X_u e \overline{\nu}_e$ events lie in the region $|P_{\text{miss}}| < 2.125\,\text{GeV}/c$, only the correction function $f_1(|P_{\text{miss}}|)$ is used in the further analysis to correct for the observed bias in the entire P_{miss} region. Figure 4.5 shows the distribution of $|P_{\nu,\text{true}}| - |P_\nu|$ as a function of $|P_\nu|$ and the corresponding $|P_\nu|$

---

[2] This peak is mainly caused by the second correction, f_2.

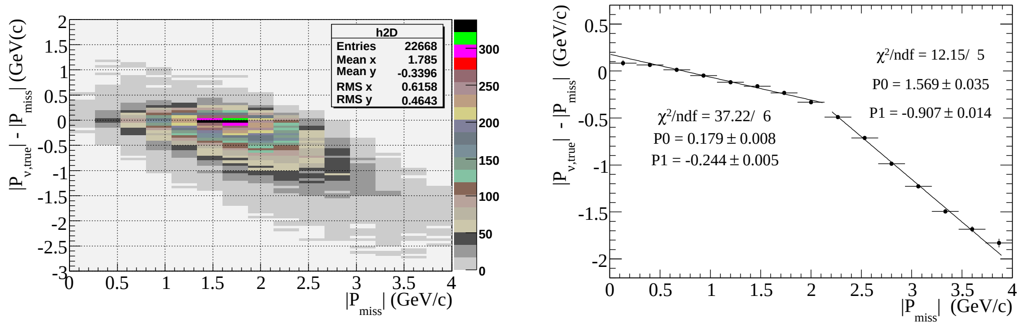

Figure 4.4: Generated $B \to X_u e \overline{\nu}_e$ neutrino momentum $|P_{\nu,\mathrm{true}}|$ minus $|P_{\mathrm{miss}}|$ as a function of $|P_{\mathrm{miss}}|$ (left), and the mean $|P_{\nu,\mathrm{true}}| - |P_{\mathrm{miss}}|$ value for 260 MeV/c bin in P_{miss} (right). In the latter plot, two linear functions are fitted to obtain a correction for the observed bias.

distribution. The neutrino three-momentum is then defined as

$$P_\nu = \frac{P_{\mathrm{miss}}}{|P_{\mathrm{miss}}|} f_1(|P_{\mathrm{miss}}|), \tag{4.7}$$

and the corresponding four-momentum as

$$p_\nu = (|P_\nu|, P_\nu). \tag{4.8}$$

Finally, the neutrino four-momentum in combination with the four-momentum of the signal electron is used to calculate the electron-neutrino invariant $q^2 = (p_e + p_\nu)^2$. Figure 4.6 shows the distributions of q^2 resolution without/with the correction applied for the neutrino estimator. One of the advantages of the improved q^2 resolution is that the migration of the signal $B \to X_u e \overline{\nu}_e$ events in the $q^2 - E_e$ region (described in details in section 6.1) can be minimized, which results in a better separation power between signal and $B \to X_c l \nu$ background using the $s_{\mathrm{h}}^{\mathrm{max}}$ cut.

4.6 Partial Reconstruction of $B \to D^* \ell \nu$ Decays

The main part of the $B \to X_c l \nu$ background are $B \to D^* \ell \nu$ decays. In order to reduce the sensitivity to the background estimation with a minimal loss of $B \to X_u e \overline{\nu}_e$ signal efficiency, such events can be vetoed. Further studies have shown (see Table 7.9) that also overall systematic uncertainties can be significantly reduced if the $B \to D^* \ell \nu$ veto is applied.
The $B \to D^* \ell \nu$ decays can be reconstructed in two ways:

1. “exclusive”: the B meson is fully reconstructed where the D^* particle is selected through its decay $D^* \to D\pi$, and the D meson is identified by means of a few final states.

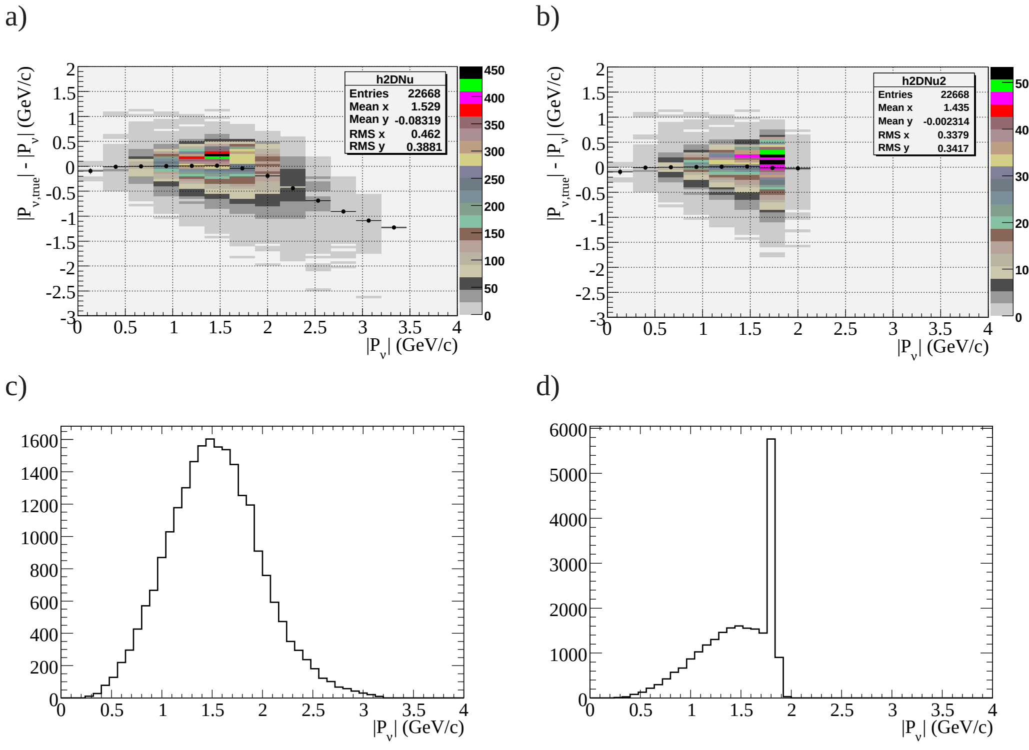

Figure 4.5: Generated $B \to X_u e \overline{\nu}_e$ $|P_{\nu,\mathrm{true}}|$ minus corrected $|P_\nu|$ neutrino momenta as a function of $|P_\nu|$ (top) and $|P_\nu|$ resolution (bottom). In the upper plots, the mean $|P_{\nu,\mathrm{true}}| - |P_\nu|$ value for 260 MeV$/c$ bin in $|P_\nu|$ is overlaid. The left plots show distributions where $|P_\nu|$ is corrected using only the function $f_1(|P_{\mathrm{miss}}|)$ (see text) and the right plots show distributions where two correction functions are applied to remove the observed bias in $|P_{\nu,\mathrm{true}}| - |P_{\mathrm{miss}}|$. The $|P_\nu|$ distribution (d) has an artificial peak at $|P_\nu| \approx 1.8\,\mathrm{GeV}/c$ due to correction using function $f_2(|P_{\mathrm{miss}}|)$.

2. “inclusive”: the B meson is partially reconstructed. The restricted phase space of the $D^{*} \to D\pi$ transition allows to select $B \to D^{*}\ell\nu$ events by reconstructing only the low-momentum pion, π_s ($\pi_s \equiv \pi^{\pm}/\pi^{0}$), from the D^{*} decay, without reconstructing D candidates.

The advantage of the partial reconstruction is that the number of identified $B \to D^{*}\ell\nu$ decays in a given sample is about ten times higher than the number of fully reconstructed events. However, this results in more combinatorial background and the higher probability to reject $B \to X_u e \overline{\nu}_e$ events.
The partial reconstruction technique is used in this analysis to identify the $B \to D^{*}\ell\nu$ decays as described below.

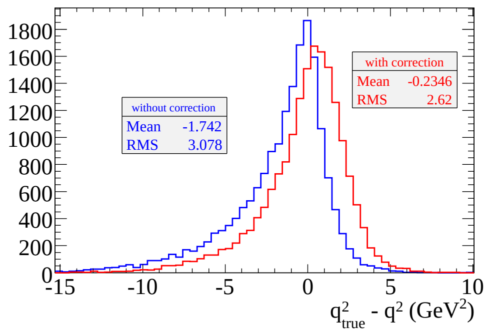

Figure 4.6: Distribution of signal $B \longrightarrow X_u e \overline{\nu}_e$ events for q^2 resolution without (blue) and with (red) the correction applied for the neutrino estimator. The resolution is computed as a difference between the generated (true) and the reconstructed q^2 quantity. The tail on the left side corresponds to events with additional unreconstructed particles.

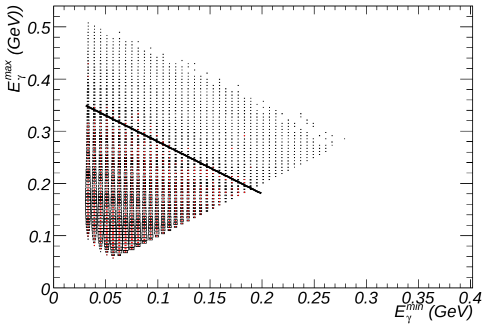

Figure 4.7: Distribution of E_γ^{max} vs. E_γ^{min} for slow neutral pions. The solid line represents a requirement (see text) made to separate pions from $B \longrightarrow D^* \ell \nu$ (red) decays from pions reconstructed as combinatorial background or from other decays (black).

4.6.1 Low-Momentum Pion Reconstruction

The low-momentum (slow) charged pion, $\pi^{\pm}$, is a candidate from the default charged track list with momentum in the range $0.05\,\mathrm{GeV}/c < |P_{\pi^{\pm}}| < 0.23\,\mathrm{GeV}/c$. The upper cut on the momentum represents the kinematical limit of the slow pions from $B \longrightarrow D^* \ell \nu$ decays as obtained from studies of Monte Carlo generator[3] events.

The neutral slow pion is reconstructed in the decay channel $\pi^0 \longrightarrow \gamma\gamma$ with an invariant mass $0.115\,\mathrm{GeV}/c^2 < m_{\gamma\gamma} < 0.150\,\mathrm{GeV}/c^2$ and with a momentum $|P_{\pi^0}| < 0.23\,\mathrm{GeV}/c$. In order to minimize the combinatorial background for the π^0 reconstruction an additional requirement is made. Figure 4.7 shows the two dimensional distribution of maximal, E_γ^{max}, and minimal, E_γ^{min}, energies of both photons entering in the reconstruction of each π^0 candidates. Only pions with daughters satisfying

$$E_\gamma^{max} < 0.38\,\mathrm{GeV} - E_\gamma^{min} \tag{4.9}$$

have been used in the further analysis. Due to this selection criterion about 20% of slow π^0 candidates from combinatorial background are rejected while the loss of true π^0 from $B \longrightarrow D^* \ell \nu$ decays is less than 0.3%.

4.6.2 Inclusive D^* Reconstruction

The D^* candidates are reconstructed in the decay channels $D^{*+} \longrightarrow D^0 \pi^+$, $D^{*+} \longrightarrow D^+ \pi^0$ and $D^{*0} \longrightarrow \overline{D}^0 \pi^0$. Due to the limited phase space available in the decay of D^* candidates

---

[3] Generator events are event where the `GEANT4` detector simulation is switched off.

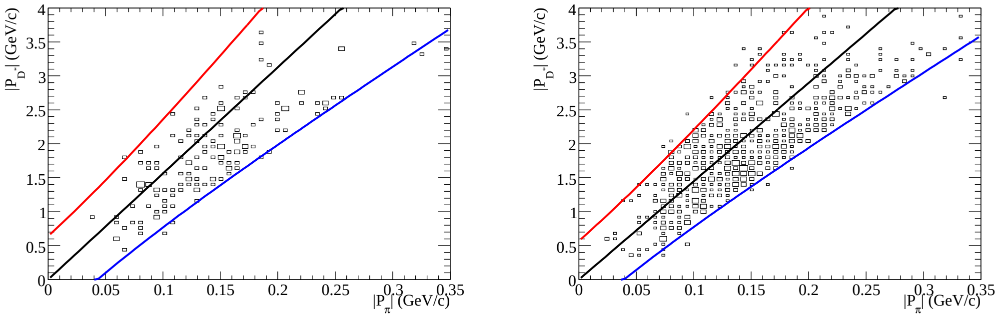

Figure 4.8: D^* momentum distribution as a function of the slow pion momentum for fully reconstructed $D^{*0} \to \bar{D}^0\pi^0$ (left) and $D^{*+} \to D^0\pi^+$ (right) events in $|P_{D^*}| - |P_\pi|$ plane. The solid lines represent, maximal in red, minimal in blue, and average in black, D^* momenta calculated as described in the text. The contributions above/below the maximal/minimal allowed momenta are due to the detector resolution.

the energies of slow pions in the D^* rest frame are 141 MeV and 145 MeV for π^0/π^+ respectively. The slow pions are emitted within a restricted cone centered around the D^{*+}/D^{*0} direction in the laboratory frame. It allows to compute the D^* four-momentum from the kinematic properties of the reconstructed slow π^0/π^+ candidate.

One of the solutions of the relativistic equation

$$\begin{pmatrix} E_{\pi_s} \\ |P_{\pi_s}| \end{pmatrix} = \begin{pmatrix} \gamma & \beta\gamma \\ \beta\gamma & \gamma \end{pmatrix} \begin{pmatrix} E_{\pi_s}^{cms} \\ |P_{\pi_s}^{cms}| \end{pmatrix} \tag{4.10}$$

which describes the two-body decay of D^* meson with

$$\gamma = \frac{E_{D^*}}{m_{D^*}} \qquad \beta = \frac{|P_{D^*}|}{E_{D^*}} \qquad cms \equiv D^* \text{ rest frame}$$

provides the maximal/minimal (±) kinematically allowed D^* momentum depending on the π_s momentum in the laboratory frame:

$$|P_{D^*}|^{\max/\min} = \frac{m_{D^*}}{m_\pi^2}(E_{\pi_s}^{cms}|P_{\pi_s}| \pm |P_{\pi_s}^{cms}|E_{\pi_s}). \tag{4.11}$$

E_{π_s} and $|P_{\pi_s}|$ are the slow pion energy and momentum measured in the laboratory frame, m_{D^*} and m_π the masses of the D^* and π mesons. $E_{\pi_s}^{cms}$ and $|P_{\pi_s}^{cms}|$ are the energy and the momentum of the slow pion calculated from two-body decay in the D^* rest frame.

The D^* four-momentum is then defined by identifying its polar and azimuth angles with the π_s ones, and computing its momentum as the average of the maximum and minimum momenta

$$|P_{D^*}|^{\text{ave}} = \frac{|P_{D^*}|^{\max} + |P_{D^*}|^{\min}}{2} = \frac{m_{D^*}}{m_{\pi_s}^2} E_{\pi_s}^{cms}|P_{\pi_s}| \tag{4.12}$$

calculated from the π_s kinematics. Figure 4.8 shows the dependency of the D^* momentum on the slow pion momentum in the laboratory frame obtained using truth $B \to D^*\ell\nu$ Monte Carlo events where decays $D^{*+} \to D^0\pi^+$ and $D^{*0} \to \bar{D}^0\pi^0$ were fully reconstructed.

4.6.3 $B \to D^*\ell\nu$ Veto Definition

The veto is defined by identifying B mesons in the decay channels: $B^- \to D^{*0}e^-\overline{\nu}$, $D^{*0} \to \bar{D}^0\pi^0$ and $\bar{B}^0 \to D^{*+}e^-\overline{\nu}$, $D^{*+} \to D^0\pi^+/D^+\pi^0$, using an ***Artificial Neural Network*** (**ANN**) described in detail in the following.

The ANN belongs to the class of Multilayer Perceptrons (MLP), which are feed-forward neural networks according to the propagation scheme shown in Figure 4.9. The neural network consists of one input layer, where the number of neurons is corresponding to the number of input variables, k hidden layers, and one output layer with two output classes. All neuron inputs to a given layer are linear combinations of the neuron outputs of the previous layer. The mathematical definition of a neuron of the hidden layer k at the position j is given as

$$X_j^{(k)} = A(w_{0j}^{(k)} + \sum_{i=1}^{M_{k-1}} w_{ij}^{(k)} X_i^{(k)}), \tag{4.13}$$

where A is an “activation function” that applies a weight to the output from one neuron based on the sum of the input. Here, a sigmoid “activation function” has been used

$$A(X) = (1+e^{-X})^{-1}. \tag{4.14}$$

In addition to the active neurons of each layer, there are bias neurons. These neurons have no input from the previous layer, but they are connected to each active neuron of the next layer. The bias neurons always emit $X_0^{(k)} = 1$ leading to an additional input weight $w_{0j}^{(k)}$ for the active neurons.

During the iterative training procedure the input weights w_{ij} of the neuron-neuron connections will be optimized to separate the two event classes. Afterwards, the trained ANN can be used to analyze a given data sample.

In this analysis the Toolkit for Multivariate Analysis [51] (TMVA) is used. The neural network is optimized to separate between two output classes $B \to D^*\ell\nu$ and $B \to X_u l\nu$ using Monte Carlo simulation. For each case, $D^* \to \pi^\pm$ and $D^* \to \pi^0$, a separate neural network has been built. The notation $D^* \to \pi^0$ implies decay channels $B^- \to D^{*0}e^-\overline{\nu}$, $D^{*0} \to \bar{D}^0\pi^0$ and $\bar{B}^0 \to D^{*+}e^-\overline{\nu}$, $D^{*+} \to D^+\pi^0$, and $D^* \to \pi^\pm$ the decays $\bar{B}^0 \to D^{*+}e^-\overline{\nu}$, $D^{*+} \to D^0\pi^+$, plus their charged conjugate decays.

The neural network uses the following discriminating variables as input:

- $|P_\pi|$: the momentum of the slow pion in the $\Upsilon(4S)$ rest frame;
- M^2_{miss}: the invariant mass squared computed from the B, D^* and e four-momenta through the relation $M^2_{\text{miss}} = (p_B - p_{D^*} - p_e)^2$. Neglecting resolution effects, this quantity must be zero, whereas background events are spread within a wide M^2_{miss} range.
- $cos\Theta^*$: the cosine of the angle between the D^* and the electron flight directions in the $\Upsilon(4S)$ rest frame. For B decays to a spin-1 particle such as $B \to D^*\ell\nu$ decays and due to the angular momentum conservation one must have $cos\Theta^* \sim -1$, whereas all other events result in an almost flat distribution from -1 to +1.

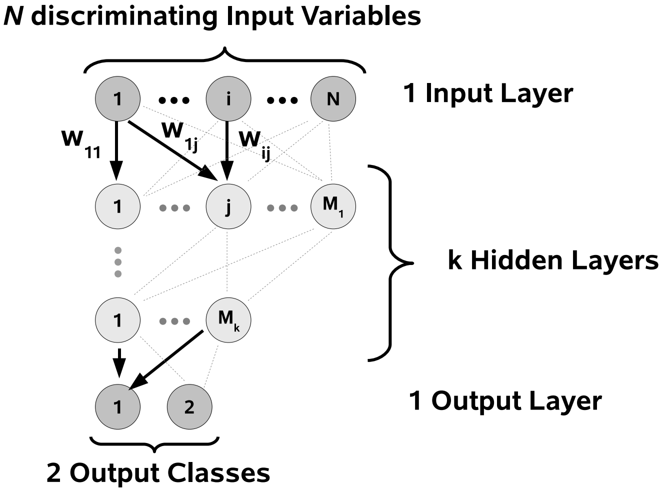

Figure 4.9: Propagation scheme of an Artificial Neural Network.

- $cos\Theta_{BY}$: the cosine of the angle between the B candidate and the vector sum of the D^* and electron candidates in the $\Upsilon(4S)$ restframe. The angle Θ_{BY} is defined in Figure 4.10. The four-momentum $p_Y = p_{D^*} + p_e$ has to be consistent with a B meson decay. The four-momentum of the neutrino in a $B \to D^* \ell \nu$ event can be expressed as

  $$p_\nu^2 = (p_B - p_Y) = M_B^2 + M_Y^2 - 2(E_B E_Y - |P_B||P_Y| cos\Theta_{BY}) = 0. \tag{4.15}$$

  The four-vector of the B meson, p_B, has an unknown direction. Nevertheless, equation (4.15) can be solved for $cos\Theta_{BY}$ because the energy and momentum of the B meson are known:

  $$cos\Theta_{BY} = \frac{2E_B E_Y - M_B^2 - M_Y^2}{2|P_B||P_Y|}. \tag{4.16}$$

  For each fully reconstructed decay one must have $|cos\Theta_{BY}| < 1$. The background will tend to have non-physical values of $|cos\Theta_{BY}|$. Extensions of $|cos\Theta_{BY}| > 1$ for partial reconstructed $B \to D^* \ell \nu$ events are due to detector resolution and the approximation made to reconstruct D^* candidates from slow pion kinematics.

Figures 4.11 and 4.12 show the distribution of input variables and Figure 4.13 their linear correlations for $D^* \to \pi^\pm$ and $D^* \to \pi^0$, respectively. The preselection cuts, $|cos\Theta_{BY}| < 5$ and $M_{\text{miss}}^2 > -7\,\text{GeV}^2$ restrict the region, for which the neural network has been built. These cuts do not affect the $B \to D^* \ell \nu$ efficiency ($\sim 100\%$ of truth $B \to D^* \ell \nu$ events are selected) but reduce the contribution of $B \to X_u l \nu$ events, so that the training of neural network is

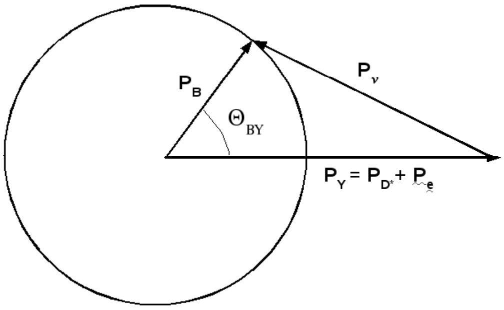

Figure 4.10: Angle Θ_{BY} defined in the $\Upsilon(4S)$ frame.

focussing only on the region where both classes are present and maximal separation power can be achieved.

Each training sample contains 12000 $B \to D^{*}\ell\nu$ and the same number of $B \to X_u l\nu$ Monte Carlo truth events. Neural networks have been built with $k = 2$ hidden layers. The number of training cycles has been chosen to be 500, which has been found to be reasonable. The normalized output distributions are shown in Figure 4.14. The $B \to D^{*}\ell\nu$ veto is then defined by the cut on the neural network output distribution.

In principle, for each analyzed event, one or more $B \to D^{*}\ell\nu$ candidates can be reconstructed. In such cases the candidates with maximal neural network outputs, $NN^{\pi^{\pm}}_{\mathrm{max}}$ and $NN^{\pi^{0}}_{\mathrm{max}}$, have been chosen. Finally, the optimization procedure (see Section 4.8) is used to evaluate the best cuts on the variables, $NN^{\pi^{\pm}}_{\mathrm{max}}$ and $NN^{\pi^{0}}_{\mathrm{max}}$.

4.7 Continuum Subtraction

A comparison of continuum Monte Carlo simulation, $e^{+}e^{-} \to f\bar{f}$ ($f \equiv$ fermion) to off-peak data shows discrepancies in the normalization and shape of some distributions, as shown in Figure 4.15. In particular, the luminosity of simulated Bhabha events can not be determined and hence it is difficult to normalize the simulated Bhabha sample to off-peak data. Therefore, instead of continuum Monte Carlo the off-peak data is used for continuum subtraction.

The data presented in this analysis is shown (see section 4.9) after subtracting from the on-peak sample the off-peak data scaled to on-peak luminosity with a scaling factor $F_{\mathrm{off}} = 9.94$ calculated as

$$F_{\mathrm{off}} = \frac{\mathcal{L}_{\mathrm{on}}}{\mathcal{L}_{\mathrm{off}}}\left(\frac{E_{\mathrm{off}}}{E_{\mathrm{on}}}\right)^{2}, \tag{4.17}$$

where $\mathcal{L}_{\mathrm{on}}$ and $\mathcal{L}_{\mathrm{off}}$ are the total on-peak and off-peak luminosities and E_{on} and E_{off} corresponding center of mass energies, respectively. The correction $E_{\mathrm{off}}/E_{\mathrm{on}}$ is needed to take into account different production cross-sections for $e^{+}e^{-} \to f\bar{f}$ processes at different center of mass energies.

In order to reduce the statistical uncertainties induced by subtracting the scaled off-peak data a part of refined selection criteria outlined in section 4.8 has been designed to suppress continuum events. Furthermore, these selection criteria improve the agreement between on-peak and scaled off-peak data. Figure 4.16 shows the lepton energy distribution of on-peak and off-peak data in the region $E_e > 2.8\,\mathrm{GeV}$. Above this threshold no B mesons can

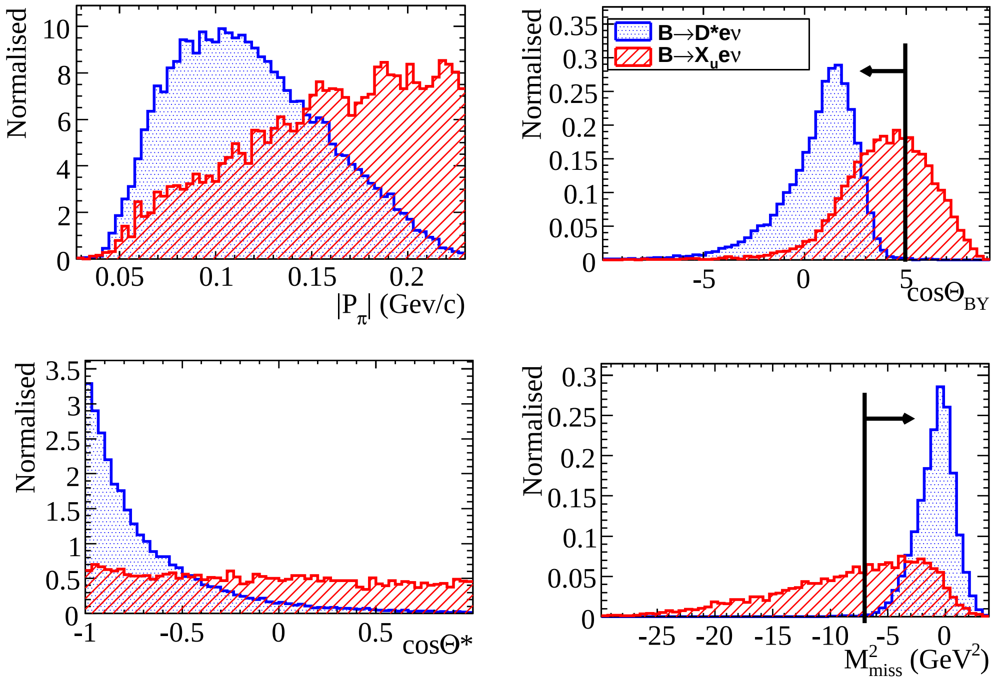

Figure 4.11: Distributions of the neural network input variables for $D^* \to \pi^\pm$ class. The vertical solid lines represent the preselection cuts applied to $B \to D^*\ell\nu$ events before NN training.

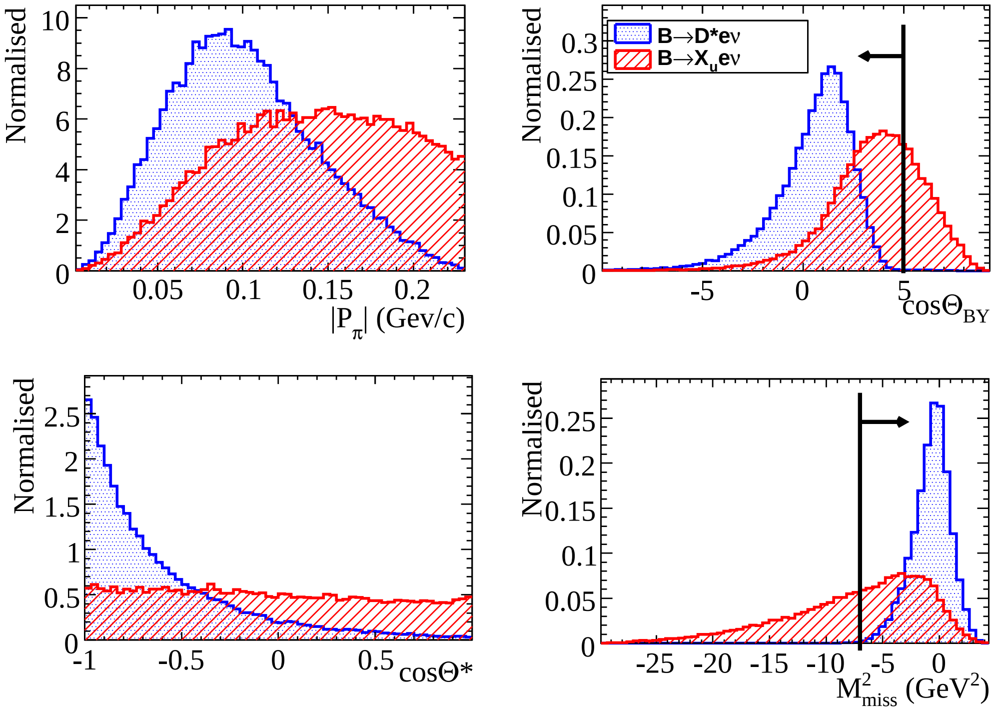

Figure 4.12: Distributions of the neural network input variables for $D^* \to \pi^0$ class. The vertical solid lines represent the preselection cuts applied to $B \to D^* \ell \nu$ events before NN training.

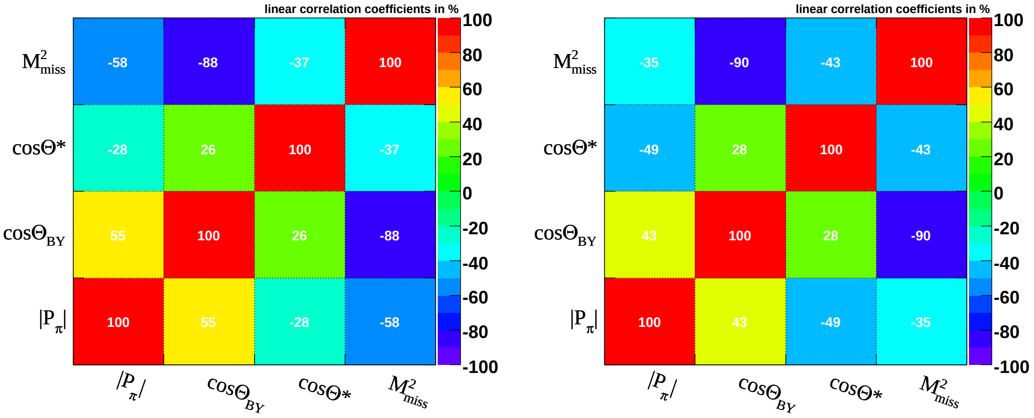

	$\lvert P_\pi \rvert$	$\cos\Theta_{BY}$	$\cos\Theta*$	M^2_{miss}
M^2_{miss}	-58	-88	-37	100
$\cos\Theta*$	-28	26	100	-37
$\cos\Theta_{BY}$	55	100	26	-88
$\lvert P_\pi \rvert$	100	55	-28	-58

	$\lvert P_\pi \rvert$	$\cos\Theta_{BY}$	$\cos\Theta*$	M^2_{miss}
M^2_{miss}	-35	-90	-43	100
$\cos\Theta*$	-49	28	100	-43
$\cos\Theta_{BY}$	43	100	28	-90
$\lvert P_\pi \rvert$	100	43	-49	-35

a) $D^* \to \pi^\pm$ class

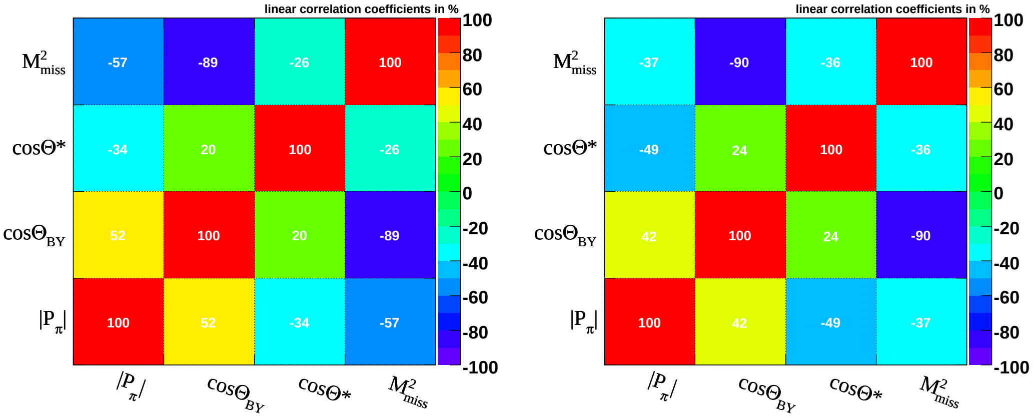

	$\lvert P_\pi \rvert$	$\cos\Theta_{BY}$	$\cos\Theta*$	M^2_{miss}
M^2_{miss}	-57	-89	-26	100
$\cos\Theta*$	-34	20	100	-26
$\cos\Theta_{BY}$	52	100	20	-89
$\lvert P_\pi \rvert$	100	52	-34	-57

	$\lvert P_\pi \rvert$	$\cos\Theta_{BY}$	$\cos\Theta*$	M^2_{miss}
M^2_{miss}	-37	-90	-36	100
$\cos\Theta*$	-49	24	100	-36
$\cos\Theta_{BY}$	42	100	24	-90
$\lvert P_\pi \rvert$	100	42	-49	-37

b) $D^* \to \pi^0$ class

Figure 4.13: Linear correlation coefficients of NN input variables from $B \to D^*\ell\nu$ (left) and $B \to X_u l\nu$ (right) samples.

be produced and the remaining events are pure continuum events. Hence, the continuum estimation using off-peak data can directly tested by comparison of lepton energy spectra in this region. The bottom plots in Figure 4.16 display the comparison between on-peak and off-peak data as $y_i = N_i^{\text{on}}/N_i^{\text{off}} - 1$, where N_i denotes the number of entries for a given bin i. These plots provide also χ^2 values calculated as

$$\chi^2 = \sum_i \frac{(N_i^{\text{off}} - N_i^{\text{on}})^2}{\sigma_i^2(\text{off}) + \sigma_i^2(\text{on})}, \tag{4.18}$$

based purely on statistical uncertainties. In addition, a fit to a constant value, $y = P_0$, is performed to provide a quantitative numbers for a deviation between data and the simulation.

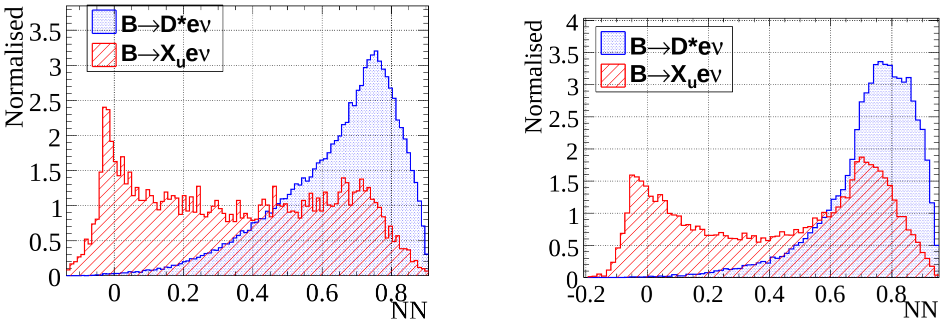

Figure 4.14: The normalized neural network output distributions for $D^* \to \pi^\pm$ (left) and $D^* \to \pi^0$ (right) classes. The plots show distributions obtained from Monte Carlo simulation after neural network training. The two output classes are $B \to D^* \ell \nu$ (blue) and $B \to X_u l \nu$ (red) events.

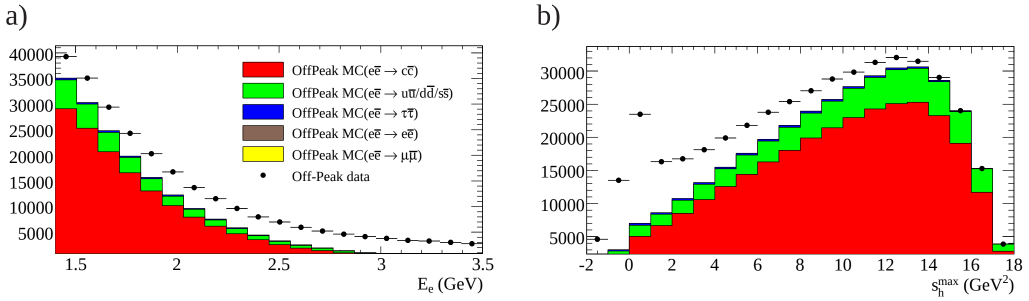

Figure 4.15: Off-peak data and off-peak MC distributions for a) E_e and b) s_h^{max}after applying the preselection requirements. The simulation is scaled to the luminosity of the off-peak data. There are discrepancies in the normalization (both plots) as well as in the shape of distributions (right plot).

The parameter P_0 is displayed in lower plots as “offset(fit)” and the corresponding value for χ^2/ndf(fit). Both the fit and the calculation of χ^2 have been performed for the entire region of the plotted variable.
A reasonable agreement between on-peak and off-peak data is achieved for an electron energy above 2.8 GeV.

4.8 Optimization Procedure

The ratio of signal to background for events satisfying the preselection requirements outlined in section 4.4.1 is $N_{\text{sig}}^{MC}/N_{\text{bkg}}^{MC} = 0.03$. Therefore, further selection criteria are applied to reduce the amount of background and to improve the quality of the neutrino momentum measurement. The optimal selection requirements are obtained from a cut optimization procedure described in this section. The variables used in this procedure are chosen with

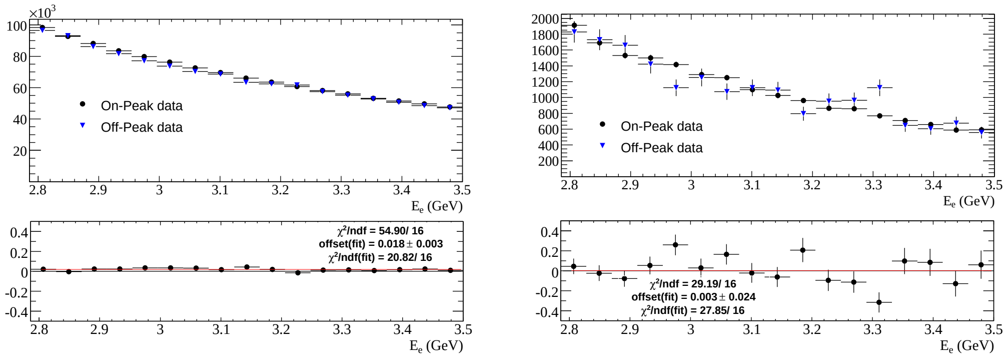

Figure 4.16: Lepton energy distribution for on-peak and scaled off-peak data in the region above 2.8 GeV, left: after preselection and right: after refined selection requirements are applied, as outlined in section 4.8.3. The lower plots show the relative comparison between on-peak and scaled off-peak data as $y_i = N_i^{\text{on}}/N_i^{\text{off}} - 1$. A quantitative comparison is given by χ^2 and the quantities from linear fit (“offset”(fit) and χ^2/ndf) performed to the data points y_i as described in details in section 4.9.

the aim to discriminate between $B \rightarrow X_u e \overline{\nu}_e$ and $B \rightarrow X_c l \nu$ events and to suppress the continuum events. The optimization of the selection criteria has been performed using only off-peak data for continuum events and $B\overline{B}$ Monte Carlo for signal and background estimations. The on-peak data are excluded to avoid introducing any possible bias in this analysis. Hence the event selection is performed “blind”.

4.8.1 Discriminating Variables

The discriminating variables entering in the optimization procedure are:

1. $E_{\text{miss}} - |P_{\text{miss}}|$, the difference between missing energy and missing momentum in the event. This quantity indicate the quality of the neutrino reconstruction. If the neutrino is the one particle in the event that is not reconstructed by the detection $E_{\text{miss}} - |P_{\text{miss}}|$ should be zero within detector resolution. Missing particles, such as K_L^0, additional neutrinos or particles lost due detector acceptance, cause a positive bias in $E_{\text{miss}} - |P_{\text{miss}}|$.
   As an alternative, the missing invariant mass squared
   $$m_{\text{miss}}^2 = (E_{\text{miss}} - |P_{\text{miss}}|)(E_{\text{miss}} + |P_{\text{miss}}|) \tag{4.19}$$
   could be used to improve the neutrino reconstruction. However, m_{miss}^2 mixes resolution effects with the decay kinematics of a specific event and is therefore less transparent. Hence, the quantity $E_{\text{miss}} - |P_{\text{miss}}|$ which is independent of the missing momentum and hence of the momentum of the real neutrino is used in this analysis;

2. $cos\Theta_{\text{miss}}$, the cosine of the missing three-momentum with respect to the beamline. If the direction of the missing three-momentum points toward the beamline

($|cos\Theta_{\mathrm{miss}}| \sim 1$) one can not distinguish between neutrinos and detectable particles that are outside the detector acceptance. In addition, the $cos\Theta_{\mathrm{miss}}$ distribution of continuum events peaks also at $|cos\Theta_{\mathrm{miss}}| \sim 1$ as shown in Figure 4.17. Therefore, this variable is used not only to improve the quality of the neutrino reconstruction but also to suppress the contribution from continuum events.

3. $cos\Theta_{\mathrm{e-T}}$, the cosine of the angle between thrust axis and the flight direction of the signal electron. The thrust is defined as

$$T = \frac{\sum_i |n \cdot P_i|}{\sum_i |P_i|}, \tag{4.20}$$

where P_i are the longitudinal momenta of the particle i (the signal electron is not included) and the vector n is the thrust axis pointing in the direction where the sum of longitudinal momenta P_i becomes maximal. The thrust is an event shape variable. The B mesons are produced nearly at rest. Their decay products are distributed roughly uniformly in solid angle. In contrast, continuum events have a much more collimated (jet-like) event topology. Figure 4.17 shows the $cos\Theta_{\mathrm{e-T}}$ distribution for on-peak and off-peak data. The continuum events peak at ±1;

4. $NN^{\pi^\pm}_{\mathrm{max}}$, $NN^{\pi^0}_{\mathrm{max}}$, output of the neural networks for $D^* \rightarrow \pi^\pm$ and $D^* \rightarrow \pi^0$ classes, respectively (see section 4.6.3). These variables are used to define the veto which is applied to remove $B \rightarrow D^* \ell \nu$ events.

5. E_e, the energy of the signal electron. Due to the kinematical limit of the electron energy the upper bound is set at 2.8 GeV;

6. $s_{\mathrm{h}}^{\mathrm{max}}$, the maximum invariant mass squared of the hadronic recoil system (see section 2.3). This variable is used to reduce the amount of $B \rightarrow X_c l \nu$ background.

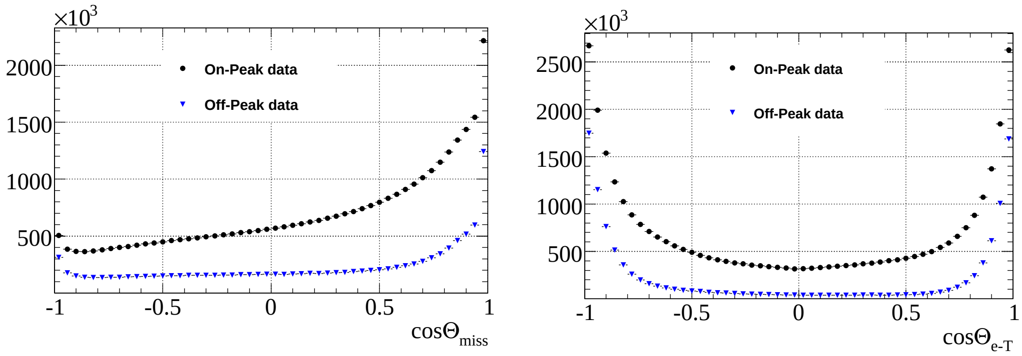

Figure 4.17: Distribution for $cos\Theta_{\mathrm{miss}}$ (left) and $cos\Theta_{\mathrm{e-T}}$ (right) for on-peak and scaled off-peak data after applying the preselection requirements. Both distributions peak at ±1.

4.8.2 Optimization Technique

The selection criteria were optimized by finding a set of values for the discriminating variables for which the overall uncertainty on the extracted signal yield was minimal. This corresponds to an optimization of the total branching fraction $\mathcal{B}(B \to X_u e\overline{\nu}_e)$. An alternative is the optimization of the uncertainty on the CKM matrix element $|V_{ub}|$ calculated from $\Delta\mathcal{B}(B \to X_u e\overline{\nu}_e)$ as discussed in section 8.3. This requires a calculation of the normalized theoretical rate, $\Delta\Gamma/|V_{ub}|^2$, and corresponding theoretical uncertainties for each cut value of the discriminating variables. Corresponding calculations will be soon provided [52] and the optimization procedure can be then modified.

The extracted signal yield, corrected for efficiency and acceptance, is

$$S = \frac{N_{\mathrm{tot}} - N_{B\bar{B}} - F_{\mathrm{off}} \cdot N_{\mathrm{off}}}{\varepsilon}, \tag{4.21}$$

where

- $N_{B\bar{B}}$ is the number of $B\bar{B}$ Monte Carlo events scaled to the number of $B\bar{B}$ pairs in data ($B \to X_u l\nu$ events not included);
- $F_{\mathrm{off}} \cdot N_{\mathrm{off}}$ is the off-peak data yield scaled to on-peak luminosity with a scaling factor $F_{\mathrm{off}} = 9.94$ (defined in section 4.7);
- N_{sig} is the number of $B \to X_u e\overline{\nu}_e$ signal events after the cuts;
- $\varepsilon = N_{\mathrm{sig}}/N_{\mathrm{sig}}^{\mathrm{gen}}$ is the efficiency times acceptance for $B \to X_u e\overline{\nu}_e$ signal events. N^{gen} is the number of generated signal events before any cuts are applied;
- $N_{\mathrm{tot}} = \varepsilon N_{\mathrm{sig}} + N_{B\bar{B}} + F_{\mathrm{off}} N_{\mathrm{off}}$ is the total measured yield after the cuts.

The overall uncertainty on the extracted signal yield is computed as the quadratic sum of statistical, systematic and theoretical uncertainties :

$$\frac{\Delta S^2}{S^2} = \left(\frac{\Delta S^2}{S^2}\right)_{\mathrm{stat}} + \left(\frac{\Delta S^2}{S^2}\right)_{\mathrm{syst}} + \left(\frac{\Delta S^2}{S^2}\right)_{\mathrm{theo}}. \tag{4.22}$$

1. The statistical uncertainty for background, continuum and total measured yields is calculated assuming Poissonian statistic. It is estimated to be:

$$\begin{aligned} \left(\frac{\Delta S^2}{S^2}\right)_{\mathrm{stat}} &= \frac{\sigma^2(N_{\mathrm{tot}} - N_{B\bar{B}} - F_{\mathrm{off}} \cdot N_{\mathrm{off}})}{(N_{\mathrm{tot}} - N_{B\bar{B}} - F_{\mathrm{off}} \cdot N_{\mathrm{off}})^2} \\ &= \frac{N_{\mathrm{tot}} + N_{B\bar{B}} + F_{\mathrm{off}}^2 \cdot N_{\mathrm{off}}}{(N_{\mathrm{tot}} - N_{B\bar{B}} - F_{\mathrm{off}} \cdot N_{\mathrm{off}})^2}. \end{aligned} \tag{4.23}$$

2. The systematic uncertainty due to the $B\bar{B}$ background can be only evaluated at the end of this analysis using on-peak data (see section 7.3). Therefore, in the optimization procedure an approximation for the systematic uncertainty is used:

$$\left(\frac{\Delta S^2}{S^2}\right)_{\mathrm{syst}} = \frac{(\rho \cdot N_{B\bar{B}})^2}{(N_{\mathrm{tot}} - N_{B\bar{B}} - F_{\mathrm{off}} \cdot N_{\mathrm{off}})^2}. \tag{4.24}$$

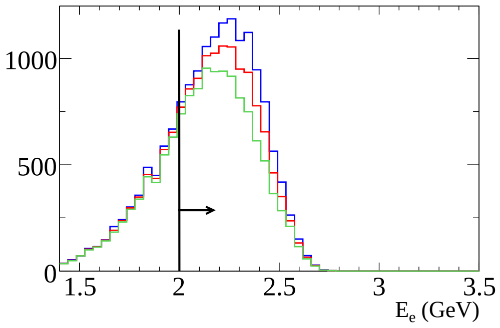

Figure 4.18: Distributions of electron energy for simulated $B \longrightarrow X_u e \overline{\nu}_e$ signal events for SF parameter pairs $(m_b, a) = (4.658\,\mathrm{GeV}, 1.328)$ (red), $(m_b, a) = (4.577\,\mathrm{GeV}, 1.973)$ (green) and $(m_b, a) = (4.739\,\mathrm{GeV}, 0.761)$ (blue). The numbers of extracted signal yields calculated as an Integral between lower bound (2.0 GeV) and upper bound (2.8 GeV) are used to compute the theoretical uncertainty on $\Delta(S)/S$.

The fixed parameter ρ is the fractional uncertainty in the $B\bar{B}$ background. One assumes that the systematic uncertainty can be scaled with the number, $N_{B\bar{B}}$, of $B\bar{B}$ background events. The fractional uncertainty on the signal yield due to ρ is then $\Delta S/S = \rho \cdot N_{B\bar{B}}/N_{\mathrm{sig}}$. In the optimization procedure the parameter ρ is chosen to be 0.04 ($N_{B\bar{B}}/N_{\mathrm{sig}} \sim 1.3$) which corresponds to a 5% uncertainty on $\Delta S/S$. In addition, the stability of cut values for the discriminating variables depending on ρ has been studied (see Figures 4.22 and 4.23). This study shown that the results of the optimization procedure for all discriminating variables (with the exception of $\mathrm{s}_{\mathrm{h}}^{\mathrm{max}}$and E_e) are less sensitive to the parameter ρ in the range between 0.03 and 0.05. This corresponds to 4% – 6% uncertainties, which is roughly what is found in chapter [4] 7.

3. The theoretical uncertainty is estimated by varying the two SF parameters m_b and a. A detailed description of the computation of the theoretical uncertainty is given in section 7.2. The changes on the SF parameters result in different numbers of extracted signal yields, N_{sig}, and hence in different values of the reconstruction efficiency ε. Figure 4.18 shows the E_e distribution for different values of the SF parameters for simulated $B \longrightarrow X_u e \overline{\nu}_e$ signal events. The corresponding uncertainty is then defined as

$$\left(\frac{\Delta S^2}{S^2}\right)_{\mathrm{theo}} = \frac{\delta^2(\varepsilon)}{\varepsilon}, \tag{4.25}$$

where the $\delta(\varepsilon)$ denotes the difference of the signal reconstruction efficiency with respect to the changes on the SF parameters.

The selection was optimized by adjusting each of the criteria and iterating the procedure until stable values were obtained.

---

[4] The systematic uncertainty due to $B\bar{B}$ background is evaluated for the partial branching fraction, which is equal in this case to the uncertainty on the total branching fraction.

Table 4.6: Residual yields for B^+ decays after applying successively the selection requirements. The events in the simulation are scaled to the number of $B\bar{B}$ pairs in data using the scaling factor $F_{B\bar{B}} = 0.323$. The requirements on E_e and $s_{\mathrm{h}}^{\mathrm{max}}$ define the signal region.

Criteria	$B \to X_u e \overline{\nu}_e$	$B \to D^* e \nu_e$	$B \to D e \nu_e$	$B \to X_c^{\mathrm{rest}} e \overline{\nu}_e$	other
Preselection	441427 ± 378	10358043 ± 1830	2828376 ± 956	2156727 ± 835	505360 ± 404
Bhabha veto	419573 ± 368	9932548 ± 1792	2722304 ± 938	2088560 ± 822	482955 ± 395
N_{lep}	342112 ± 333	7905366 ± 1598	2159713 ± 835	1626787 ± 725	319553 ± 321
$cos\Theta_{\mathrm{miss}}$	223146 ± 269	5043806 ± 1277	1342772 ± 659	948849 ± 554	171136 ± 235
$cos\Theta_{\mathrm{e-T}}$	95066 ± 175	2215314 ± 846	529501 ± 414	386141 ± 353	57487 ± 136
$E_{\mathrm{miss}} - \lvert P_{\mathrm{miss}} \rvert$	17697 ± 76	293655 ± 308	69623 ± 150	49336 ± 126	7357 ± 49
$B \to D^* e \nu_e$ veto	8502 ± 52	65273 ± 145	26283 ± 92	11949 ± 62	2245 ± 27
E_e	4021 ± 36	11816 ± 62	3471 ± 33	420 ± 12	259 ± 9
$s_{\mathrm{h}}^{\mathrm{max}}$	3182 ± 32	3205 ± 32	780 ± 16	68 ± 5	79 ± 5

4.8.3 Optimization Results

Figures 4.19 to 4.21 display the relative uncertainty $\Delta S/S$ as a function of the selection criteria studied. The contributions from the theoretical, $B\bar{B}$ background systematic and statistical uncertainties are shown individually. For each plot, all selection criteria are held fixed except for the variable under study.
The refined selection criteria obtained by the optimization procedure are

- $-0.80 < cos\Theta_{\mathrm{miss}} < 0.64$;
- $-0.56 < cos\Theta_{\mathrm{e-T}} < 0.64$;
- $0.0\,\mathrm{GeV} < E_{\mathrm{miss}} - |P_{\mathrm{miss}}| < 0.8\,\mathrm{GeV}$;
- $NN_{\mathrm{max}}^{\pi^\pm} < 0.208$;
- $NN_{\mathrm{max}}^{\pi^0} < 0.136$;
- $E_e < 2.0\,\mathrm{GeV}$;
- $s_{\mathrm{h}}^{\mathrm{max}} < 3.52\,\mathrm{GeV}^2$.

In addition, the number of charged leptons in the event has to be $N_{\mathrm{lep}} = 1$. This requirement helps improving the neutrino resolution by reducing the number of events for which more than one neutrino is produced.

Tables 4.6 to 4.9 show the impact of the selection and resulting yields after applying successively the selection criteria to the simulation for charged and neutral B decays, respectively. The ratio of signal to $B\bar{B}$ background for events satisfying the refined selection criteria is $N_{sig}^{MC}/N_{bkg}^{MC} \approx 0.80$. This ratio is about 10% higher compared to results from a similar analysis performed in [1]. Furthermore, the obtained optimization result for the lower bound requirement of the electron energy is $2.0\,\mathrm{GeV}$ compared to $2.1\,\mathrm{GeV}$ chosen in [1]. In general, the amount of $B\bar{B}$ background is strongly correlated with the lower bound of electron energy and the upper bound of $s_{\mathrm{h}}^{\mathrm{max}}$. As the lower cut (upper cut) for E_e

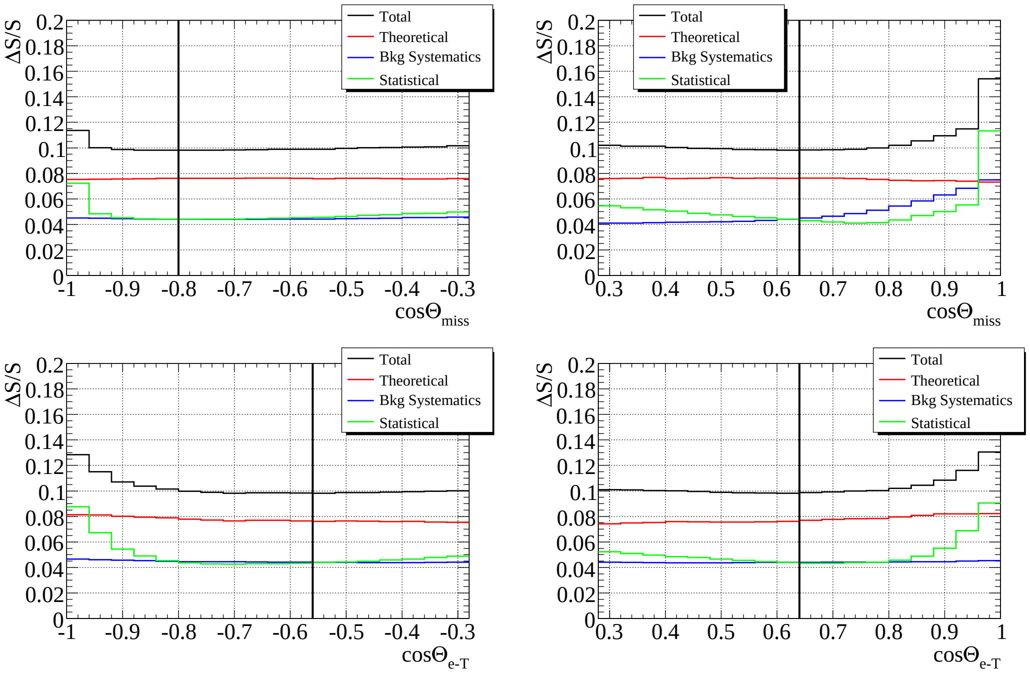

Figure 4.19: Optimization of the event selection using $cos\Theta_{\rm miss}$ (top) and $cos\Theta_{\rm e-T}$ (bottom) variables. The vertical lines denote the lower (left) and upper (right) bounds chosen for the selection criteria. The plots display the total (black) fractional uncertainty $\Delta S/S$ due to statistical (green), background systematic (blue) and theoretical (red) uncertainties. Note that all selection criteria are held fixed except for the variable under study.

($s_{\rm h}^{\rm max}$) decreases (increases) the amount of $B\bar{B}$ increases strongly. The achieved improvement in this analysis is a result of the $B \to D^{*}e\nu_{e}$ veto.
After applying of $B \to D^{*}e\nu_{e}$ veto about 80% of $B \to D^{*}e\nu_{e}$ decays are removed while $\sim$ 50% of signal events are lost, as shown in Tables 4.7 and 4.9. The contribution from $B \to D\ell\nu$, $B \to X_{c}^{\rm rest}e\bar{\nu}_{e}$ and other backgrounds is also reduced by 60% – 75%. Thus, about 7500 background events are expected to be selected from $B\bar{B}$ data. The difference in yields between $B^{0}\bar{B}^{0}$ and $B^{+}B^{-}$ at the preselection level is due to the difference in semileptonic branching fractions (see Tables 4.3 and 4.5). The selection requirements (e. g. cut on $N_{\rm lep}$ or $E_{\rm miss} - |P_{\rm miss}|$) amplify this assymetry, since the efficiency for $B^{0}\bar{B}^{0}$ events is 8% smaller than for $B^{+}B^{-}$ events. This is caused by the higher $D^{\pm}$ content in $B^{0}/\bar{B}^{0}$ decays. In fact, $D^{\pm}$ decay more often than $D^{0}/\bar{D}^{0}$ to neutrinos K_{L}^{0} (see table 7.4). Therefore, such events are more likely to fail the neutrino reconstruction requirements.

4.9 Comparison Between Data and Simulation

In this analysis the Monte Carlo simulation is used to estimate the $B\bar{B}$ background and the signal efficiency. Therefore, it is important to validate the simulation by comparing kine-

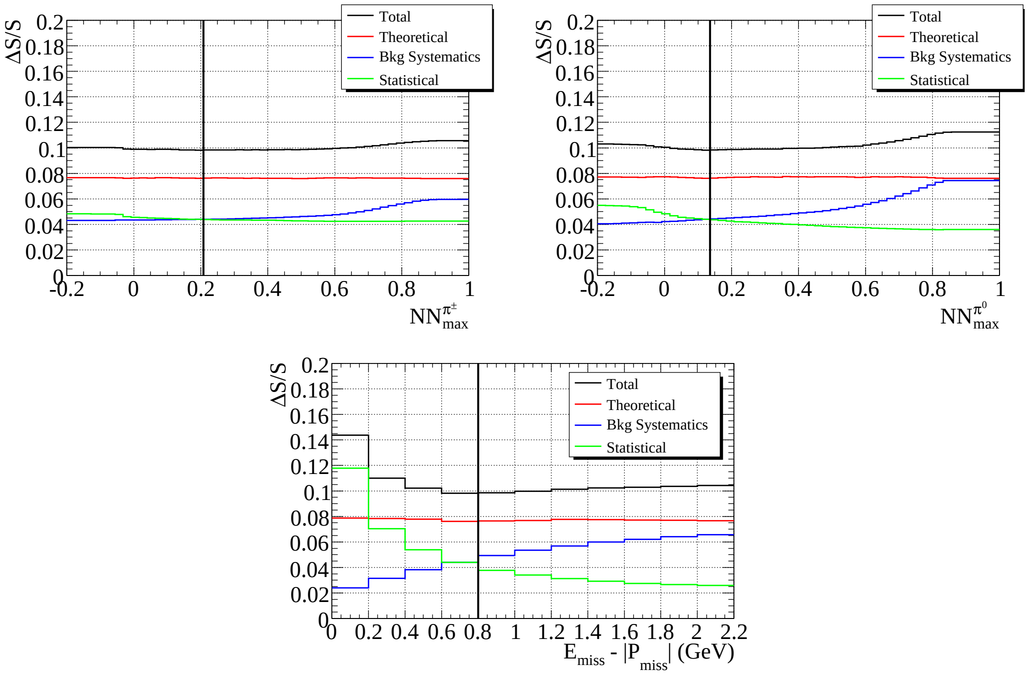

Figure 4.20: Optimization of the event selection using neural net outputs for $D^* \rightarrow \pi^\pm$ (top left) and $D^* \rightarrow \pi^0$ (top right) classes and $E_{\mathrm{miss}} - |P_{\mathrm{miss}}|$ (bottom) variable. The vertical lines denote the upper bounds chosen for the selection criteria. The plots display the total (black) fractional uncertainty $\Delta S/S$ due to statistical (green), background systematic (blue) and theoretical (red) uncertainties. Note that all selection criteria are held fixed except for the variable under study.

matical distributions between data and the Monte Carlo simulation.

Figures 4.24 to 4.34 present spectra for various quantities satisfying the preselection and refined event selection requirements listed in the previous section. For distributions obtained after the refined selections all refined cuts have been applied except for the plotted variable, in which case the selection region is denoted by a vertical line and an arrow. The comparison plots are produced including only statistical uncertainties and hence are mostly for a qualitative crosscheck. Note that in these Figures and all similar Figures, the top plot compares the data after continuum subtraction (data points) and the contribution from signal and background Monte Carlo simulation (solid lines), and the bottom plot displays the comparison between data and $B\bar{B}$ simulation (signal + background) as $y_i = N_i^{\mathrm{data}}/N_i^{\mathrm{MC}} - 1$, where N_i denotes the number of entries for a given bin i. Lower plot provides also χ^2 value calculated as

$$\chi^2 = \sum_i \frac{(N_i^{\mathrm{MC}} - N_i^{\mathrm{data}})^2}{\sigma_i^2(\mathrm{MC}) + \sigma_i^2(\mathrm{data})}, \tag{4.26}$$

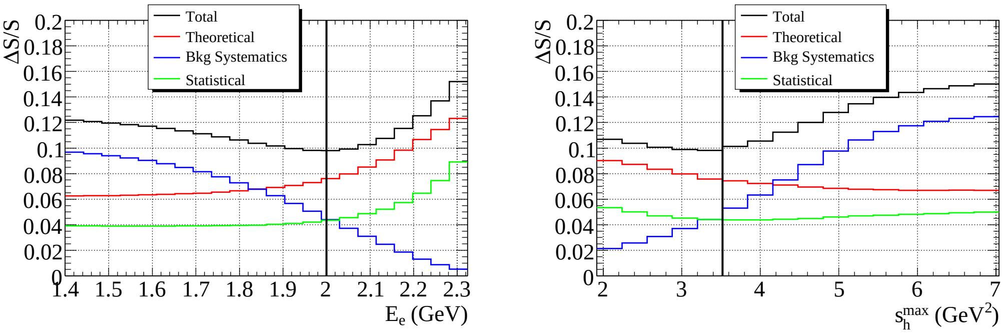

Figure 4.21: Optimization of the event selection using lepton energy (left) and $s_\mathrm{h}^\mathrm{max}$(right) variable. The vertical lines denote the requirement chosen for the selection criteria. The plots display the total (black) fractional uncertainty $\Delta S/S$ due to statistical (green), background systematic (blue) and theoretical (red) uncertainties. Note that all selection criteria are held fixed except for the variable under study.

based purely on statistical uncertainties. In order to enter the χ^2 computation, a bin i has to satisfy $y_i^{\mathrm{data/MC}} - 3\sigma_i(\mathrm{data/MC}) > 0$. In addition, a fit to a constant value $y = P_0$ is performed to provide a quantitative numbers for a deviation between data and the simulation. The parameter P_0 is displayed in the lower plot as “offset(fit)” and the corresponding value for $\chi^2/\mathrm{ndf(fit)}$. Both the fit and the calculation of χ^2 have been performed for entire region of the plotted variable.

The refined selection results in an improvement of the χ^2 probability for most of the variables, in particular for all variables used in the optimization procedure (e. g. $s_\mathrm{h}^\mathrm{max}$, E_e, $cos\Theta_\mathrm{miss}$ etc.). The χ^2 probability is calculated as

$$P_{\chi^2,\mathrm{ndf}} = \left[2^{\mathrm{ndf}/2}\Gamma\left(\frac{\mathrm{ndf}}{2}\right)\right]^{-1} \int_{\chi^2}^{\infty} t^{\frac{\mathrm{ndf}}{2}-1} e^{-\frac{t}{2}}\, dt, \tag{4.27}$$

where Γ is the generalization of the factorial function to real and complex arguments:

$$\Gamma_x = \int_0^\infty t^{x-1} e^{-t}\, dt. \tag{4.28}$$

The variables $cos\Theta_\mathrm{miss}$ and $cos\Theta_\mathrm{e-T}$ used in suppressing continuum events show a reasonable agreement within the entire region, and yield χ^2 probabilities of 78% and 32%, respectively. A good agreement between the data and Monte Carlo simulation is achieved also for the neutrino reconstruction in terms of missing energy and momentum, and $E_\mathrm{miss} - |P_\mathrm{miss}|$, as presented in Figures 4.24, 4.26 and 4.27. The requirement on the $E_\mathrm{miss} - |P_\mathrm{miss}|$ results in the χ^2 probabilities for P_miss and E_miss of 27% and 70%, respectively.

The agreement between data and the simulation for the neural network output is significantly improved after applying the refined selection, as shown in Figures 4.30 and 4.31. The corresponding χ^2 probabilities are $P_{\chi^2,\mathrm{ndf}} = 41\%$ for the $D^* \to \pi^\pm$ and $P_{\chi^2,\mathrm{ndf}} = 39\%$ for $D^* \to \pi^0$ classes.

Overall, a reasonable agreement is achieved between data and simulation for all variable

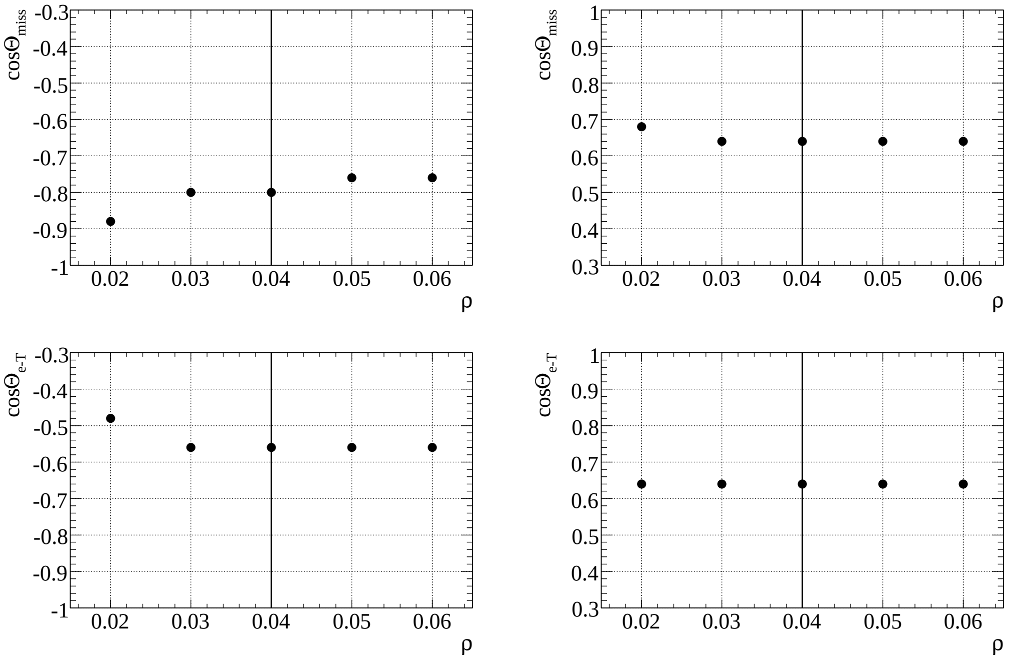

Figure 4.22: Refined selection requirement for $cos\Theta_{\mathrm{miss}}$ (top) and $cos\Theta_{\mathrm{e-T}}$ (bottom) obtained as a function of parameter ρ (see text). The left plots represent the requirements for the lower bounds and the right plots for the upper bounds. The vertical line denotes the value of ρ using to define default refined selection requirements as outlined in section 4.8.3.

plotted, particular for all variables used by the optimization procedure.
Figures 4.33 and 4.34 display electron energy spectrum and $\mathrm{s}_{\mathrm{h}}^{\mathrm{max}}$distributions, respectively. The latter is used for the signal extraction, as described in detail in chapter 6.1. The agreement between the data and the simulation for the $\mathrm{s}_{\mathrm{h}}^{\mathrm{max}}$distribution is very good, however there is small offset ("offset(fit)"$= -0.012 \pm 0.010$) in the comparison. The possible sources of this offset are the difference in branching fraction of B and D decays in the simulation and in the data, theoretical uncertainties in the signal simulation, or also the uncertainty in the number of $B\bar{B}$ events used to calculate the luminosity scaling factor $F_{B\bar{B}}$, as outlined in section 4.3. The influence of all systematic uncertainties is discussed in chapter 7.

Tables 4.10 and 4.11 summarize the yields and marginal efficiencies for data prior to and after continuum subtraction, and compare these results with expected yields from the Monte Carlo simulation. For each selection criteria, comparable yields and marginal efficiencies are obtained for $B\bar{B}$ data and the Monte Carlo simulation.

Table 4.7: Marginal efficiency for B^+ decays after applying successively the selection requirements. The efficiencies for a given requirement are calculated with respect to the yields obtained after the previous selection requirement.

Criteria	$B \to X_u e\overline{\nu}_e$	$B \to D^* e\nu_e$	$B \to De\nu_e$	$B \to X_c^{\text{rest}} e\overline{\nu}_e$	other
Preselection	1.000 ± 0.000	1.000 ± 0.000	1.000 ± 0.000	1.000 ± 0.000	1.000 ± 0.000
Bhabha veto	0.950 ± 0.000	0.959 ± 0.000	0.962 ± 0.000	0.968 ± 0.000	0.956 ± 0.000
N_{lep}	0.815 ± 0.000	0.796 ± 0.000	0.793 ± 0.000	0.779 ± 0.000	0.662 ± 0.000
$cos\Theta_{\text{miss}}$	0.652 ± 0.000	0.638 ± 0.000	0.622 ± 0.000	0.583 ± 0.000	0.536 ± 0.001
$cos\Theta_{\text{e}-\text{T}}$	0.426 ± 0.001	0.439 ± 0.000	0.394 ± 0.000	0.407 ± 0.000	0.336 ± 0.001
$E_{\text{miss}} - \lvert P_{\text{miss}} \rvert$	0.186 ± 0.001	0.133 ± 0.000	0.131 ± 0.000	0.128 ± 0.000	0.128 ± 0.001
$B \to D^* e\nu_e$ veto	0.480 ± 0.002	0.222 ± 0.000	0.378 ± 0.001	0.242 ± 0.001	0.305 ± 0.003
E_e	0.473 ± 0.003	0.181 ± 0.001	0.132 ± 0.001	0.035 ± 0.001	0.115 ± 0.004
$s_{\text{h}}^{\text{max}}$	0.791 ± 0.004	0.271 ± 0.002	0.225 ± 0.004	0.163 ± 0.010	0.304 ± 0.016

Table 4.8: Residual yields for B^0 decays after applying successively the selection requirements. The events in the simulation are scaled to the number of $B\overline{B}$ pairs in data using scaling factor $F_{B\overline{B}} = 0.323$. The requirements on E_e and $s_{\text{h}}^{\text{max}}$define the signal region.

Criteria	$B \to X_u e\overline{\nu}_e$	$B \to D^* e\nu_e$	$B \to De\nu_e$	$B \to X_c^{\text{rest}} e\overline{\nu}_e$	other
Preselection	417560 ± 367	8991054 ± 1705	2791888 ± 950	2422278 ± 885	659877 ± 462
Bhabha veto	396353 ± 358	8600945 ± 1667	2679234 ± 931	2343390 ± 870	628346 ± 451
N_{lep}	318997 ± 321	6649664 ± 1466	1985507 ± 801	1821417 ± 767	418906 ± 368
$cos\Theta_{\text{miss}}$	208884 ± 260	4274176 ± 1175	1252818 ± 636	1066328 ± 587	231749 ± 274
$cos\Theta_{\text{e}-\text{T}}$	88879 ± 169	1879731 ± 779	508963 ± 406	428882 ± 372	72732 ± 153
$E_{\text{miss}} - \lvert P_{\text{miss}} \rvert$	15130 ± 70	205188 ± 258	51321 ± 129	50562 ± 128	7443 ± 49
$B \to D^* e\nu_e$ veto	7372 ± 49	49648 ± 127	20552 ± 82	12233 ± 63	2192 ± 27
E_e	3480 ± 34	7899 ± 51	2805 ± 30	456 ± 12	229 ± 9
$s_{\text{h}}^{\text{max}}$	2778 ± 30	2436 ± 28	822 ± 16	66 ± 5	78 ± 5

Table 4.9: Marginal efficiency for B^0 decays after applying successively the selection requirements. The efficiencies for a given requirement are calculated with respect to the yields obtained after the previous selection requirement.

Criteria	$B \to X_u e\overline{\nu}_e$	$B \to D^* e\nu_e$	$B \to De\nu_e$	$B \to X_c^{\text{rest}} e\overline{\nu}_e$	other
Preselection	1.000 ± 0.000	1.000 ± 0.000	1.000 ± 0.000	1.000 ± 0.000	1.000 ± 0.000
Bhabha veto	0.949 ± 0.000	0.957 ± 0.000	0.960 ± 0.000	0.967 ± 0.000	0.952 ± 0.000
N_{lep}	0.805 ± 0.000	0.773 ± 0.000	0.741 ± 0.000	0.777 ± 0.000	0.667 ± 0.000
$cos\Theta_{\text{miss}}$	0.655 ± 0.000	0.643 ± 0.000	0.631 ± 0.000	0.585 ± 0.000	0.553 ± 0.000
$cos\Theta_{\text{e}-\text{T}}$	0.425 ± 0.001	0.440 ± 0.000	0.406 ± 0.000	0.402 ± 0.000	0.314 ± 0.001
$E_{\text{miss}} - \lvert P_{\text{miss}} \rvert$	0.170 ± 0.001	0.109 ± 0.000	0.101 ± 0.000	0.118 ± 0.000	0.102 ± 0.001
$B \to D^* e\nu_e$ veto	0.487 ± 0.002	0.242 ± 0.001	0.400 ± 0.001	0.242 ± 0.001	0.294 ± 0.003
E_e	0.472 ± 0.003	0.159 ± 0.001	0.136 ± 0.001	0.037 ± 0.001	0.104 ± 0.004
$s_{\text{h}}^{\text{max}}$	0.798 ± 0.004	0.308 ± 0.003	0.293 ± 0.005	0.144 ± 0.009	0.343 ± 0.018

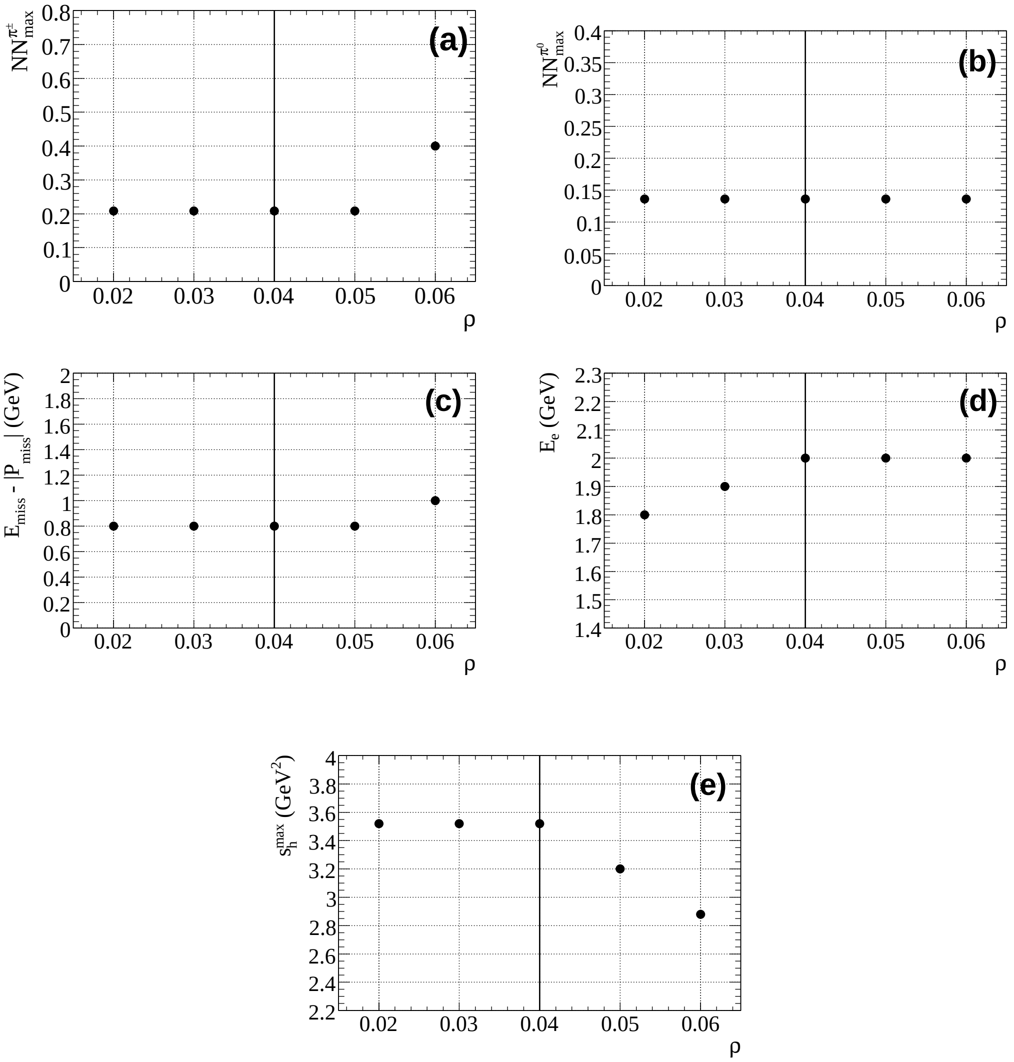

Figure 4.23: Refined selection requirements for neural network output ((a) $D^* \rightarrow \pi^{\pm}$, (b) $D^* \rightarrow \pi^0$), (c) $E_{\mathrm{miss}} - |P_{\mathrm{miss}}|$, (d) E_e and (e) $s_{\mathrm{h}}^{\mathrm{max}}$obtained as a function of parameter ρ (see text). The vertical line denotes the value of ρ using to define default refined selection requirements as outlines in section 4.8.3.

Table 4.10: Residual yields for data and Monte Carlo simulation after applying successively the selection requirements. The errors are purely statistical.

Criteria	On-peak data	Off-peak data	$B\bar{B}$ data	$B\bar{B}$ MC
Preselection	57846280 ± 7606	26406902 ± 16204	31439378 ± 17900	31572588 ± 3194
Bhabha veto	42622048 ± 6529	12619245 ± 11202	30002802 ± 12965	30294208 ± 3129
N_{lep}	34417476 ± 5867	11163041 ± 10536	23254436 ± 12059	23548022 ± 2759
$cos\Theta_{\mathrm{miss}}$	20660484 ± 4545	6024378 ± 7740	14636107 ± 8976	14763662 ± 2184
$cos\Theta_{\mathrm{e-T}}$	6604301 ± 2570	321598 ± 1788	6282703 ± 3131	6262696 ± 1423
$E_{\mathrm{miss}} - \lvert P_{\mathrm{miss}} \rvert$	800571 ± 895	43214 ± 656	757357 ± 1109	767311 ± 498
$B \to D^{*} e \nu_e$ veto	224129 ± 473	22532 ± 473	201597 ± 669	206249 ± 258
E_e	42753 ± 207	8452 ± 290	34301 ± 356	34857 ± 106
$s_{\mathrm{h}}^{\mathrm{max}}$	17534 ± 132	4385 ± 209	13149 ± 247	13494 ± 66

Table 4.11: Marginal efficiencies for data and Monte Carlo simulation after applying successively the selection requirements. The errors are purely statistical.

Criteria	On-peak data	Off-peak data	$B\bar{B}$ data	$B\bar{B}$ MC
Preselection	1.000 ± 0.000	1.000 ± 0.000	1.000 ± 0.000	1.000 ± 0.000
Bhabha veto	0.737 ± 0.000	0.478 ± 0.000	0.954 ± 0.000	0.960 ± 0.000
N_{lep}	0.808 ± 0.000	0.885 ± 0.000	0.775 ± 0.000	0.777 ± 0.000
$cos\Theta_{\mathrm{miss}}$	0.600 ± 0.000	0.540 ± 0.000	0.629 ± 0.000	0.627 ± 0.000
$cos\Theta_{\mathrm{e-T}}$	0.320 ± 0.000	0.053 ± 0.000	0.429 ± 0.000	0.424 ± 0.000
$E_{\mathrm{miss}} - \lvert P_{\mathrm{miss}} \rvert$	0.121 ± 0.000	0.134 ± 0.002	0.121 ± 0.000	0.123 ± 0.000
$B \to D^{*} e \nu_e$ veto	0.280 ± 0.001	0.521 ± 0.008	0.266 ± 0.001	0.269 ± 0.000
E_e	0.191 ± 0.001	0.375 ± 0.010	0.170 ± 0.001	0.169 ± 0.000
$s_{\mathrm{h}}^{\mathrm{max}}$	0.410 ± 0.002	0.519 ± 0.017	0.383 ± 0.003	0.387 ± 0.001

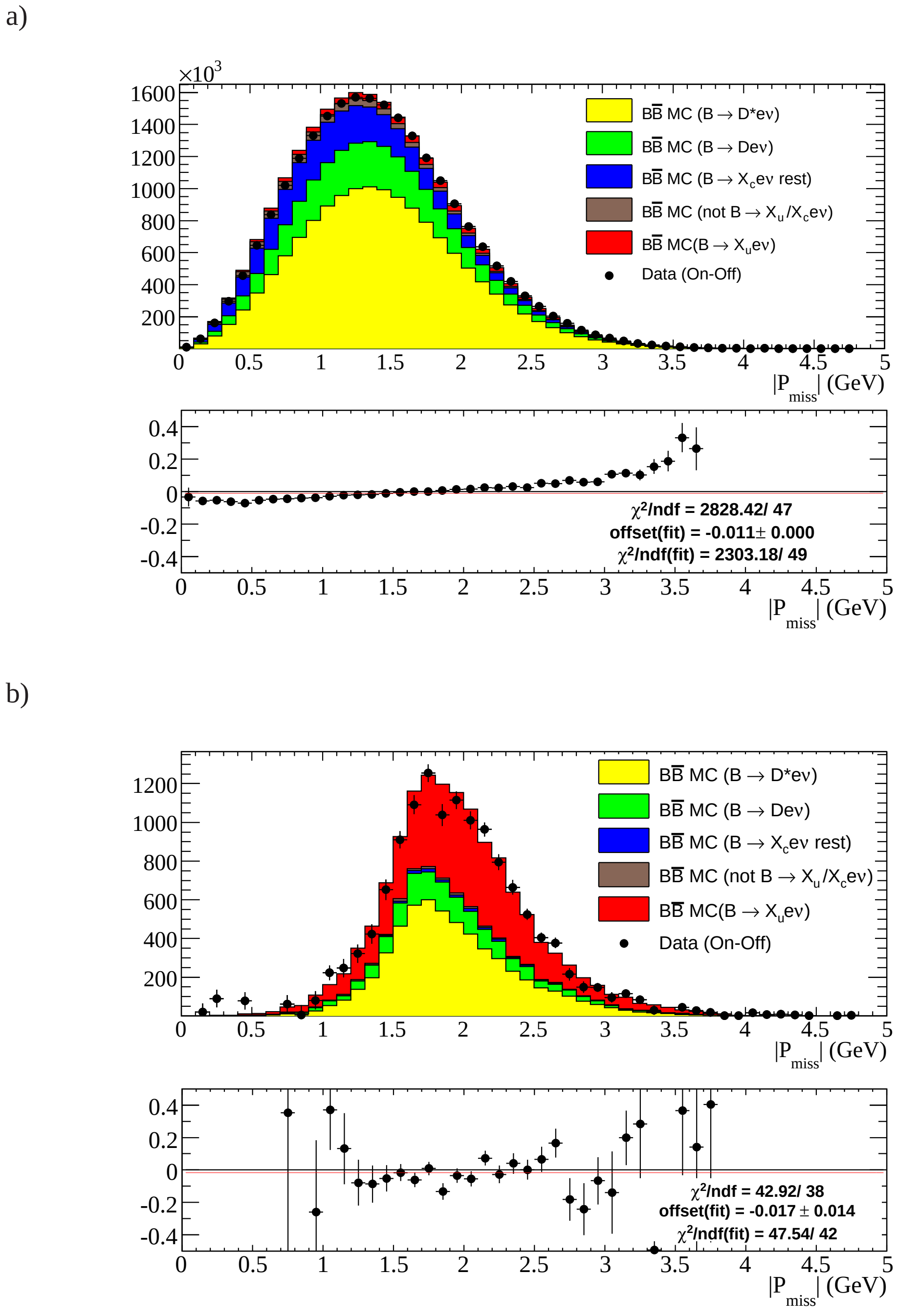

Figure 4.24: Data and MC distributions for $|P_{\text{miss}}|$ after applying a) the preselection and b) the refined selection requirements. The upper plot shows the data distribution after off-peak continuum subtraction as well as the Monte Carlo distribution. The lower plot shows the relative comparison between data and MC as $y_i = N_i^{\text{on}}/N_i^{\text{off}} - 1$. The simulation is scaled to the number of $B\bar{B}$ pairs in data. A quantitative comparison is given by χ^2 and the quantities from a fit to a constant value ("offset"(fit) and χ^2/ndf) performed to the data points y_i as described in details in section 4.9.

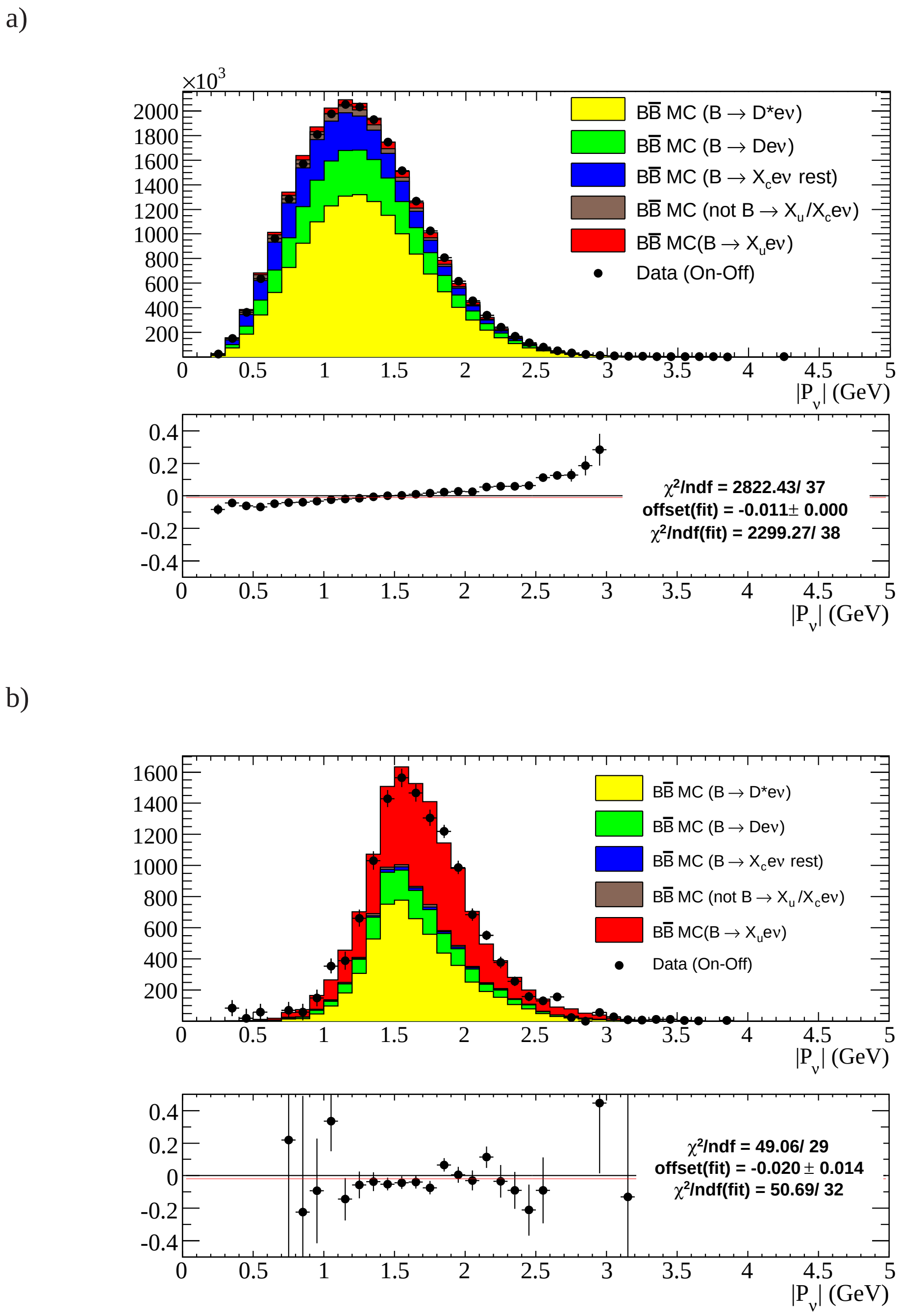

Figure 4.25: Data and MC distributions for $|P_\nu|$ after applying a) the preselection and b) the refined selection requirements. The plots follow the same conventions as those of figure 4.24.

a)

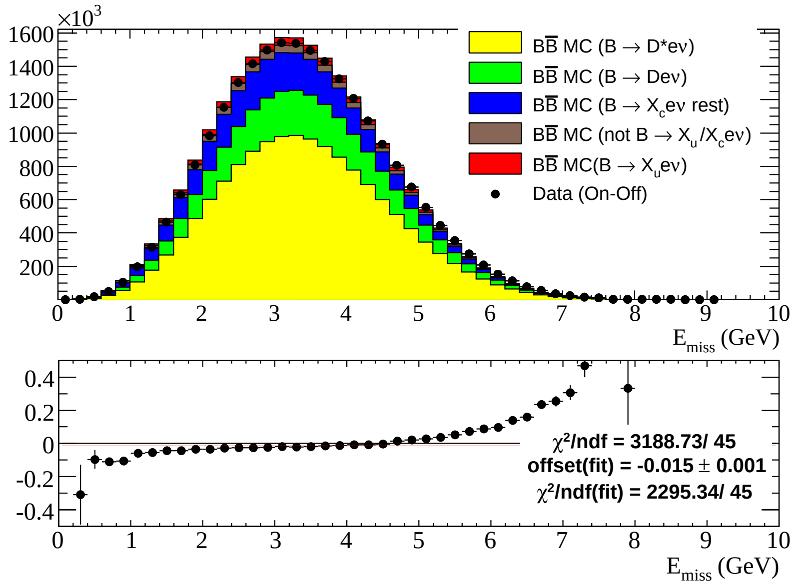

b)

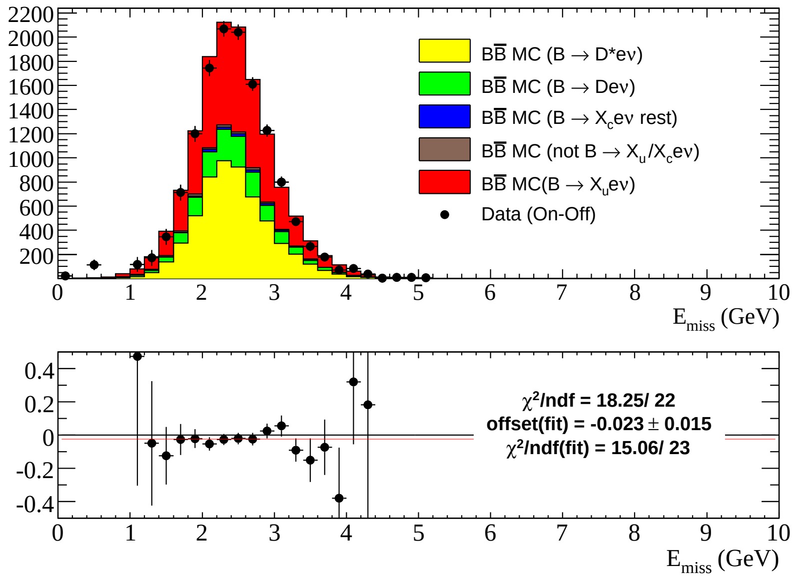

Figure 4.26: Data and MC distributions for E_{miss} after applying a) the preselection and b) the refined selection requirements. The plots follow the same conventions as those of figure 4.24.

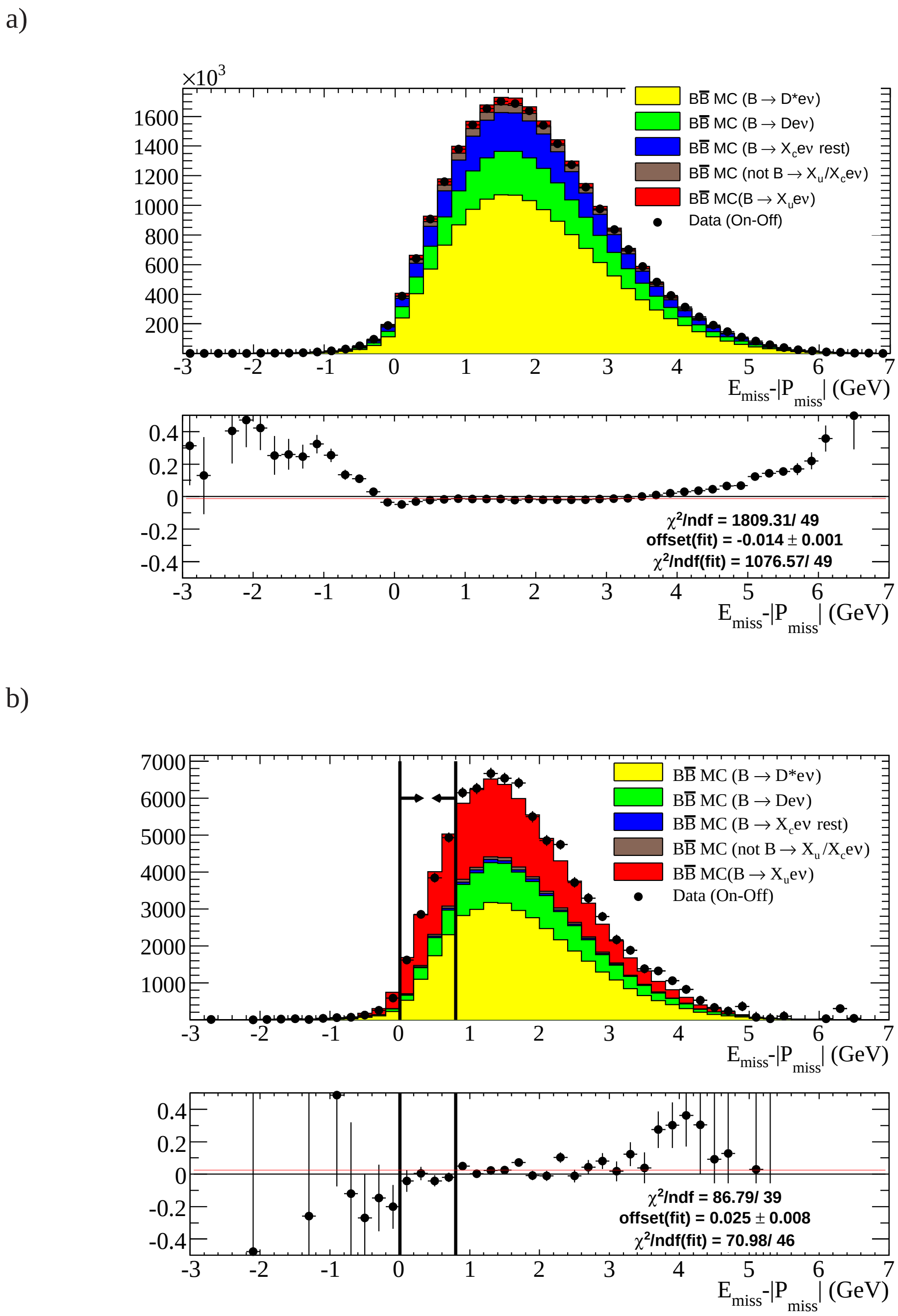

Figure 4.27: Data and MC distributions for $E_{\mathrm{miss}} - |P_{\mathrm{miss}}|$ after applying a) the preselection and b) the refined selection requirements. The plots follow the same conventions as those of figure 4.24.

a)

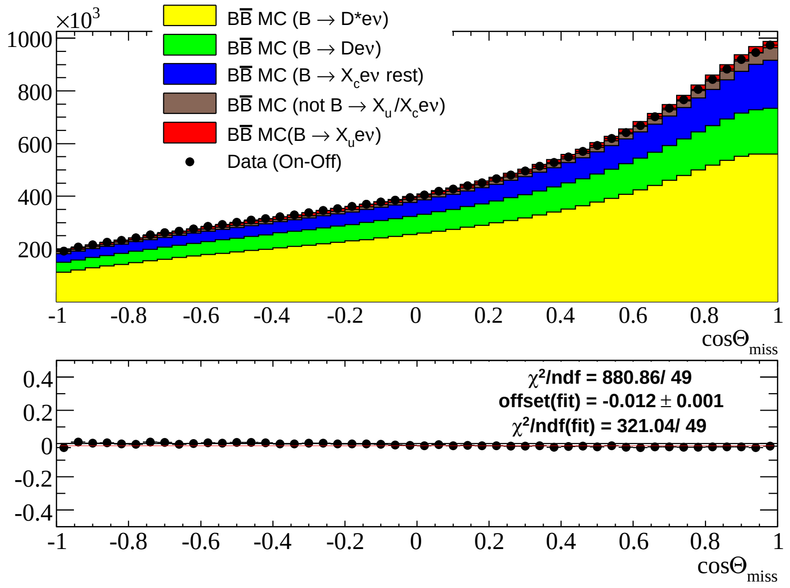

b)

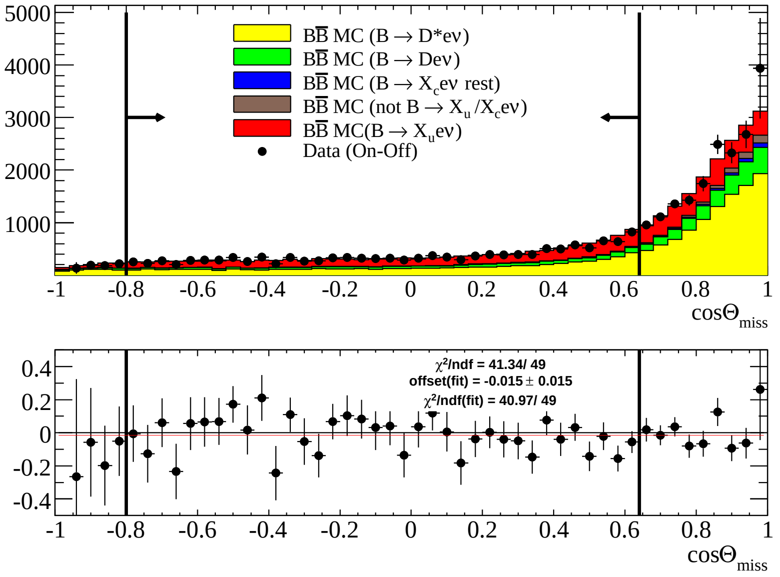

Figure 4.28: Data and MC distributions for $cos\Theta_{\text{miss}}$ after applying a) the preselection and b) the refined selection requirements. The plots follow the same conventions as those of figure 4.24.

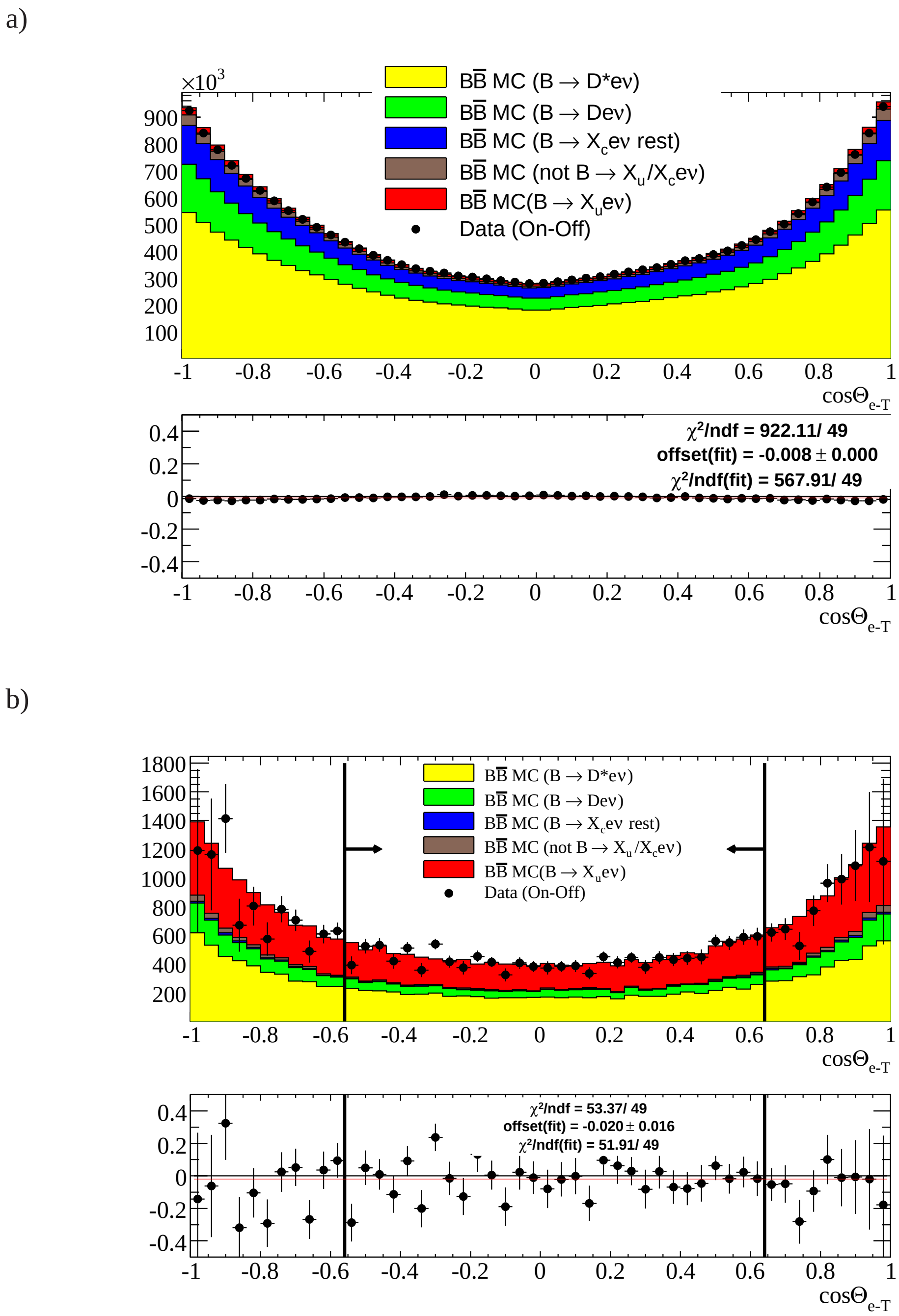

Figure 4.29: Data and MC distributions for $cos\Theta_{e-T}$ after applying a) the preselection and b) the refined selection requirements. The plots follow the same conventions as those of figure 4.24.

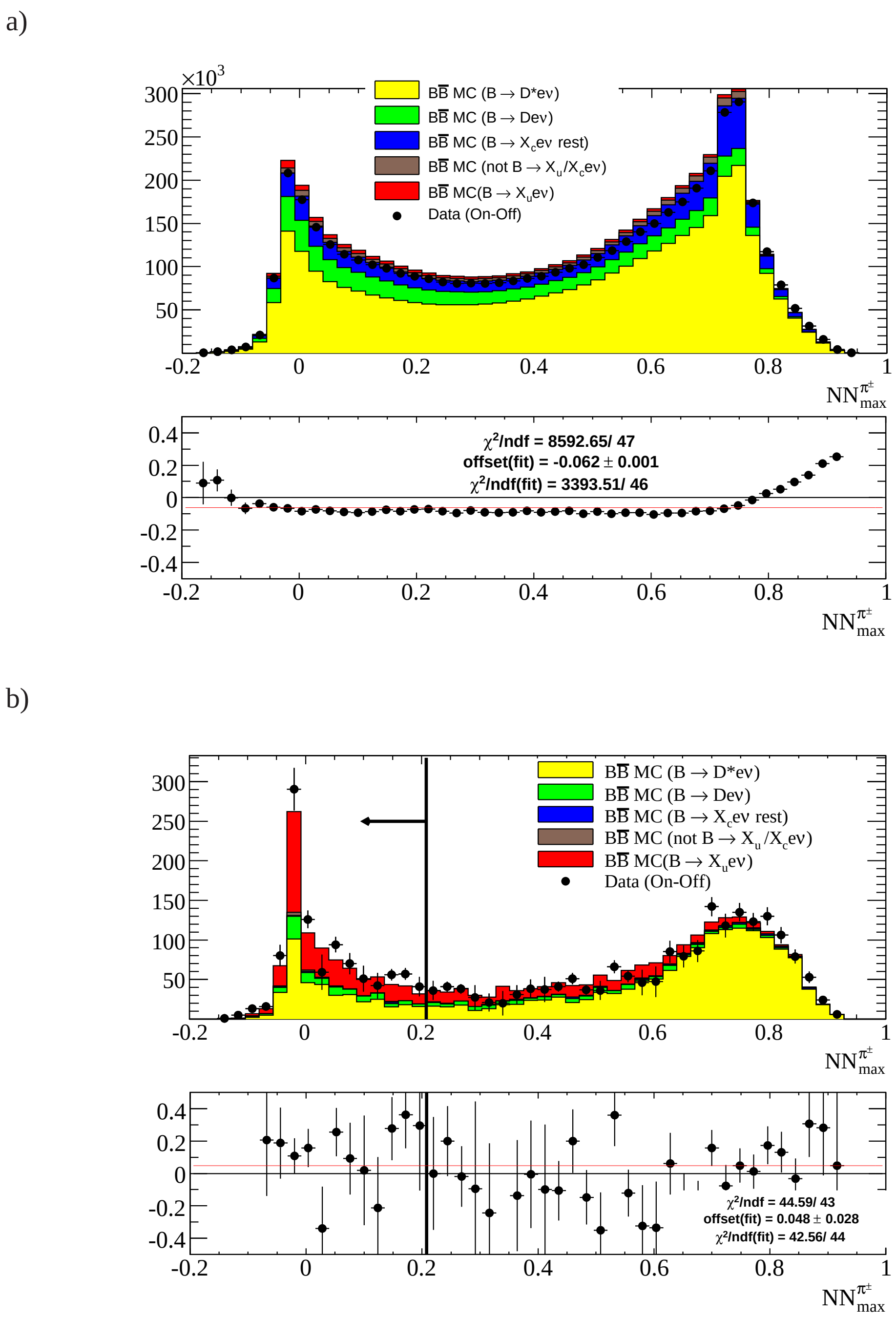

Figure 4.30: Data and MC distributions for $NN^{\pi^\pm}_{\mathrm{max}}$ after applying a) the preselection and b) the refined selection requirements. Note that $NN^{\pi^\pm}_{\mathrm{max}}$ distributions do not contain events where no partial $B \to D^* e\nu_e$ candidates were reconstructed. The plots follow the same conventions as those of figure 4.24.

a)

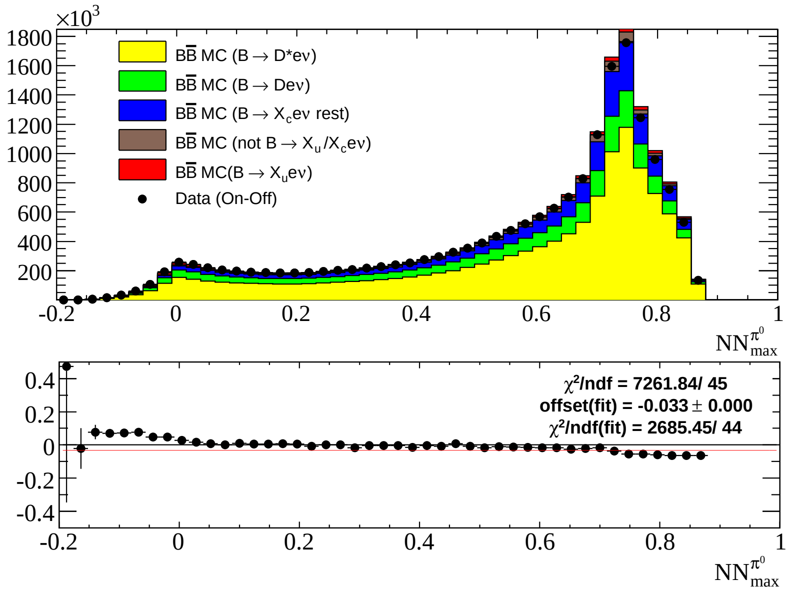

b)

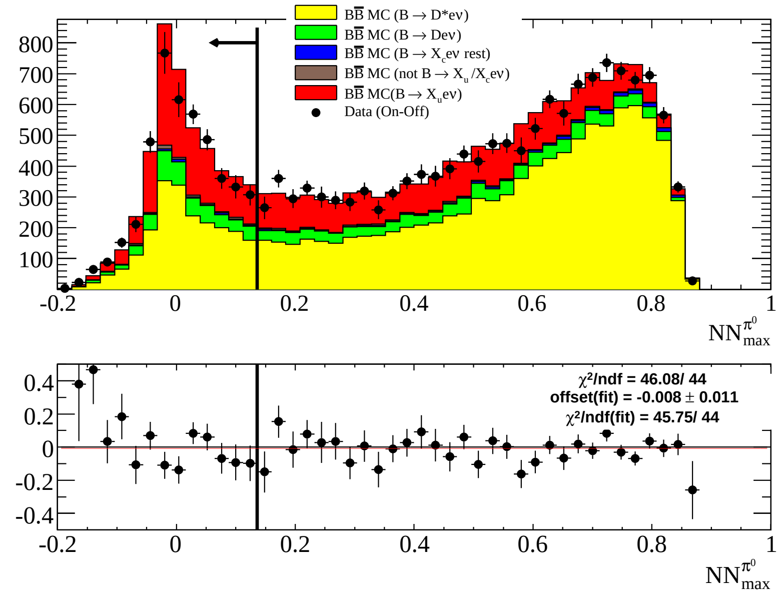

Figure 4.31: Data and MC distributions for $NN^{\pi^0}_{\mathrm{max}}$ after applying a) the preselection and b) the refined selection requirements. Note that $NN^{\pi^0}_{\mathrm{max}}$ distributions do not contain events where no partial $B \to D^* e\nu_e$ candidates were reconstructed. The plots follow the same conventions as those of figure 4.24.

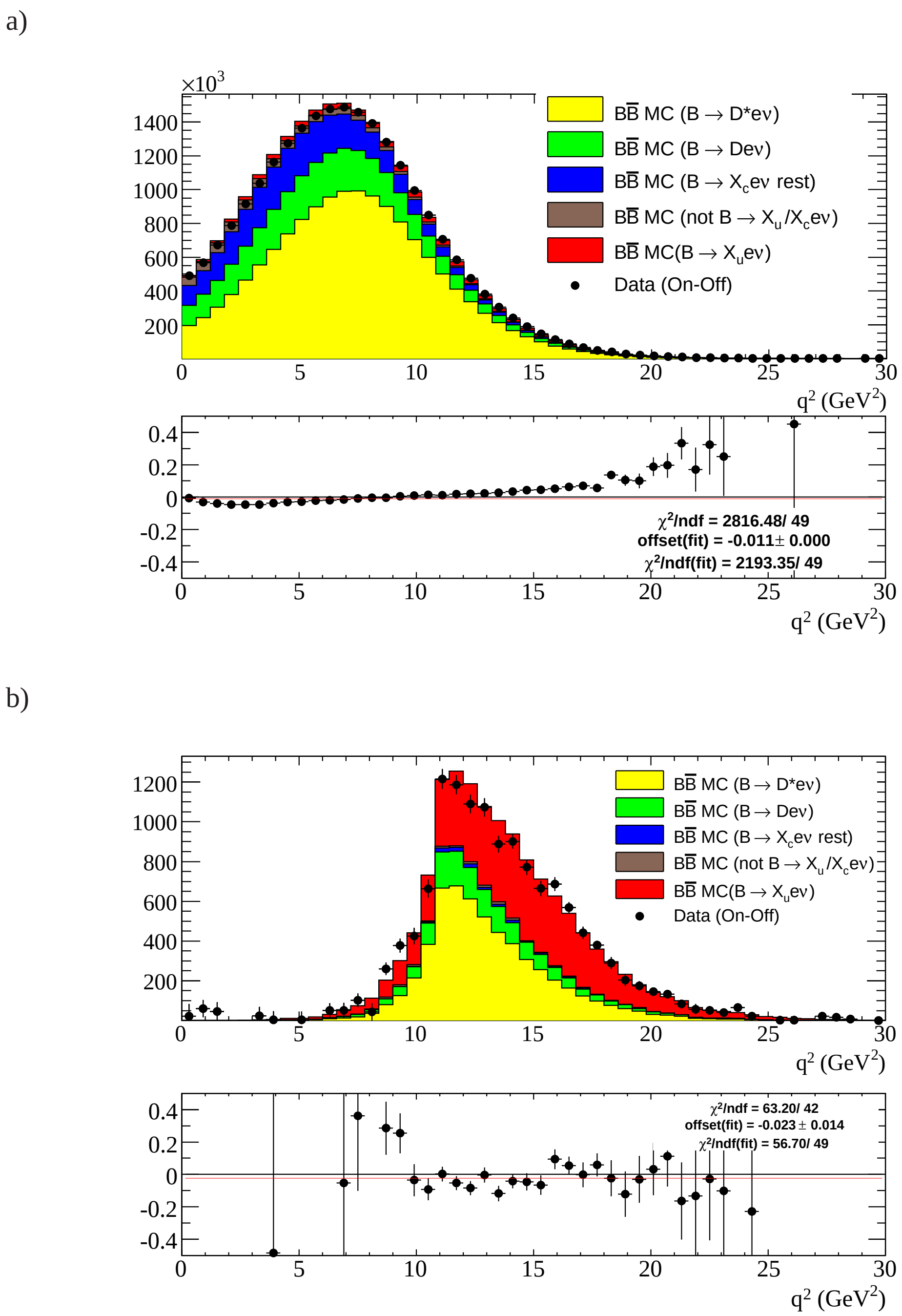

Figure 4.32: Data and MC distributions for q^2 after applying a) the preselection and b) the refined selection requirements. The plots follow the same conventions as those of figure 4.24

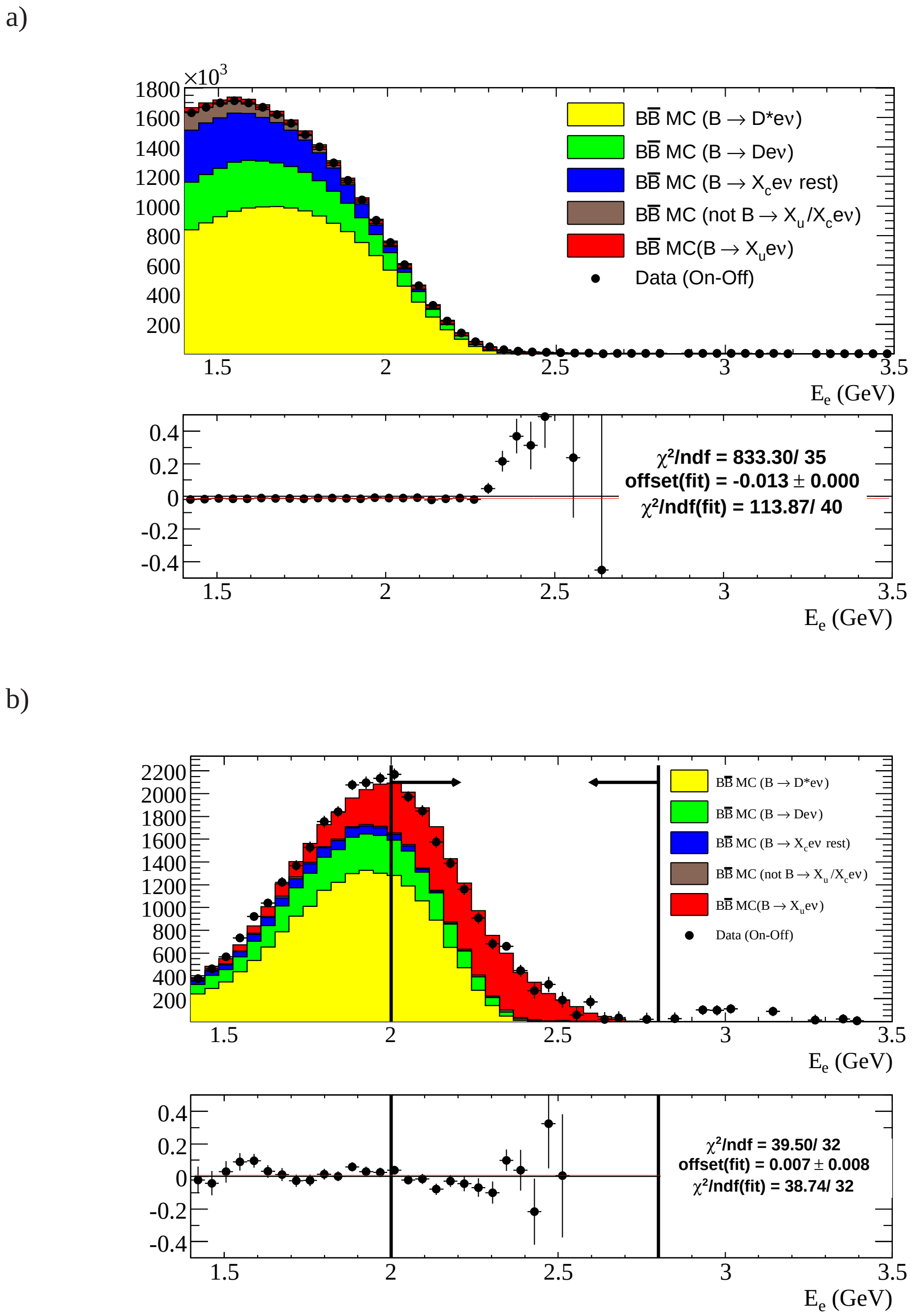

Figure 4.33: Data and MC distributions for E_e after applying a) the preselection and b) the refined selection requirements. The plots follow the same conventions as those of figure 4.24

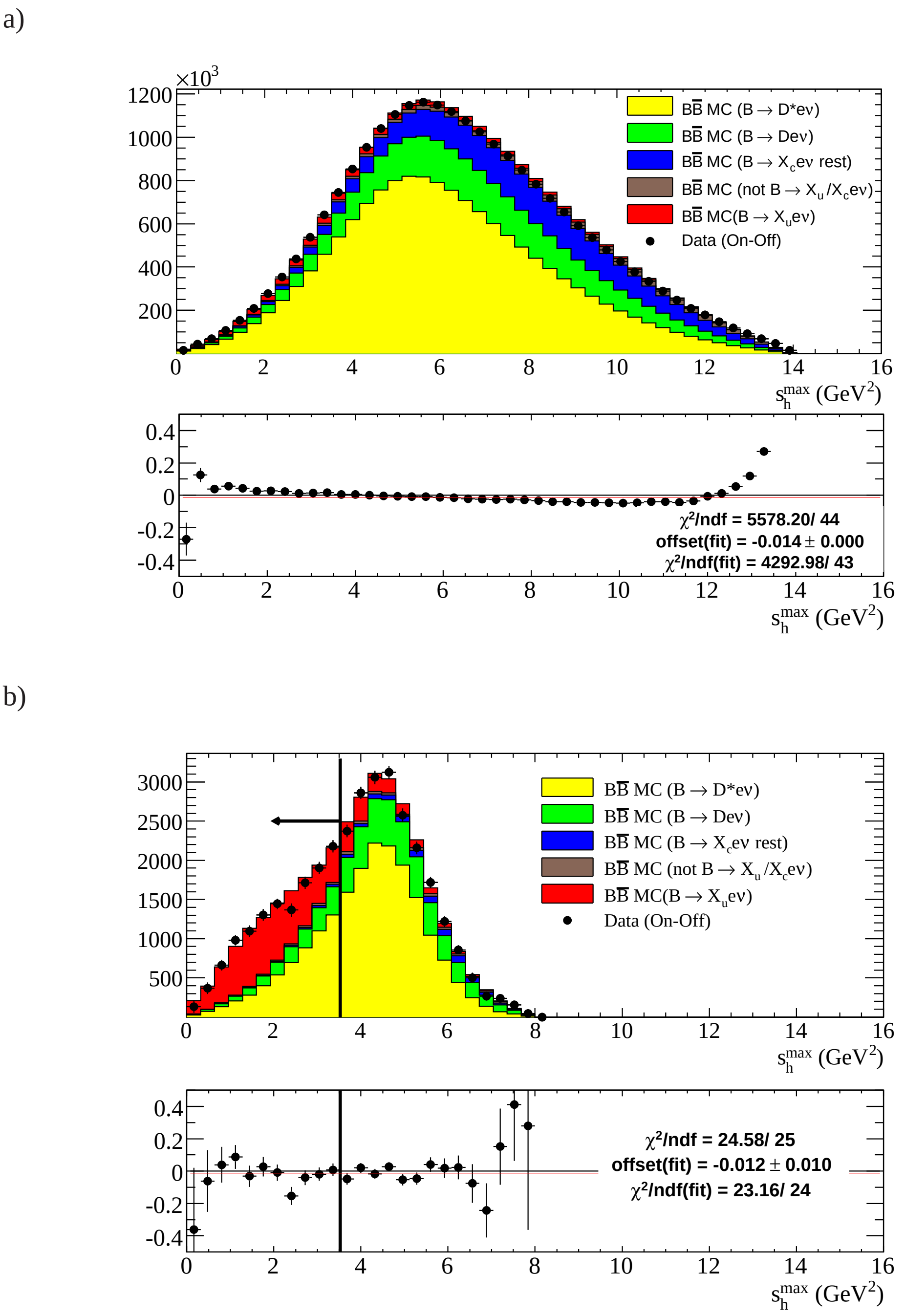

Figure 4.34: Data and MC distributions for s_h^{max} after applying a) the preselection and b) the refined selection requirements. The plots follow the same conventions as those of figure 4.24

5 Control Sample

In order to reduce the sensitivity of the signal efficiency predictions to the details of the Monte Carlo simulation, an independent control sample (CS) has been studied. This control sample contains $B \rightarrow D^0 e\overline{\nu}_e X$ decays, where the D^0 meson is reconstructed in the $K^-\pi^+$ decay channel accompanied by a possible additional low energy pion or photon from a D^* meson decay that is not reconstructed.
Section 5.1 gives a detailed overview of the selection of $B \rightarrow D^0 e\overline{\nu}_e$ events. In this context, the effects of the selection criteria are studied on the agreement between data and the simulation. The signal Monte Carlo efficiencies can then be corrected using $B \rightarrow D^0 e\overline{\nu}_e X$ control sample such that it reproduces the data selection efficiency more accurately. Corresponding studies of the selection efficiency are described in section 5.2 and their results are given in section 5.3. Control sample studies are performed using on-peak/off-peak and Monte Carlo data sets listed in Tables 4.1 and 4.2, respectively.

5.1 Selection of $B \rightarrow D^0 e\overline{\nu}_e$ events

The selection of $B \rightarrow D^0 e\overline{\nu}_e$ events is based on the studies performed in [1] including some modification as described in the following.
D^0 mesons are reconstructed in the decay chanel $D^0 \rightarrow K^+\pi^-$ by studying all possible combination of two charged tracks. The invariant $K^-\pi^+$ mass is required to be within 40 MeV/c^2 of the nominal D^0 mass of 1865 MeV/c^2 [53]. This wide mass window allows to define a D^0 mass signal region as well as sideband region in order to study background contributions from B decays. Finally, the D^0 meson is required to have a momentum $|P_{D^0}| > 0.5\,\mathrm{GeV}/c$.

A $B \rightarrow D^0 e\overline{\nu}_e$ event is identified by combining the reconstructed D^0 with the signal electron. For the selection of $B \rightarrow D^0 e\overline{\nu}_e$ candidates following selection criteria are applied:

- $m_{D^0 e} > 3.0\,\mathrm{GeV}/c^2$: the invariant mass of $D^0 e$ systems. This requirement is made to ensure that the $D^0 e$ combination originates from $B \rightarrow D^0 e\overline{\nu}_e X$ decays, as shown in Figure 5.1;

- $-1.5 < cos\Theta_{BY} < 1.1$: the cosine of the angle between B candidate and the vector sum of the D^0 and the electron candidate ($\equiv Y$ system) in the $\Upsilon(4S)$ rest frame. A detailed description of the $cos\Theta_{BY}$ variable is given in section 4.6.3. For correctly reconstructed $B \rightarrow D^0 e\overline{\nu}_e$ events $cos\Theta_{BY}$ must have values in the physical ± 1 range. Extensions of $cos\Theta_{BY} > 1$ for $B \rightarrow D^0 e\overline{\nu}_e$ events are due to detector resolution or mis-reconstructed particles. The lower negative values ($cos\Theta_{BY} < -1$) are produced by $B \rightarrow X_c e\overline{\nu}_e$ decays where X_c is a charm system, such a D^* or D^{**}, that produce a D^0. To reduce the influence of not well simulated semileptonic $B \rightarrow D^{**} e\overline{\nu}_e$ decays an lower bound of -1.5 is chosen. Figure 5.1 displays the $cos\Theta_{BY}$ distributions for Monte Carlo events.

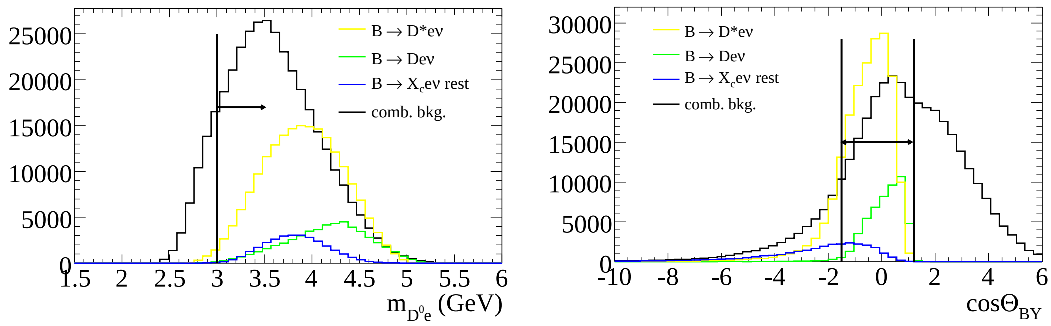

Figure 5.1: Distributions of the invariant mass of the D^0e system (left) and $cos\Theta_{BY}$ (right) in the $B \longrightarrow D^0 e\overline{\nu}_e X$ control sample for candidates in the D^0 mass window after applying the preselection outlined in section 4.4.1. The $B \longrightarrow D^0 e\overline{\nu}_e$ selection requirements are denoted by vertical lines. The combinatorial background can be subtracted using D^0 mass sidebands.

- $E_e > 1.9\,\mathrm{GeV}$: energy of the signal electron. This requirement is relaxed to $E_e > 1.7$ and 1.8 GeV to calculate alternative efficiency correction factors.

In addition, the event preselection criteria outlined in section 4.4.1 and refined requirements described in section 4.8.3 (with exception of the $B \longrightarrow D^* e\nu_e$ veto and $\mathrm{s_h^{max}}$cuts) are also applied for the control sample.

The above described kinematic requirements are applied to improve the purity of the control sample and to achieve a topology similar to the $B \longrightarrow X_u e\overline{\nu}_e$ signal events:

1. Since the one B meson is fully reconstructed in the control sample, the other B mesons decay generically. The decay of the other B meson in the event is unbiased by the $B \longrightarrow D^0 e\overline{\nu}_e$ selection procedure and therefore is identical to the other B meson decay in $B \longrightarrow X_u e\overline{\nu}_e$ signal events.;

2. No neutral hadrons or additional neutrinos are present in the decay chain. Therefore, the control sample can be used to correct for differencies in the simulation of the reconstruction of the tracks and clusters that come from other B meson decay.

Hence, the obtained correction factors for signal Monte Carlo efficiencies (see next section) from control sample studies can be applied to the signal efficiency of the $B \longrightarrow X_u e\overline{\nu}_e$ decays.

5.2 Adjusting the Monte Carlo Efficiency

The refined selection requirements outlined in section 4.8.3 render the efficiency predictions sensitive to the details of the Monte Carlo simulation. This sensitivity can be reduced using efficiencies for data and simulation obtained from $B \longrightarrow D^0 e\overline{\nu}_e X$ sample studies.
The calculation of the $B \longrightarrow D^0 e\overline{\nu}_e$ efficiencies is based on the extraction of yields inside the D^0 mass signal region corrected for the number of expected combinatorial background in

Table 5.1: The signal (N_{sig}) and the background (N_{bkg}) yields in the $B \to D^0 e \overline{\nu}_e X$ control sample within D^0 mass signal region for data and Monte Carlo simulation after applying successively the selection requirements. The events of the simulation are scaled to the number of $B\overline{B}$ in data. Note that the errors shown are purely statistical.

	Data		**MC**	
Criteria	N_{sig}	N_{bkg}	N_{sig}	N_{bkg}
Preselection	374580 ± 1147	70906 ± 652	380454 ± 447	65051 ± 237
Bhabha veto	368473 ± 1125	69431 ± 634	375842 ± 444	63932 ± 234
N_{lep}	302461 ± 1035	51749 ± 574	307871 ± 402	48275 ± 216
$cos\Theta_{\text{miss}}$	184595 ± 801	30174 ± 474	186556 ± 314	28458 ± 170
$cos\Theta_{\text{e-T}}$	83927 ± 370	13027 ± 175	83942 ± 212	11868 ± 118
$E_{\text{miss}} - \lvert P_{\text{miss}} \rvert$	21241 ± 181	2572 ± 78	20906 ± 97	2345 ± 43
$E_e > 1.7\,\text{GeV}$	11965 ± 145	1104 ± 85	11746 ± 69	1114 ± 24
$E_e > 1.8\,\text{GeV}$	8450 ± 106	780 ± 38	8465 ± 59	688 ± 24
$E_e > 1.9\,\text{GeV}$	5202 ± 82	443 ± 30	5315 ± 46	380 ± 16

this region. The signal region is defined by a $\pm 11\,\text{MeV}/c^2$ window around the the fitted D^0 mass peak corresponding to a $\pm 2\sigma$ window where σ is the fitted mass resolution. The sideband regions are then selected by requiring the invariant mass to be $m_{K\pi} < 1.835\,\text{GeV}/c^2$ and $m_{K\pi} > 1.890\,\text{GeV}/c^2$, as illustrated in Figure 5.2. The functions used to fit the D^0 mass distribution consist of two Gaussian functions to describe signal events and one polynomial of first order to describe the combinatorial background contribution:

$$f(m) = \left[P_1 \exp\frac{(m-P_2)^2}{2P_3^2} + P_4 \exp\frac{(m-P_5)^2}{2P_6^2} \right] + (m \cdot P_7 + P_8), \tag{5.1}$$

where the P_i's are free parameters. The parameter P_2 is interpreted as the D^0 mass, m_{D^0}, which can be compared to the nominal D^0 mass of 1864.8 GeV/c^2 [53] and the parameter P_3 as the width, σ, of the D^0 signal distribution.

Figure 5.2 displays the $m_{K\pi}$ spectra for both data and Monte Carlo simulation after applying the selection requirements outlined in section 5.1.

The differences between the fitted m_{D^0} in data and the Monte Carlo simulation are very small ($< 1\,\text{MeV}$). Furthermore, the fitted value, m_{D^0}, in the Monte Carlo simulation is in a very good agreement with the value (1864.8 GeV/c^2) used as input in the simulation. To validate the fit method described above the number of fitted signal yields is compared to the number of true generated $B \to D^0 e \overline{\nu}_e X$ events inside the signal region using generator level information. A reasonable agreement has been found between these two numbers: e. g. for the selection requirements outlined in section 5.1 and $E_e > 1.9\,\text{GeV}$ the number of true generated $B \to D^0 e \overline{\nu}_e X$ events is 5361 ± 42 where the fitted number of $B \to D^0 e \overline{\nu}_e X$ events is 5315 ± 46.

The signal yields, N_{sig}, are computed as a difference of total and background yields, N_{bkg}, obtained from the fits in the D^0 mass signal region. Table 5.1 shows the corresponding yields for data and simulation after applying successively the selection requirements. These yields can be used to form marginal and cumulative efficiencies. Table 5.2 provides an

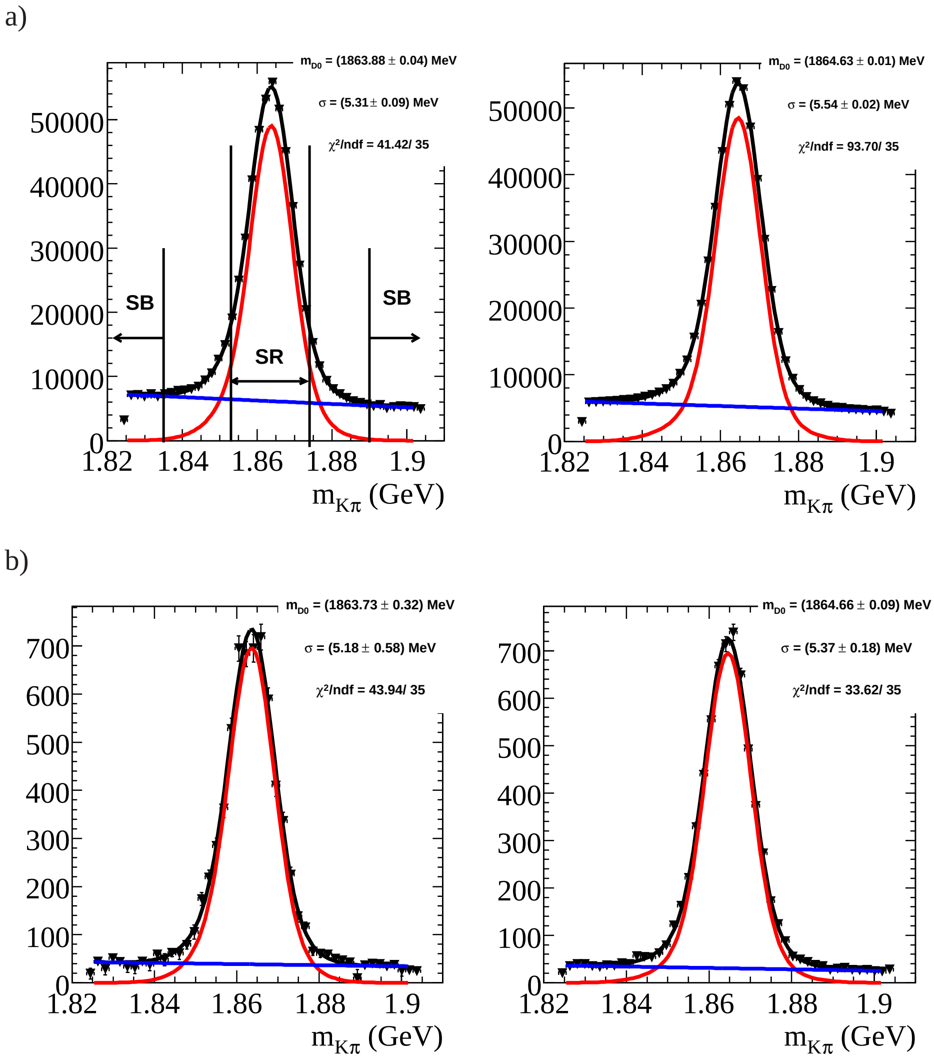

Figure 5.2: D^0 mass spectra for data (left) and simulation (right) in the $B \to D^0 e \overline{\nu}_e X$ control sample after applying a) the preselection and b) the refined selection requirements. The latter plot displays D^0 mass distributions for $E_e > 1.9\,\mathrm{GeV}$. The signal region (SR) is defined as within 2σ ($\sim 11\,\mathrm{MeV}/c^2$) of the fitted D^0 mass peak. The sideband regions (SB) are selected by requiring the invariant mass to be $m_{K\pi} < 1.835\,\mathrm{GeV}/c^2$ and $m_{K\pi} > 1.890\,\mathrm{GeV}/c^2$. The combinatorial background is described by a polynomial of first order (blue) and the signal events by two Gaussian functions (red). The sum of the signal and the background functions is denoted by the black line.

overview about corresponding efficiencies, where the sample satisfying the $B \to D^0 e \overline{\nu}_e$ selection requirements defined the denominator in computing the efficiencies. For each selection criterion, comparable marginal efficiencies are obtained for data and simulation.

Table 5.2: Marginal and cumulative efficiencies in the $B \to D^0 e \overline{\nu}_e X$ control sample for data and Monte Carlo simulation after applying successively the selection requirements. Marginal efficiencies for various lepton energy cuts are computed with respect to the yields obtained after applying the $E_{\text{miss}} - |P_{\text{miss}}|$ requirement. Note that the errors shown are purely statistical and all efficiencies are expressed in units of $\times 10^{-2}$.

	Data		**MC**	
Criteria	marg. ε	cumul. ε	marg. ε	cumul. ε
Preselection	100.00 ± 0.00	100.00 ± 0.00	100.00 ± 0.00	100.00 ± 0.00
Bhabha veto	98.37 ± 0.02	98.37 ± 0.02	98.79 ± 0.01	98.79 ± 0.01
N_{lep}	82.09 ± 0.06	80.75 ± 0.06	81.92 ± 0.04	80.92 ± 0.04
$cos\Theta_{\text{miss}}$	61.03 ± 0.09	49.28 ± 0.08	60.60 ± 0.05	49.04 ± 0.05
$cos\Theta_{\text{e}-\text{T}}$	45.47 ± 0.12	22.41 ± 0.07	45.00 ± 0.07	22.06 ± 0.04
$E_{\text{miss}} - \lvert P_{\text{miss}}\rvert$	25.31 ± 0.15	5.67 ± 0.04	24.91 ± 0.08	5.49 ± 0.02
$E_e > 1.7\,\text{GeV}$	56.33 ± 0.34	3.19 ± 0.03	56.19 ± 0.20	3.09 ± 0.02
$E_e > 1.8\,\text{GeV}$	39.78 ± 0.34	2.26 ± 0.02	40.49 ± 0.19	2.22 ± 0.01
$E_e > 1.9\,\text{GeV}$	24.49 ± 0.30	1.39 ± 0.02	25.42 ± 0.17	1.40 ± 0.01

Table 5.3: Efficiency correction factors for various requirements on E_e. The $D^0 e\nu$ efficiencies are taken from table 5.2 and correspond to the cumulative efficiencies after applying the E_e requirements. Note that the errors shown are purely statistical and all efficiencies are expressed in units of $\times 10^{-2}$.

	lower bound on E_e in [GeV]		
	1.7	1.8	1.9
$\varepsilon^{\text{data}}_{D^0 e\nu}$	3.194 ± 0.029	2.256 ± 0.024	1.390 ± 0.019
$\varepsilon^{\text{MC}}_{D^0 e\nu}$	3.087 ± 0.016	2.225 ± 0.014	1.397 ± 0.011
$\varepsilon^{\text{data}}_{D^0 e\nu} / \varepsilon^{\text{MC}}_{D^0 e\nu}$	1.035 ± 0.011	1.014 ± 0.013	0.995 ± 0.016

The Monte Carlo prediction for the $B \to X_u e \overline{\nu}_e$ signal efficiency is then adjusted according to

$$\varepsilon_u^{\text{data}} = \varepsilon_u^{\text{MC}} \left(\frac{\varepsilon^{\text{data}}_{D^0 e\nu}}{\varepsilon^{\text{MC}}_{D^0 e\nu}} \right), \tag{5.2}$$

where the above $D^0 e\nu$ efficiencies are taken from table 5.2 and correspond to the cumulative efficiencies after applying the E_e requirements.

5.3 Results of the Control Sample Studies

Table 5.3 shows the efficiency correction factors for various requirements of the lower bound on the electron energy. There is a slight dependency of the correction factor on E_e which can not be explained due to statistical fluctuation. Therefore, the requirements on E_e

for the calculation of the efficiency correction factor must be adjusted to the requirements on the lepton energy for $B \rightarrow X_u e \overline{\nu}_e$ events selection. In this analysis, different efficiency correction factors are applied computed by requiring the same selection criteria on electron energy for the control sample as well as for the $B \rightarrow X_u e \overline{\nu}_e$ event reconstruction. Stability scans described in section 8.2 show that the dependency of the extracted $B \rightarrow X_u e \overline{\nu}_e$ branching fractions on the lower bound of the electron energy vanishes by applying a signal efficiency correction factor calculated for the same requirements on E_e as in case of $B \rightarrow X_u l \nu$ event selection. In order to have sufficient statistics for the reconstruction of the $B \rightarrow D^0 e \overline{\nu}_e$ events, the signal correction factors can only be evaluated for the maximal requirement $E_e > 1.9\,\mathrm{GeV}$. The correction factor obtained for this lepton energy cut is used also to correct the $B \rightarrow X_u e \overline{\nu}_e$ signal efficiency for $E_e > 2.0\,\mathrm{GeV} \ldots E_e > 2.2\,\mathrm{GeV}$. When the systematic studies are performed (see chapter 7) the correction factors are also taken into account.

Figures from 5.3 to 5.8 display various kinematical distributions for events satisfying the $B \rightarrow D^0 e \overline{\nu}_e$ and refined selection requirements listed in section 4.8.3. All of these selected criteria were applied in producing the plots except when a cut corresponded to the variable plotted, in which case the selected region is denoted by an arrow. The requirements on $s_{\mathrm{h}}^{\mathrm{max}}$ and $B \rightarrow D^* e \nu_e$ veto are omitted since they are designed to remove semileptonic $B \rightarrow X_c e \overline{\nu}_e$ decays and would suppress the control sample. The plots shown are produced by selecting events within the D^0 mass windows and subtracting the corresponding distributions for events with $K^- \pi^+$ invariant masses in the D^0 mass sideband region. The distributions from the side band region are scaled to the number of combinatorial background events in the signal region obtained from the fit to the D^0 mass distribution.

The apparent discrepancies for the yields in data and simulation ($\sim 3\%$) are well within background systematics, as will be discussed in chapter 7.

a)

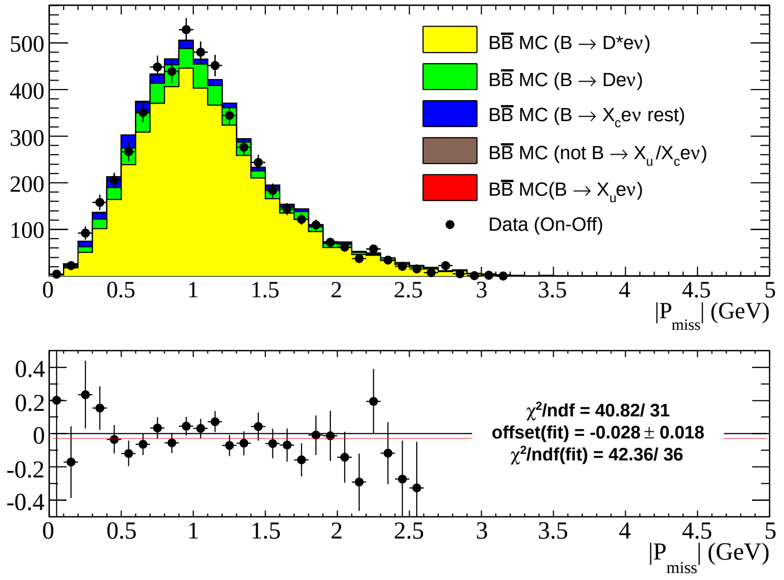

b)

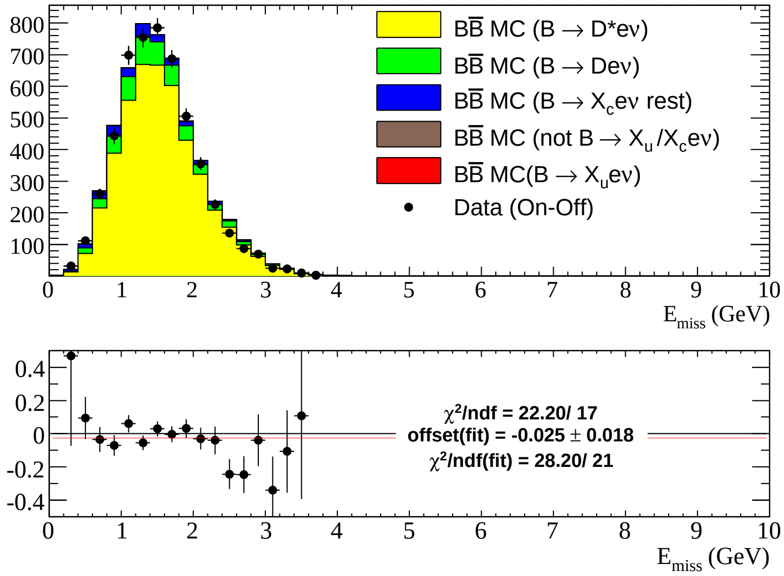

Figure 5.3: Data and MC distributions for a) $|P_{\rm miss}|$ and b) $E_{\rm miss}$ after applying the refined selection requirements and requirement on $E_e > 1.9\,\mathrm{GeV}$. The plots follow the same conventions as those of Figure 4.24.

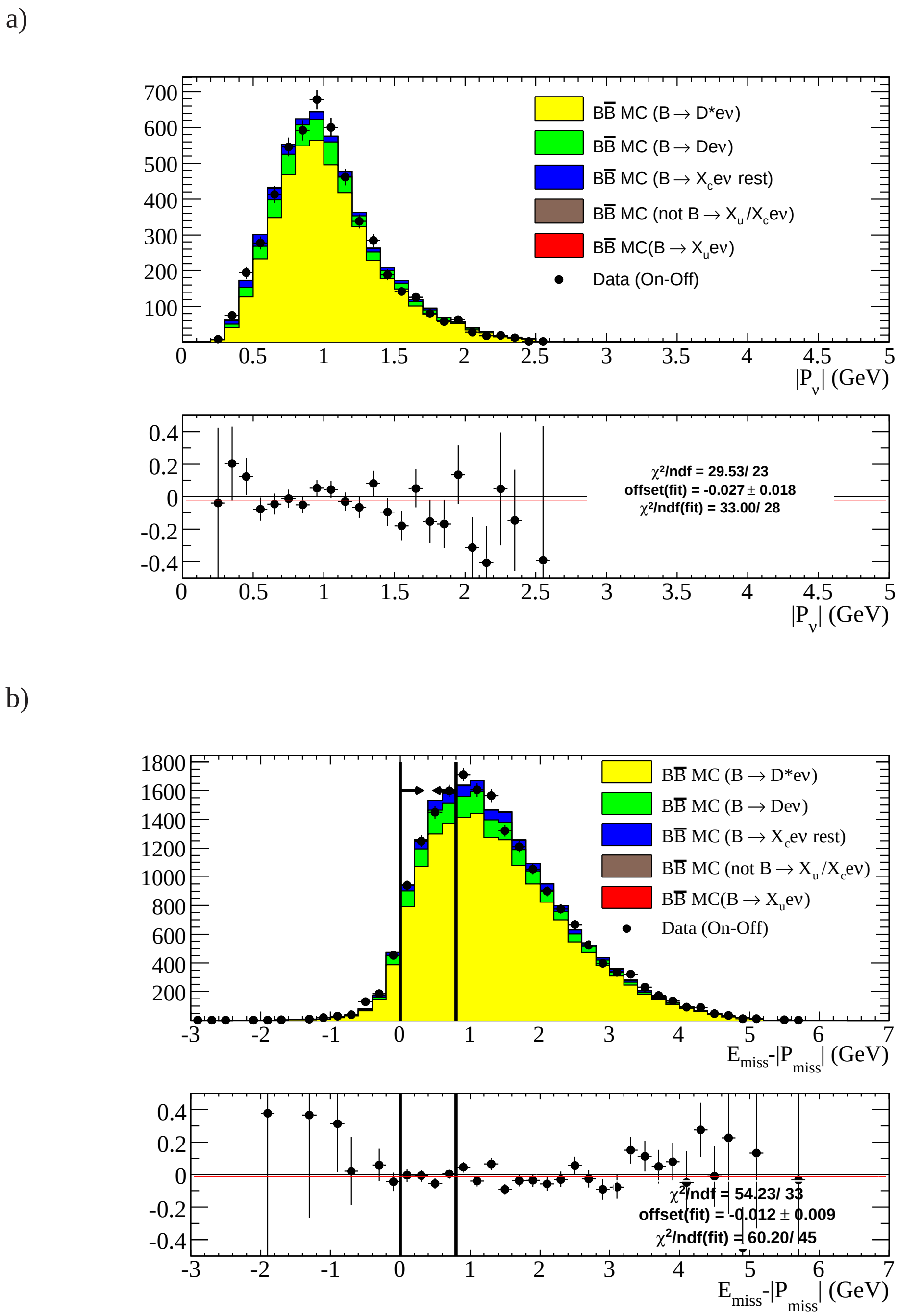

Figure 5.4: Data and MC distributions for a)$|P_\nu|$ and b) $E_{\text{miss}} - |P_{\text{miss}}|$ after applying the refined selection requirements and requirement on $E_e > 1.9\,\text{GeV}$. The plots follow the same conventions as those of Figure 4.24.

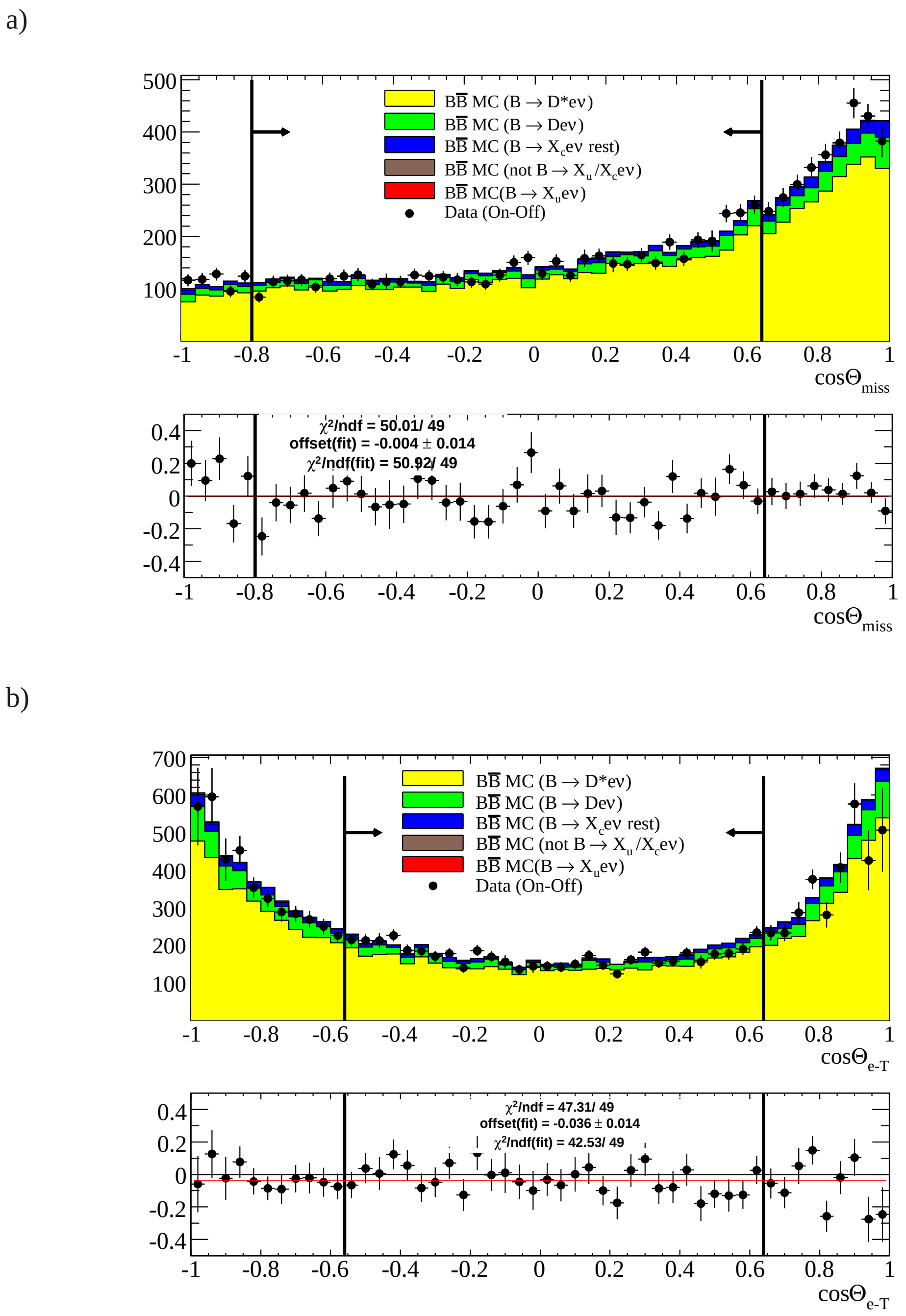

Figure 5.5: Data and MC distributions for a) $cos\Theta_{\mathrm{miss}}$ and b) $cos\Theta_{\mathrm{e-T}}$ after applying the refined selection requirements and requirement on $E_e > 1.9\,\mathrm{GeV}$. The plots follow the same conventions as those of Figure 4.24.

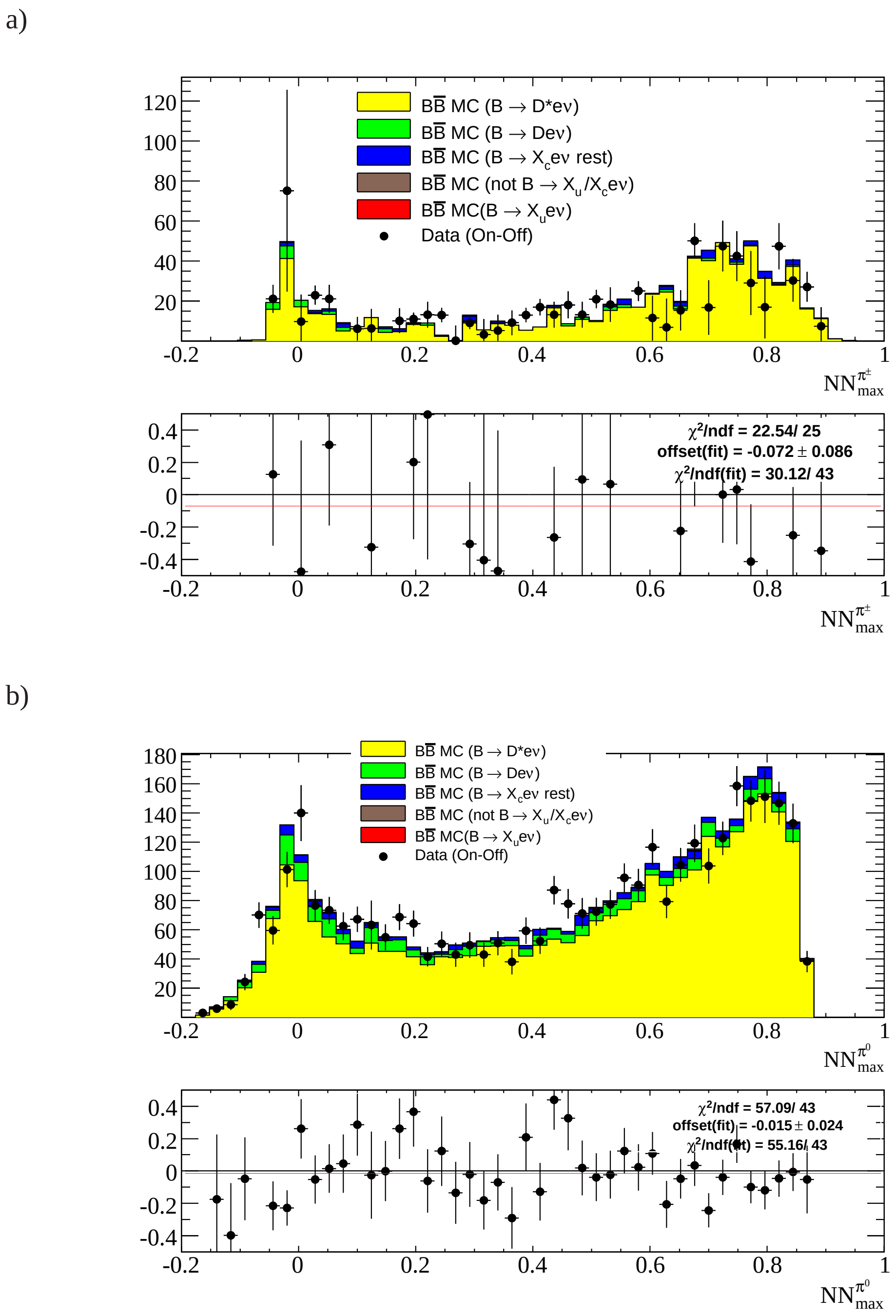

Figure 5.6: Data and MC distributions for a) $NN^{\pi^\pm}_{\max}$ and b) $NN^{\pi^0}_{\max}$ after applying the refined selection requirements and requirement on $E_e > 1.9\,\mathrm{GeV}$. Note that $NN^{\pi^\pm}_{\max}/NN^{\pi^0}_{\max}$ distributions do not contain events where no partial $B \to D^* e \nu_e$ candidates were reconstructed. The plots follow the same conventions as those of Figure 4.24.

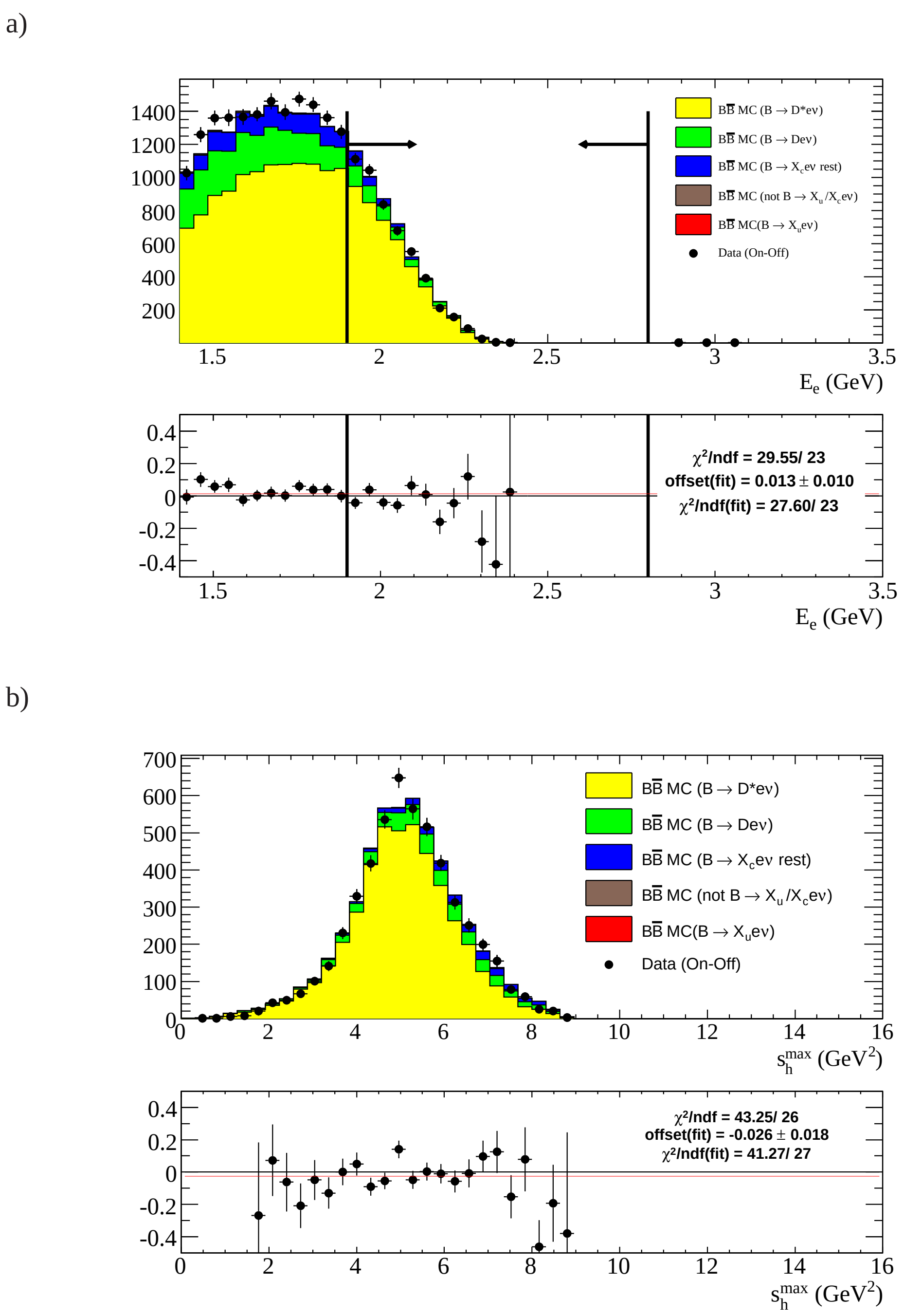

Figure 5.7: Data and MC distributions for a) E_e and b) $s_{\mathrm{h}}^{\mathrm{max}}$ after applying the refined selection requirements and requirement on $E_e > 1.9\,\mathrm{GeV}$. The plots follow the same conventions as those of Figure 4.24.

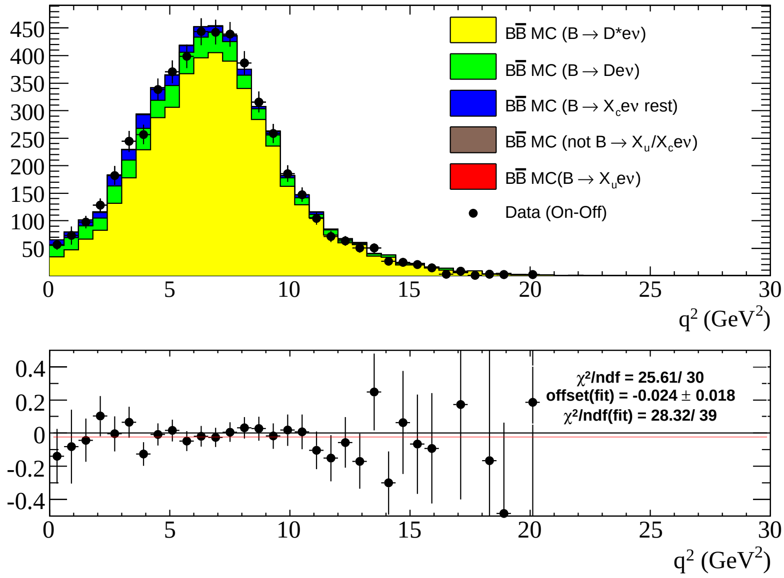

Figure 5.8: Data and MC distributions for q^2 after applying the refined selection requirements and requirement on $E_e > 1.9\,\text{GeV}$. The plots follow the same conventions as those of Figure 4.19.

6 Signal Extraction

6.1 Signal Extraction Procedure

Since the simulation of background events appears to be adequate (see section 4.9) and a correction factor for signal effciency has been determined (chapter 5), one may proceed to the next stage of the analysis. In order to extract $\Delta\mathcal{B}(B \to X_u e\overline{\nu}_e)$, the yield for events satisfying the event selection outlined in section 4.8.3 is extracted for both data and the simulation.

The partial branching fraction, $\Delta\mathcal{B}\ (B \to X_u e\overline{\nu}_e)$, unfolded for the detector efficiency is defined as

$$\begin{aligned}
\Delta\mathcal{B}\ (B \to X_u e\overline{\nu}_e) &= \mathcal{B}(B \to X_u e\overline{\nu}_e)\, f_u \\
&= \frac{N^{\text{data}}_{\text{cand}} - N^{\text{MC}}_{\text{bkg}}}{2N_{B\bar{B}}\varepsilon_u} f_u \\
&= \frac{N^{\text{data}}_{\text{cand}} - N^{\text{MC}}_{\text{bkg}}}{\varepsilon_{\text{sig}} 2N_{B\bar{B}}} \left[1 + \left(\frac{1}{f_u} - 1\right)\frac{\varepsilon_{\overline{\text{sig}}}}{\varepsilon_{\text{sig}}}\right]^{-1}, \qquad (6.1)
\end{aligned}$$

where N^{data} is the number of candidates in data, $N^{\text{MC}}_{\text{bkg}}$ the number of background events estimated from Monte Carlo simulation, $N_{B\bar{B}} = 454.21 \times 10^6$ the number of analyzed $\Upsilon(4S) \to B\bar{B}$ decays, and f_u the fraction of $B \to X_u e\overline{\nu}_e$ decays that fall in the true signal region. The signal efficiency ε_u may be expanded as

$$\varepsilon_u = \varepsilon_{\text{sig}} f_u + \varepsilon_{\overline{\text{sig}}}(1 - f_u)\,. \qquad (6.2)$$

The efficiencies ε_{sig} and $\varepsilon_{\overline{\text{sig}}}$ are obtained from the Monte Carlo simulation and give the efficiencies to reconstruct target and non-target events in the selected signal region. In this analysis the target region is defined by the cut on the unsmeared kinematic variables $s^{\text{max}}_{\text{h,true}}$ and $E_{e,\text{true}}$ in the $\Upsilon(4S)$ rest frame. The cut value are the same as for the corresponding measured variables $s^{\text{max}}_{\text{h}}$ and E_e. As an alternative the target region can be defined in the B meson rest frame. In the latter case the extracted partial branching fraction may be more sensitive [52] to the variation of Shape Function parameters a and m_b (see section 7.2). Therefore, the signal extraction is performed in the $\Upsilon(4S)$ rest frame.

Figure 6.1 shows the distribution of the reconstructed $B \to X_u e\overline{\nu}_e$ events in the true $q^2 - E_e$ plane for simulated events after the refined selection. The events generated outside the signal (target) region feed into the signal region mainly due to the limited q^2 resolution. The determination of f_u is based on a theoretical calculation and hence depends on the underlying model. As a consequence of the small ratio $\varepsilon_{\overline{\text{sig}}}/\varepsilon_{\text{sig}}$ ($\mathcal{O} \sim 10^{-2}$) the dependency of the extracted $\Delta\mathcal{B}$ value on f_u and hence the sensitivity to the theoretical model for $B \to X_u e\overline{\nu}_e$ decays is reduced.

In order to minimize the influence of the simulation of $B\bar{B}$ background and the sensitivity of the signal efficiency prediction, two control samples are used.

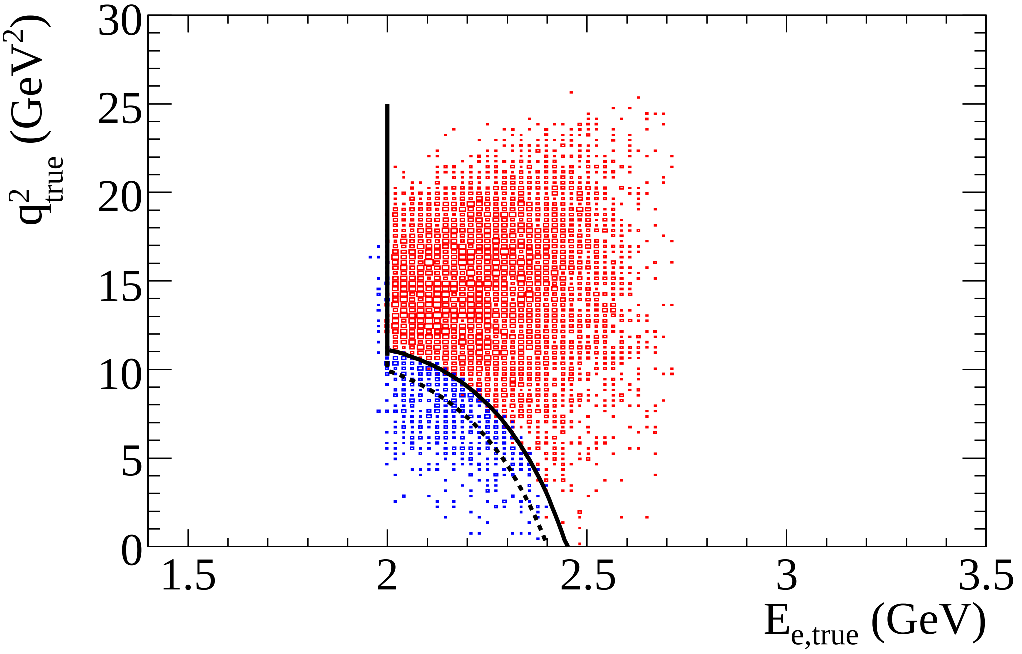

Figure 6.1: The distribution of generated $B \rightarrow X_u e \overline{\nu}_e$ events wich have been reconstructed in the $q^2 - E_e$ signal region. The black solid lines define the target region: the vertical line corresponds to the lepton energy cut ($E_e < 2.0\,\mathrm{GeV}$), the solide curve to the cut, $s_{\mathrm{h}}^{\mathrm{max}} < 3.52\,\mathrm{GeV}^2$. The events (in blue color) generated outside the target region may feed into the signal region. Events denoted by the red color have been generated in the target region. The dashed curve represents the cut, $s_{\mathrm{h}}^{\mathrm{max}} < 4.00\,\mathrm{GeV}^2$.

Table 6.1: Relative contributions of various B decay modes to the total number of selected events for the signal region ($s_{\mathrm{h}}^{\max} < 3.52\,\mathrm{GeV}^2$) and the $s_{\mathrm{h}}^{\max}$sideband ($s_{\mathrm{h}}^{\max} > 4.48\,\mathrm{GeV}^2$) in Monte Carlo simulation. All events satisfy the refined event selection outlined in section 4.8.3. Requirement on the lower bound of the electron energy is 2.0 GeV.

Decay mode X	N_X/N_{tot} ($s_{\mathrm{h}}^{\max} < 3.52\,\mathrm{GeV}^2$)[%]	N_X/N_{tot} ($s_{\mathrm{h}}^{\max} > 4.48\,\mathrm{GeV}^2$)[%]
$B \to D^*\ell\nu$	41.8	65.4
$B \to D\ell\nu$	11.9	23.7
$B \to X_c^{rest} l\nu$	1.0	4.4
$B \to X_{other} l\nu$	1.2	1.7
$B \to X_u e\overline{\nu}_e$	44.1	4.8

The partial branching fraction extraction sensitivity to the signal efficiency prediction is reduced by the $B \to D^0 e\overline{\nu}_e X$ control sample, which is described in chapter 5. The corresponding correction factor obtained from this control sample is defined as

$$F_{D^0e\nu}^{corr} = \varepsilon_{D^0e\nu}^{data}/\varepsilon_{D^0e\nu}^{MC}, \tag{6.3}$$

where $\varepsilon_{D^0e\nu}^{data}$ and $\varepsilon_{D^0e\nu}^{MC}$ are the selection efficiency for $B \to D^0 e\overline{\nu}_e X$ events in data and Monte Carlo simulation, respectively. The applied signal effciciency correction ($F_{D^0e\nu}^{corr} \cdot \varepsilon_u$) results in smaller systematic uncertainties as separate studies have shown. To adjust the Monte Carlo background estimation in the signal region the yields in data, N_{SB}^{data}, and simulation, N_{SB}^{MC}, for the $s_{\mathrm{h}}^{\max}$sideband region ($s_{\mathrm{h}}^{\max} > 4.48\,\mathrm{GeV}^2$) are compared and a correction factor is computed as

$$F_{SB}^{corr} = N_{SB}^{data}/N_{SB}^{MC}. \tag{6.4}$$

This correction factor is then used to adjust the number of $B\bar{B}$ background events, N_{bkg}^{MC}, in the signal region.

Although the overall disagreements between data and simulation are taken into account by applying of F_{SB}^{corr} the current signal extraction procedure is not optimal. The calculation of the background correction factor does not take into account the different composition of $B \to X_c e\overline{\nu}_e$ sub-modes in the signal and sideband regions. Table 6.1 shows the relative contributions of B decay modes in the signal and sideband regions obtained from Monte Carlo simulation. As a consequence the corrected number of background events in the signal region may be overestimated or underestimated depending on the tuning parameters of Monte Carlo simulation (e. g. $\mathcal{B}(D^0 \to K^0 X)$ or tracking and photon reconstruction efficiencies). However, as shown in the following sections, this possible bias is taken into account by the systematic evaluation procedure. Furthermore, studies on Monte Carlo simulation used as data have been shown, that the systematic on $\Delta\mathcal{B}$ fully cover the bias on the background correction factor F_{SB}^{corr}.

The possible improvement of the signal extraction procedure in the future could be a fit to the data in the $s_{\mathrm{h}}^{\max}$sideband region for the different background contributions.

After the adjustment of the signal efficiency and the background estimates the final formula for the extraction of the partial branching fraction is given by

$$\Delta\mathcal{B}\left(B \to X_u e \overline{\nu}_e\right) = \frac{N_{\text{cand}}^{\text{data}} - N_{\text{bkg}}^{\text{MC}} F_{SB}^{corr}}{2N_{B\bar{B}}\varepsilon_{\text{sig}} F_{D^0 e\nu}^{corr}} \left[1 + \left(\frac{1}{f_u} - 1\right)\frac{\varepsilon_{\overline{\text{sig}}}}{\varepsilon_{\text{sig}}}\right]^{-1}. \tag{6.5}$$

7 Systematic Uncertainties

In this chapter various sources of systematic uncertainties are discussed. In all cases where a killing technique[1] has been applied (e. g. track and photon selection efficiency), the uncertainties can only be evaluated in one direction (+ or -). Therefore, for these cases the systematics are symmetrized. In other cases the largest discrepancy (+ or -) was taken as systematic error.

7.1 Evaluation Procedure for Systematic Uncertainties

The exctraction of the partial branching fraction is affected by various systematic uncertainties. For instance the number of estimated background events in simulation depends on the charm background branching fractions and the modeling of the detector affects the signal efficiency as well as the amount of estimated background. The influence of all such effects is studied by adjusting the Monte Carlo simulation to reflect each source of the systematic uncertainties. The analysis was then repeated by measuring of an alternative partial branching fraction $\Delta\mathcal{B}'$. The size of systematic uncertainties is derived from the change of the extracted partial branching fraction $\Delta\mathcal{B}'$ with respect to the nominal $\Delta\mathcal{B}$.

$$\sigma(\Delta\mathcal{B}) = \frac{\Delta\mathcal{B}' - \Delta\mathcal{B}}{\Delta\mathcal{B}} \tag{7.1}$$

The sources of systematics taken into account are discussed in the following sections.

7.2 Signal simulation

Since the signal simulation is based on the hybrid model, as discussed in section 4.3.1, the influence of the modeling of resonant and non-resonant components have to be investigated.

To evaluate the systematic uncertainties on $\Delta\mathcal{B}$ arising from the modeling of the resonant $B \rightarrow X_u e \overline{\nu}_e$ decays, the corresponding branching fractions (see Table 4.3) in the simulation are varied within their uncertainties. New hybrid models obtained from the exclusive branching fraction modification are built and alternative partial $B \rightarrow X_u e \overline{\nu}_e$ branching fractions are extracted. The corresponding uncertainties are listed in Table 7.2.

The other source of systematic uncertainties in $B \rightarrow X_u e \overline{\nu}_e$ modeling comes from the HQE parameters, which affect the non-resonant part of the hybrid model. The underlying theoretical model [23] used to generate the non-resonant $B \rightarrow X_u e \overline{\nu}_e$ Monte Carlo events, depends at first order on two Shape Function parameters a and m_b which can be derived from HQE parameters λ_1 and $\overline{\Lambda}$ as described in sections 2.2.2.1 and 4.3.1. To be conservative and to follow the suggestion of theorists, the systematic uncertainty on the partial branching fraction is evaluated as the maximum deviations of extracted $\Delta\mathcal{B}$ using $2-\sigma$

---

[1] MC objects such as tracks or photons are removed randomly with a given probabilty from the simulation

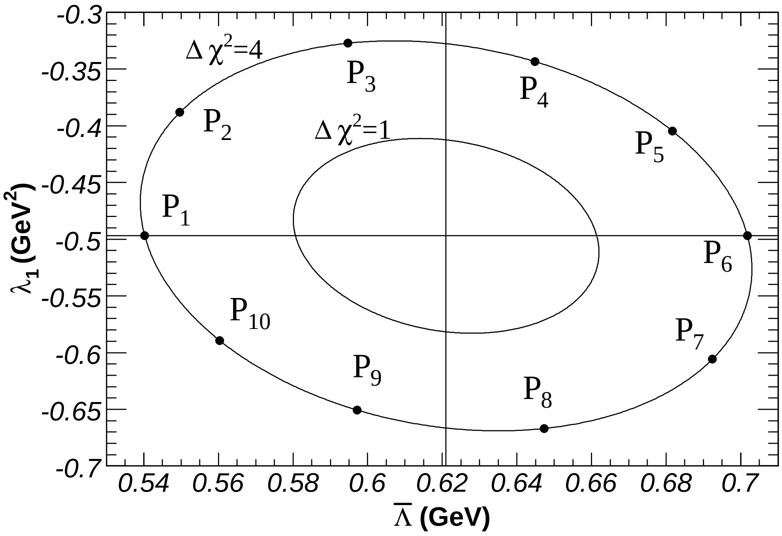

Figure 7.1: $\chi^2 = 1$ and $\chi^2 = 4$ error ellipses of the HQE parameters $\overline{\Lambda} = (0.621 \pm 0.041)$ GeV and $\lambda_1 = (-0497 \pm 0.086)\,\mathrm{GeV}^2$ with correlation of -0.17. The set of discrete points $P_1, \ldots, P_{10}$ is defined to estimate the uncertainty due to the SF parameters a and m_b.

error ellipse (see Figure 7.1) of the HQE parameters. For each point on the ellipse a new hybrid model is computed using as input the parameters a and m_b listed in Table 7.1.
The largest deviation observed on the extraction of $\Delta\mathcal{B}$ are observed using SF parameters $P_3 = \{a, m_b\} = \{2.63, 4.63\,\mathrm{GeV}/c^2\}$. From this deviation the systematic uncertainty on $\Delta\mathcal{B}$ is evaluated to be 0.3% and is defined as SF parameter uncertainty. As expected, this uncertainty is small due to the characteristic of the unfolding procedure even though f_u varies by $+12.5\%$ for P_6 or by -13.2% for P_1 (see Table 7.3).

The uncertainty due to the hybridization of the signal simulation is estimated by a comparison of the results of partial branching fraction extracted using signal Monte Carlo simulation which contains only the non-resonant $B \to X_u e \overline{\nu}_e$ decays and signal simulation which is based on the nominal hybrid model, where the resonant and non-resonant are mixed as described in section 4.3.1.
The overall systematic uncertainty on $\Delta\mathcal{B}$ due to the $B \to X_u e \overline{\nu}_e$ simulation is 2.54% with dominant contribution from hybridization error.

7.3 Background simulation

The $B\bar{B}$ background in this analysis has been estimated from MC simulation. To reflect the most recent measurements from various experiments the coresponding branching fractions, form factor parameters, and if needed also the underlying decay models (e.g.: for $B \to D\ell\nu$ and $B \to D^*\ell\nu$ decays) are varied in the MC simulation.
Tables 4.5 and 7.4 give an overview of branching fractions for the relevant decay modes

Table 7.1: Definition of the points on the $\chi^2 = 4$ ellipse (see Figure 7.1) for HQE parameters $\overline{\Lambda}$ and λ_1 and corresponding values for the SF parameters a and m_b.

Ellipse Point	$\overline{\Lambda}[\mathrm{GeV}]$	$\lambda_1[\mathrm{GeV}^2]$	$m_b[\mathrm{GeV}/c^2]$	a
central value	0.621	-0.497	4.658	1.328
P_1	0.702	-0.497	4.577	1.973
P_2	0.682	-0.405	4.597	2.446
P_3	0.645	-0.343	4.634	2.633
P_4	0.595	-0.327	4.684	2.244
P_5	0.550	-0.388	4.729	1.334
P_6	0.540	-0.497	4.739	0.761
P_7	0.560	-0.589	4.719	0.598
P_8	0.597	-0.651	4.682	0.644
P_9	0.647	-0.667	4.632	0.885
P_{10}	0.692	-0.606	4.587	1.374

used in the nominal simulation (SP8) and obtained from the world average [34] or from measurements performed at BABAR.

To evaluate the systematic uncertainties on $\Delta\mathcal{B}$ an alternative $\Delta\mathcal{B}'$ has been calculated where the following procedure has been applied. The number of background events has been varied according to the uncertainties of the branching fractions listed in the Tables 4.5 and 7.4. In reweighting the exclusive $B \to De\nu_e$, $B \to D^*e\nu_e$, and $B \to D^{**}e\nu$ with $D^{**} \equiv D_1/D_2^*$ channels the overall $\mathcal{B}(B \to X_c l\nu)$ is kept constant by modifying the branching fraction of all other decays. In the case of $B \to D^{**}e\nu$ decays with $D^{**} \equiv D_0^*/D_1'$ only the non-resonant $B \to Dn(\pi)e\nu$ branching fraction was modified, where the total $\mathcal{B}(B \to X_c l\nu)$ is kept constant. This method for evaluation of systematic uncertainties due to the branching fraction variation of $B \to X_c l\nu$ sub-modes was suggested by the BABAR semileptonic working group [54].
In addition to the branching fraction variation of the $B \to D\ell\nu$ and $B \to D^*\ell\nu$ decays, the uncertainties of corresponding form factor parameters have been taken into account.

The studies such as [55] have shown that the most realistic description of the dynamics of exclusive semileptonic decays is provided by the HQET [14, 15]. To reflect the most recent measurements [38] of $B \to D\ell\nu$ decays the model in the Monte Carlo simulation for this decay mode has been changed from ISGW2 [13] to HQET [14,15] using the CLN [16] parametrization (a short overview of the relationship between ISGW2 and HQET model is given in section 2.2.1). For this purpose the corresponding weights are calculated for the form factor parameter $\rho_D^2 = 1.22 \pm 0.08$ [38] and applied in the simulation on an event-by-event basis. Thus, the differential decays rate as well as the shape of the lepton spectra of $B \to D\ell\nu$ decays are modified. The corresponding weight distribution for the nominal Monte Carlo is shown in Figure 7.2. The uncertainty on $\Delta\mathcal{B}$ due to the $B \to D\ell\nu$ form factor parameter is evaluated by varying ρ_D^2 within its errors.
The theoretical framework with respect to the dynamics of $B \to D^*\ell\nu$ decays is given in section 2.2.1. The three free form factor parameters $\rho_{D^*}^2$, R_1 and R_2 are measured from experiments. The errors on these parameters are also sources of systematic uncertainties

Table 7.2: Systematic uncertainties due to exclusive $B \to X_u l \nu$ branching fractions variation in signal Monte Carlo simulation. Up and down arrows (↑↓) indicate the branching fraction variation within $\pm\sigma$. The total uncertainty on $\Delta\mathcal{B}$ has been computed as quadratic sum of the largest error of each systematic source.

Source of Systematics	f_u^{Hyb}	$\varepsilon_{sig} \times 10^{-3}$	$\varepsilon_{\overline{sig}} \times 10^{-3}$	$\Delta\mathcal{B} \times 10^{-4}$	$\sigma(\Delta\mathcal{B})[\%]$
Nominal	0.152	17.347	0.295	3.330	0.000
$\mathcal{B}(B \to \pi l \nu) \uparrow$	0.152	17.364	0.294	3.327	-0.073
$\mathcal{B}(B \to \pi l \nu) \downarrow$	0.152	17.331	0.295	3.332	0.074
$\mathcal{B}(B \to \rho l \nu) \uparrow$	0.152	17.201	0.294	3.359	0.894
$\mathcal{B}(B \to \rho l \nu) \downarrow$	0.152	17.495	0.296	3.300	-0.881
$\mathcal{B}(B \to \omega l \nu) \uparrow$	0.152	17.412	0.294	3.319	-0.312
$\mathcal{B}(B \to \omega l \nu) \downarrow$	0.152	17.282	0.296	3.340	0.314
$\mathcal{B}(B \to \eta l \nu) \uparrow$	0.152	17.242	0.295	3.349	0.594
$\mathcal{B}(B \to \eta l \nu) \downarrow$	0.152	17.453	0.295	3.310	-0.586
$\mathcal{B}(B \to \eta^{'} l \nu) \uparrow$	0.152	17.308	0.295	3.336	0.199
$\mathcal{B}(B \to \eta^{'} l \nu) \downarrow$	0.152	17.386	0.295	3.323	-0.198
non resonant only	0.151	16.886	0.308	3.394	1.940
Total BF					± 2.521

for the $B \to D^* \ell \nu$ decays.

To evaluate the systematic uncertainties for the $B \to D^* \ell \nu$ form factor parameters $\rho^2_{D^*}$, R_1 and R_2 one needs to take into account also their correlation. For this purpose, one has to diagonalize the error matrix M_{err} using the following transformation: $\rho^2_{D^*} \to \rho^{'2}_{D^*}$, $R_1 \to R^{'}_1$ and $R_2 \to R^{'}_2$, where $\rho^{'2}_{D^*}$, $R^{'}_1$, and $R^{'}_2$ are the uncorrelated form factor parameters. The new error matrix $M^{'}_{err}$ has the form:

$$M_{err} = \begin{pmatrix} \sigma^2_{\rho^2_{D^*}} & a & b \\ a & \sigma^2_{R_1} & c \\ b & c & \sigma^2_{R_2} \end{pmatrix} \to M^{'}_{err} = \begin{pmatrix} \sigma^2_{\rho^{'2}_{D^*}} & 0 & 0 \\ 0 & \sigma^2_{R^{'}_1} & 0 \\ 0 & 0 & \sigma^2_{R^{'}_2} \end{pmatrix}, \tag{7.2}$$

where the corresponding parameters are defined as

$$a = \sigma_{\rho^2_{D^*}} \sigma_{R_1} corr(\rho^2_{D^*}, R_1), \quad b = \sigma_{\rho^2_{D^*}} \sigma_{R_2} corr(\rho^2_{D^*}, R_2), \quad c = \sigma_{R_1} \sigma_{R_2} corr(R_1, R_2).$$

The values

$$\rho^2_{D^*} = 1.191 \pm 0.056, \qquad R_1 = 1.429 \pm 0.075, \qquad R_2 = 0.827 \pm 0.044$$

and their correlation coefficients

$$corr(\rho^2_{D^*}, R_1) = +0.71, \qquad corr(\rho^2_{D^*}, R_2) = -0.83, \qquad corr(R_1, R_2) = -0.84$$

are provided by the most recent BABAR measurement [56].

The roots of the characteristic polynomial are the eigenvalues $\lambda_1 = 92.21 \times 10^{-4}$, $\lambda_2 =$

Table 7.3: Summary of of systematics due to uncertainties on the Shape Function parameters a and m_b. Definition of the points $P_1, \ldots, P_{10}$ is given in Table 7.1 und in Figure 7.1. The maximum deviation observed for point P_3 is defined as the total SF uncertainty on $\Delta\mathcal{B}$.

Source of Systematics	f_u^{Hyb}	$\varepsilon_{sig} \times 10^{-3}$	$\varepsilon_{\overline{sig}} \times 10^{-3}$	$\Delta\mathcal{B} \times 10^{-4}$	$\sigma(\Delta\mathcal{B})[\%]$
Nominal	0.152	17.347	0.295	3.330	0.000
P_1	0.132	17.287	0.275	3.335	0.166
P_2	0.134	17.262	0.284	3.338	0.252
P_3	0.141	17.259	0.296	3.340	0.305
P_4	0.153	17.313	0.310	3.333	0.111
P_5	0.167	17.353	0.317	3.330	0.007
P_6	0.171	17.330	0.314	3.337	0.223
P_7	0.168	17.318	0.308	3.339	0.289
P_8	0.161	17.347	0.297	3.333	0.089
P_9	0.150	17.342	0.284	3.332	0.079
P_{10}	0.138	17.315	0.275	3.332	0.081
Total SF					± 0.305

11.66×10^{-4} and $\lambda_3 = 2.86 \times 10^{-4}$. The corresponding diagonal matrix M'_{err} is given by

$$M'_{err} = \begin{pmatrix} \sigma'^2_{\rho^2_{D^*}} & 0 & 0 \\ 0 & \sigma'^2_{R_1} & 0 \\ 0 & 0 & \sigma'^2_{R_2} \end{pmatrix} = \begin{pmatrix} \lambda_1 & 0 & 0 \\ 0 & \lambda_2 & 0 \\ 0 & 0 & \lambda_3 \end{pmatrix} = 10^{-4} \times \begin{pmatrix} 92.21 & 0 & 0 \\ 0 & 11.66 & 0 \\ 0 & 0 & 2.86 \end{pmatrix} \quad (7.3)$$

The variation of the independent parameters $\rho'^2_{D^*}$, R'_1 and R'_2 given by $\pm\sqrt{\lambda_{1,2,3}}$ respectively is used to estimate the uncertainties on $\Delta\mathcal{B}$. The corresponding systematic uncertainties are listed in table 7.5.

In this analysis, the signal extraction is very sensitive to the branching fraction variation of inclusive D decays where the dominant contribution to the $B\bar{B}$ background simulation systematics arises from the modeling of inclusive $D^0 \to K^0 X$ decays (see table 7.6). Although the branching fraction variation of this decay mode affects only slightly the variation of the total number of $B\bar{B}$ background events in the signal region, $\pm\Delta N^{MC}_{bkg} = 0.9\%$, the corresponding systematic uncertainty on $\Delta\mathcal{B}$ results in 2.8%. The reason is that the composition of $B \to X_c e \overline{\nu}_e$ sub-modes (e. g. $B \to D\ell\nu$ or $B \to D^*\ell\nu$) in the signal and sideband regions are different. Since the $D^0 \to K^0 X$ decays are sub-modes of $B \to D^{(*,**)} l\nu$ decays, the variation of $D^0 \to K^0 X$ branching fraction results in a bias of correction factor F^{corr}_{SB} (see section 6.1). In fact, the signal extraction procedure has no handle on the modeling of charm meson decays. The total $B \to X_c l\nu$ (table 7.5) and $D \to X$ (table 7.6) uncertainties on $\Delta\mathcal{B}$ have been computed as the quadratic sum of the absolute values corresponding to the largest error of each systematic source.

Table 7.4: Summary of branching fractions of inclusive D decay modes. The nominal (SP8) branching fractions in simulation are reweighted to the most recent world average results [53]

Decay mode	$\mathcal{B}_{SP8} \times 10^{-2}$	$\mathcal{B}_{new} \times 10^{-2}$
$D^0 \to K^0 X$	41	47 ± 4
$D^+ \to K^0 X$	68	61 ± 5
$D_s^+ \to K^0 X$	39	39 ± 28
$D^0 \to lX$	8.0	6.6 ± 0.2
$D^+ \to lX$	18.0	16.0 ± 0.4
$D_s^+ \to lX$	10	8 ± 6

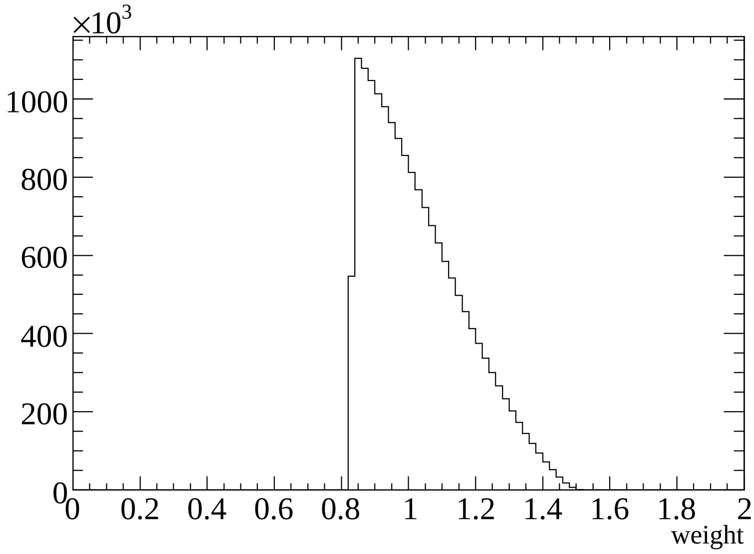

Figure 7.2: Distribution of form factor weight for $B \to D\ell\nu$ decays.

7.4 Detector Simulation

7.4.1 Track selection efficiency

To estimate the influence of the tracking efficiency in this analysis the recipe provided by the BABAR tracking group [57] was applied. In this context the differences between Monte Carlo simulation and data have been studied using the control samples $e^+e^- \to \tau^+\tau^-$ [58] and $D^* \to D^0\pi, D^0 \to K\pi$ [59]. The ratio of efficiencies $\varepsilon^{MC}/\varepsilon^{data}$ for the tracks with transverse momentum $|P_t| > 0.180\,\mathrm{MeV}/c$ has been measured for all run periods separately. The difference ($R = \varepsilon^{MC}/\varepsilon^{data} - 1$) in the track selection efficiency is given as 0.3% with an uncertainty σ_R of about 0.1%. There is no tracking efficiency correction. Instead, the data/MC difference in track reconstruction efficiency is taken as a source of systematic uncertainty. As such, the systematic uncertainty is evaluated by removing tracks randomly

Table 7.5: Summary of the systematic uncertainties due to the $B \to X_c l \nu$ background modeling. Up and down arrows (↑↓) indicate the branching fraction and form factors variation within $\pm\sigma$. $\rho'^2_{D^*}$, R'_1, and R'_2 are uncorelated $B \to D^* \ell \nu$ form factor parameters. The total $B \to X_c l \nu$ uncertainty on $\Delta\mathcal{B}$ has been computed as quadratic sum of the absolute values corresponding to largest error of each systematc source.

Source of Systematics	$\varepsilon_u \times 10^{-3}$	$F^{corr}_{D^0 e\nu}$	N^{MC}_{bkg}	F^{corr}_{SB}	$\Delta\mathcal{B} \times 10^{-4}$	$\sigma(\Delta\mathcal{B})[\%]$
Nominal	2.865	0.995	7535	0.987	3.330	-
$B \to D\ell\nu \uparrow$	2.865	0.998	7536	0.984	3.328	-0.045
$B \to D\ell\nu \downarrow$	2.865	0.991	7533	0.989	3.331	0.038
$B \to D^*\ell\nu \uparrow$	2.865	0.986	7670	0.974	3.337	0.223
$B \to D^*\ell\nu \downarrow$	2.865	1.000	7351	1.010	3.319	-0.319
$B \to D^{**}\ell\nu(narrow) \uparrow$	2.865	0.998	7397	1.000	3.339	0.281
$B \to D^{**}\ell\nu(narrow) \downarrow$	2.865	0.991	7672	0.972	3.329	-0.034
$B \to D^{**}\ell\nu(broad) \uparrow$	2.865	0.992	7539	0.984	3.348	0.543
$B \to D^{**}\ell\nu(broad) \downarrow$	2.865	0.996	7526	0.991	3.310	-0.579
$B \to X_c l\nu \uparrow$	2.865	0.994	7648	0.972	3.330	0.014
$B \to X_c l\nu \downarrow$	2.865	0.995	7421	1.002	3.329	-0.014
$\rho^2_D \uparrow$	2.865	0.995	7551	0.988	3.316	-0.416
$\rho^2_D \downarrow$	2.865	0.994	7519	0.986	3.342	0.382
$\rho'^2_{D*} \uparrow$	2.865	1.011	7301	1.016	3.286	-1.317
$\rho'^2_{D*} \downarrow$	2.865	0.979	7780	0.958	3.371	1.254
$R'_1 \uparrow$	2.865	0.994	7535	0.988	3.324	-0.175
$R'_1 \downarrow$	2.865	0.995	7533	0.985	3.335	0.166
$R'_2 \uparrow$	2.865	0.993	7553	0.986	3.328	-0.055
$R'_2 \downarrow$	2.865	0.996	7517	0.987	3.331	0.055
Total $B \to X_c l\nu$						± 1.527

in the simulation with a probability calculated as $P = \sqrt{R^2 + \sigma_R^2}$ depending on the run period. In addition, the low p_t tracks ($|P_t| < 0.180\,\mathrm{MeV}/c$) are also removed randomly from the simulation with a probability of 3.05% obtained from the slow pion study [59].

These changes on the tracking efficiency (both for low and high p_t tracks) result in a systematic uncertainty of $\sigma(\Delta\mathcal{B}) = -2.4\%$. The systematic uncertainty is assumed to be symmetric, since it is not possible to add additional tracks in the Monte Carlo simulation.

Since the difference in the track selection efficiency between data and simulation also affects the K^0_S reconstruction, an additional systematic uncertainty has to be quoted. For this purpose the K^0_S candidates were removed randomly from simulation with a probability of 1.7% as suggested by the BABAR tracking group [57]. The effect on the extracted $\Delta\mathcal{B}$ is very small, as shown in table 7.7.

Table 7.6: Summary of the systematics due to charm uncertainties in background modeling. Up and down arrows (↑↓) indicate the branching fraction variation within $\pm\sigma$. The total $D \to X$ uncertainty on $\Delta\mathcal{B}$ has been computed as quadratic sum of the largest error of each systematc source.

Source of Systematics	$\varepsilon_u \times 10^{-3}$	$F^{corr}_{D^0 ev}$	N^{MC}_{bkg}	F^{corr}_{SB}	$\Delta\mathcal{B} \times 10^{-4}$	$\sigma(\Delta\mathcal{B})[\%]$
Nominal	2.865	0.995	7535	0.987	3.330	-
$D^0 \to K^0 X \uparrow$	2.829	1.003	7468	1.020	3.238	-2.759
$D^0 \to K^0 X \downarrow$	2.901	0.986	7599	0.955	3.419	2.674
$D^+ \to K^0 X \uparrow$	2.832	0.998	7465	1.005	3.315	-0.449
$D^+ \to K^0 X \downarrow$	2.897	0.991	7604	0.969	3.345	0.462
$D_s^+ \to K^0 X \uparrow$	2.782	1.009	7349	1.018	3.351	0.639
$D_s^+ \to K^0 X \downarrow$	2.948	0.981	7722	0.957	3.307	-0.666
$D^0 \to lX \uparrow$	2.860	0.995	7524	0.991	3.321	-0.273
$D^0 \to lX \downarrow$	2.870	0.994	7545	0.983	3.339	0.271
$D^+ \to lX \uparrow$	2.858	0.995	7515	0.990	3.330	0.025
$D^+ \to lX \downarrow$	2.872	0.994	7554	0.983	3.329	-0.025
$D_s^+ \to lX \uparrow$	2.822	1.003	7447	1.002	3.337	0.233
$D_s^+ \to lX \downarrow$	2.901	0.988	7608	0.974	3.323	-0.205
Total $D \to X$						$\pm$2.896

7.4.2 Neutrals selection efficiency

As in the case of charged tracks there are also differences in the photon selection efficiency between data and the simulation. According to the study of the π^0 efficiency in τ decays [60] there is no efficiency correction necessary to single photons, however a systematic error of 1.8% needs to be taken into account. For this purpose, 1.8% of the photons are randomly removed from simulation and a new $\Delta\mathcal{B}$ was calculated. The resulting uncertainty is presented in table 7.7.

As described in section 4.6 the slow neutral pions are used in the partial reconstruction of $B \to D^* \ell \nu$ decays. The reconstruction efficiency for π^0 mesons, $\varepsilon^{MC}_{\pi^0}$, depends on the π^0 momentum and is known with an uncertainty of 3% [60]. To correct $\varepsilon^{MC}_{\pi^0}$ the π^0 candidates have been randomly removed from simulation with a probability given by

$$P^{\pi^0}_{kill} = a + b \cdot |P_{\pi^0}|, \tag{7.4}$$

where the parameters $a = 0.95970$ and $b = 0.00764$ have been taken from the π^0 efficiency study [60] and P_{π^0} is the measured π^0 three-momentum in the laboratory frame. To estimate the systematic uncertainty due to π^0 efficiency the "killing" probability $P^{\pi^0}_{kill}$ has been varied by 3% and the analysis was repeated. The result is listed in table 7.7.

7.4.3 Particle identification

To identify charged leptons, kaons and protons the corresponding PID (Particle Identification) selectors described in section 4.4.5 are used. Each selector is characterized by

Table 7.7: Systematic effects due to uncertainties in the modeling of the detector performance. The arrows ↑↓ indicate additional or less detector material in the simulation for bremsstrahlung modeling. The total experimental uncertainty on $\Delta\mathcal{B}$ has been computed as the quadratic sum of the errors of each systematc source. In the case of bremsstrahlung systematic the absolute largest uncertainty is added in quadrature.

Source of Systematics	$\varepsilon_u \times 10^{-3}$	$F^{corr}_{D^0 e\nu}$	N^{MC}_{bkg}	F^{corr}_{SB}	$\Delta\mathcal{B} \times 10^{-4}$	$\sigma(\Delta\mathcal{B})[\%]$
Nominal	2.865	0.995	7535	0.987	3.330	-
Bremsstrahlung ↑	2.853	0.997	7509	0.990	3.338	0.247
Bremsstrahlung ↓	2.876	0.993	7554	0.984	3.323	-0.190
Tracking	2.800	1.014	7468	1.017	3.248	-2.447
Neutrals	2.793	1.015	7409	1.027	3.244	-2.572
slow π^0	2.891	0.994	7687	0.970	3.289	-1.234
K_L^0 efficiency	2.857	0.997	7542	0.992	3.300	-0.895
K_L^0 energy	2.856	0.996	7537	0.992	3.309	-0.630
Electron ID	2.800	0.991	7434	1.010	3.373	1.293
$\pi^\pm$ fake-rate	2.863	0.992	7545	0.987	3.334	0.137
$K^\pm$ fake-rate	2.862	0.992	7543	0.987	3.336	0.203
$p^\pm$ fake-rate	2.863	0.992	7545	0.987	3.334	0.143
Kaon ID	2.859	0.996	7504	0.990	3.335	0.171
$\pi^\pm$ fake-rate	2.846	0.995	7471	0.993	3.359	0.885
$p^\pm$ fake-rate	2.865	0.992	7554	0.986	3.330	0.019
$\mu^\pm$ fake-rate	2.865	0.993	7534	0.987	3.333	0.094
Muon ID	2.888	0.987	7677	0.981	3.273	-1.708
Proton ID	2.864	0.995	7534	0.987	3.330	0.010
K_S efficiency	2.862	0.995	7530	0.988	3.328	-0.053
Λ efficiency	2.868	0.996	7543	0.984	3.332	0.067
J/ψ efficiency	2.867	0.998	7544	0.984	3.319	-0.313
conv. γ efficiency	2.861	0.995	7515	0.990	3.329	-0.033
Total Exp						±4.671

the efficiency to reconstruct a true lepton, kaon or proton and by their mis-identification (misID) efficiency. These efficiencies and fake rates are evaluated on control samples by the BABAR PID working group [61]. Since these efficiencies differ between data and simulation the particle identification procedure can lead to possible systematic uncertainties. To reduce the sensitivity on the efficiency differences between data and simulation, the so-called PID tweaking method, was applied. For this purpose, the particles in the simulation for each selector are added or removed based on the probability given as ratio $\varepsilon_{DATA}/\varepsilon_{MC}$, where ε_{DATA} and ε_{MC} are reconstruction efficiency for data and simulation, respectively. To evaluate the systematic uncertainty due to particle identification the PID tweaking probability is modified within its uncertainties and the analysis was repeated. The corresponding uncertainties on $\Delta\mathcal{B}$ are listed in table 7.7.

The dominant uncertainty was obtained for the muon ID mostly affected by the cut on the total number of leptons in the event.

To evaluate the uncertainties due to the particle mis-identification (e. g. pions as electrons or pions as kaons) the rate for misID is modified according to the values obtained from the data-simulation comparison provided by PID working group [61]. For this purpose, the particles in the simulation for each selector are removed with a probabilty given as

$$P^{p}_{misID,k} = \frac{N_p \varepsilon^p_k}{N_k}, \tag{7.5}$$

where ε^p_k is the fake-rate efficiency for particle k to be identified as particle p, N_p is the identified number of particles for a given selector, and N_k the total number of particles produced in the momentum region of interest. The influence of particle mis-identification is negligible for the electron selector but contributes with uncertainty of 0.9% to the total PID systematic due to the kaon selection.

Since the number of muons and protons ($N_p : p \equiv \mu/p$) as well as the corresponding fake-rate efficiencie in this analysis are small ($< 5\%$) compared to the number of other charged tracks ($N_k : k \equiv \pi/K$), the uncertainties due to the particle mis-identification for corresponding selectors can be neglected ($P^{\mu/K}_{misID,\pi/K} < 0.0005$).

The results are shown in table 7.7.

7.4.4 Modeling of K^0_L Meson

The neutrals selection criteria described in section 4.4.3 is designed to suppress the selection of K^0_L mesons. Nevertheless, a non-negligible part of these mesons are identified as photons and thus are used for reconstruction of the visible energy. As a consequence, many variables e.g. $E_{\mathrm{miss}} - |P_{\mathrm{miss}}|$ or q^2 are sensitive to the reconstruction efficiency and the energy deposition of K^0_L candidates in the EMC. The differences between data and the simulation concernig the reconstruction efficiency and the energy deposition of K^0_L have been studied in [62] using $D^0 \to K^0_L \pi^+\pi^-$ and $D^0 \to K^0_S \pi^+\pi^-$ control samples. This study provides a tool, which is used in this analysis to adjust the simulation.

To correct the reconstruction efficiency in the simulation, the K^0_L candidates are randomly removed from the neutral list with a probability depending on the true K^0_L momentum. The overall efficiency correction is -18%. The energy deposition in the EMC for detected K^0_L candidates has been modified according to the weights computed in [62]. The reweighted energy deposition of the K^0_L candidates is by $\sim 17\%$ higher compared to the nominal Monte Carlo simulation.

The systematic uncertainties listed in table 7.7 are determined from variation of the efficiency correction and energy scaling factors within their statistical uncertainties.

7.4.5 Reconstruction of composite particles

As described in section 4.4.4 all charged tracks which are identified as daughters of the composite particles K_S, Λ, J/ψ, and conversion photons are removed from the charged track list. Since the reconstruction efficiency of these composite particles is different for data and simulation the corresponding systematic uncertainties are evaluated. Hence, the composite particle are removed randomly from the simulation with a probability which corresponds to the uncertainty of the reconstruction efficiency. The daughter tracks are kept if they satisfy the charged track selection criteria.

For the conversion photons ($\gamma \rightarrow e^+e^-$) the reconstruction efficiency in the simulation has been varied within 13% taken from study [63].
The studies of the J/ψ reconstruction performed in various BABAR analyses [64, 65] show good agreement between data and simulation but don't provide any unique numbers as in the case of K_S or conversion photons. Therefore, a 20% uncertainty on the J/ψ reconstruction efficiency has been assumed. This results in a 0.3% uncertainty on the $B \rightarrow X_u e \overline{\nu}_e$ partial branching fraction.
The systematic error due to the Λ reconstruction is negligible even if the reconstruction efficiency in the simulation has been varied by 50%.
The systematic evaluation for K_S candidates is described in section 7.4.1. The systematic uncertainties due to reconstruction of composite particles are shown in table 7.7.

7.4.6 Bremsstrahlung

To investigate the systematic effects due to the bremsstrahlung modeling in the detector simulation the electon energy spectra in the simulation are reweighted corresponding to the effects caused due to uncertainties in the detector geometry. From the Bhabha control sample study [66] the uncertainty on the amount of the detector material in simulation compared to reality does not exceed 0.14% of a radiation length X_0. As a consequence the systematic uncertainty on the measured partial branching fraction has been evaluated by comparison of results for nominal and for additional or less detector material in simulation. The method implemented in [67] and used in this analysis allows to reweight electron energy spectra independent from their shape according to scenarios of additional or less detector material. In addition, about 2.8% of all generated bremsstrahlung photons have to be killed to reflect the case of thinner detector material. The analysis is then repeated and all kinimatical variables are computed with respect to changes caused by the bremsstrahlung systematic. The systematic effects due to the bremsstrahlung are very small as shown in table 7.7.

7.4.7 Final state radiation

The effects of the final state radiation in Monte Carlo simulation are modeled by the PHOTOS package [68]. To estimate the systematic uncertainties, the procedure suggested by the semileptonic AWG [69] has been applied. For this purpose, the results obtained for partial branching fraction based on simulation using PHOTOS are compared with results where the PHOTOS is switched off. Since it was not possible to generate the full set of generic Monte Carlo events with PHOTOS "off" the nominal simulation with PHOTOS "on" has been accordingly reweighted using two dimensional weights calculated in bins of true lepton energy E_l and true q^2. The weights are computed by comparison of PHOTOS "on/off" distributions obtained from generator-level Monte Carlo simulation[2] for all relevant semileptonic B decay channels: $B \rightarrow D^{(*,**)} e\nu, D^{(*)} \pi e \nu$, and $X_u e \nu_e$. This reweighting procedure has been tested and found to be correct. Figures 7.3 and 7.4 show the true E_l,

---

[2] detector simulation not included

Table 7.8: Parameters which have been used for the Beam energy correction. ξ is a normalization correction factor obtained by comparing the integrals of the initial and reweighted $\Upsilon(4S)$ energy spectra.

Run	E_{data}[GeV]	E_{MC}[GeV]	ξ
1	10.57756	10.57730	0.99558
2	10.57869	10.57783	0.98757
3	10.57843	10.57773	0.99502
4	10.57771	10.57727	0.99363
5	10.57811	10.57670	0.98181
6	10.57960	10.57616	0.93990

q^2, and $s_{\mathrm{h}}^{\mathrm{max}}$ distributions for $B \to D\ell\nu$ and $B \to X_u l\nu$ decays, respectively.
The full deviation of the $\Delta\mathcal{B}$ for the PHOTOS "off" scenario compared to the nominal $\Delta\mathcal{B}$ value is -2.8%. The systematic uncertainty is estimated as 30%[3] of the observed difference and results in $\sigma(\Delta\mathcal{B}) = -0.8\%$. A more realistic evaluation of the uncertainty due to the radiative corrections would be the comparison between results based on PHOTOS on one hand and on an exact analytical calculation on the other hand. The corresponding package [70] which will provide such a calculation in the future is under development.

7.5 Beam energy correction

The inclusive electron energy spectrum in semileptonic B decays close to the kinematic endpoint is affected by the beam collision energy. The latter is used to dermine the B meson momentum which affects the kinematic of B meson decay. The difference between beam energies in data and simulation can result in a systematic uncertainty for the extracted partial branching fraction. To estimate these systematic effects the nominal simulation was corrected event-by-event using a weight function $F(E)$:

$$F(E) = \xi e^{-\frac{(E_{data}-E_{MC})(E_{data}+E_{MC}-2E)}{2\sigma_E^2}}, \tag{7.6}$$

where E is the true $\Upsilon(4S)$ center of mass (cms) energy, $E_{data/MC}$ is the average of cms energies in data and simulation, and σ_E is the cms energy spread of the produced $\Upsilon(4S)$ resonance. The values for $E_{data/MC}$ (see table 7.8) and $\sigma_E = 4.95\,\mathrm{MeV}$ are taken from the study performed in [71], where the differences between data and simulation are studied based on the momentum distributions of fully reconstructed B mesons. The normalization factor ξ (see table 7.8) has been evaluated in this analysis by comparing the integrals of the initial and reweighted $\Upsilon(4S)$ energy spectra. Table 7.8 gives an overview for the used parameters. The systematic uncertainty on $\Delta\mathcal{B}$ is assigned as 50% of the deviation of results with and without beam energy correction and is evaluated to be $\sigma(\Delta\mathcal{B}) = 0.4\%$.

---

[3] This number follows estimates of uncertainties on the theoretical calculations that went into PHOTOS.

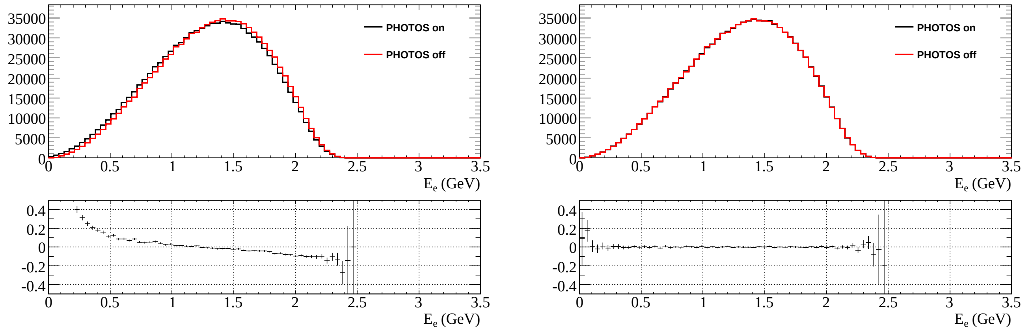

a) True E_e - distribution

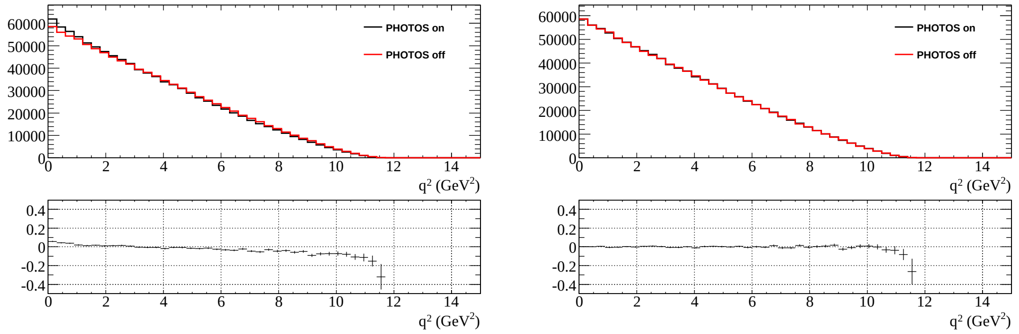

b) True q^2 - distribution

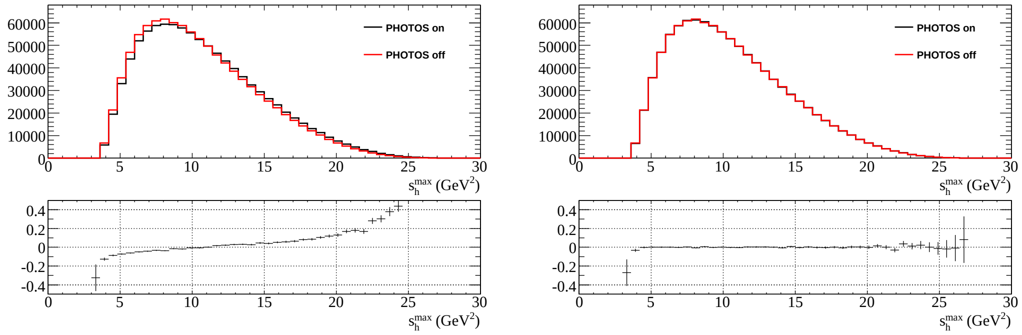

c) True $s_{\mathrm{h}}^{\mathrm{max}}$- distribution

Figure 7.3: Comparison of various true distrubutions of $B \to D\ell\nu$ decays for the PHOTOS on/off scenarios. The left plots show distributions without reweighting and on the right side plots are shown where PHOTOS on distribution are reweighted to match the PHOTOS off scenario. Some points in histograms (e. g. for $s_{\mathrm{h}}^{\mathrm{max}} \approx 3.5\,\mathrm{GeV}^2$) are affected by histogram binning.

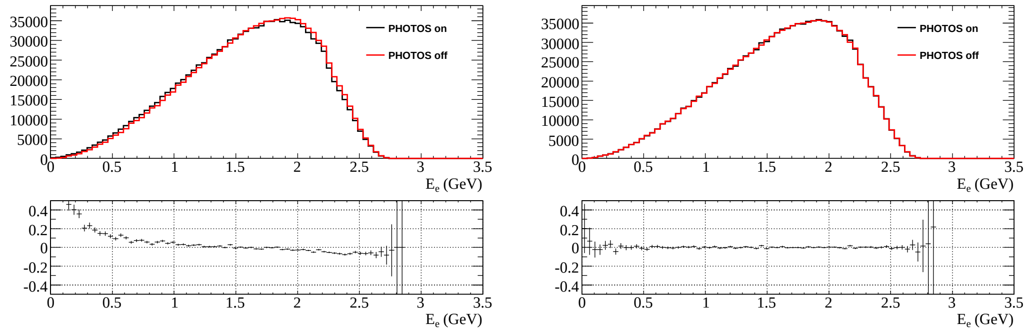

a) True E_e - distribution

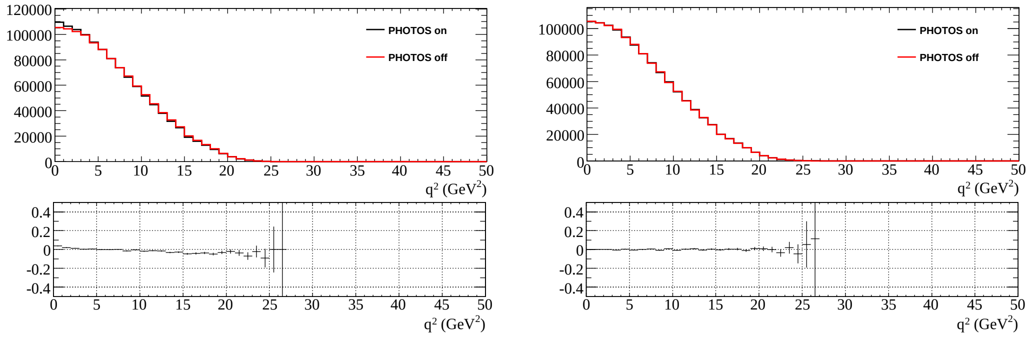

b) True q^2 - distribution

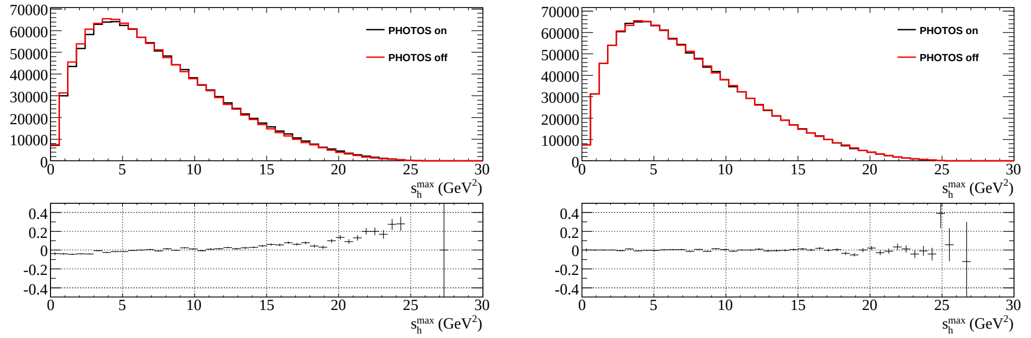

c) True $s_{\rm h}^{\rm max}$- distribution

Figure 7.4: Comparison of various true distrubutions of $B \to X_u l \nu$ decays for the PHOTOS on/off scenarios. The left plots show the distribution without reweighting and on the right side plots are shown where PHOTOS on distribution are reweighted to match the PHOTOS off scenario.

7.6 *B*-meson counting

The extraction of the partial branching fraction (see equation 6.5) requires the knowledge of the number of $B\bar{B}$ pairs produced in 413 fb^{-1} onpeak data. Accordind to [72] the evaluated number of $B\bar{B}$ pairs used in this analysis is $N_{BB} = (454.21 \pm 5.00) \times 10^6$ which results in 1.1% of the systematic uncertainty for the partial branching fraction $\Delta\mathcal{B}$.

7.7 Summary of systematic uncertainties

A summary of all systematic uncertainties studied are shown in table 7.9. The largest systematic error is due to the detector modeling with ±4.7% followed by the uncertainty due to the background simulation with ±3.4% and due to the signal simulation with ±2.5%. The total systematic uncertainty calculated as the sum of quadrature of all evaluated systematics is ±6.3%:

$$\sigma(\Delta\mathcal{B}) = \pm 4.7\%_{\mathrm{det}} \pm 3.4\%_{\mathrm{bkg}} \pm 2.5\%_{\mathrm{sig}} = \pm 6.3\%_{\mathrm{tot}}.$$

To emphasize the achievements of this analysis the evaluated systematic uncertainty are compared with uncertainties obtained in the previous analysis [1] (last column in table 7.9) and with uncertainties from this analysis without using the advanced analytical technique of the partial $B \to D^* \ell \nu$ veto. In addition, the uncertainties have been evaluated also for different requirements on the electron energy and the $s_{\mathrm{h}}^{\mathrm{max}}$, as shown in table 7.10 and 7.11.

Table 7.9: Summary of systematic uncertainties for $E_e > 2.0\,\mathrm{GeV}$. The total systematic uncertainty was computed as the quadratic sum of the detector modeling, background and signal simulation uncertainties.

Source of Systematics	$\sigma(\Delta\mathcal{B})[\%]$	$\sigma(\Delta\mathcal{B})[\%]$ (without $B \to D^*\ell\nu$ veto)	$\sigma(\Delta\mathcal{B})[\%]$ (previous analysis [73])
Track selection efficiency	2.4	4.9	2.2
Photon selection efficiency	2.6	6.6	6.4
Electron ID	1.3	1.7	1.1
Muon ID	1.7	2.1	-
Hadron ID	0.9	1.3	2.6
Bremsstrahlung	0.2	0.3	2.9
K_L^0 efficiency	0.9	1.9	-
K_L^0 energy deposition	0.6	1.5	4.3
Slow π^0 efficiency	1.2	-	-
Composites efficiency	0.3	0.8	-
Beam energy correction	0.4	1.1	-
B counting	1.1	1.1	1.1
Total detector modeling	4.7	9.2	9.1
$B \to X_c l\nu$ simulation	1.5	1.5	7.4
Inclusive D decays	2.9	6.2	-
Final State Radiation	0.8	1.4	5.1
Total background simulation	3.4	6.6	9.0
$B \to X_u l\nu$ simulation	2.5	2.5	4.4
SF parameter uncertainties	0.3	0.5	1.1
Total signal simulation	2.5	2.5	4.5
TOTAL	6.3	11.7	13.6

Table 7.10: Summary of systematic uncertainties for different requirements on lepton energy for $s_{\mathrm{h}}^{\mathrm{max}} < 3.52\,\mathrm{GeV}^2$. The total systematic uncertainty was computed as the quadratic sum of the detector modeling, background and signal simulation uncertainties.

Source of Systematics	$\sigma(\Delta\mathcal{B})[\%]$ $E_e > 1.7\,\mathrm{GeV}$	$\sigma(\Delta\mathcal{B})[\%]$ $E_e > 1.8\,\mathrm{GeV}$	$\sigma(\Delta\mathcal{B})[\%]$ $E_e > 1.9\,\mathrm{GeV}$	$\sigma(\Delta\mathcal{B})[\%]$ $E_e > 2.0\,\mathrm{GeV}$	$\sigma(\Delta\mathcal{B})[\%]$ $E_e > 2.1\,\mathrm{GeV}$	$E_e > 2.2\,\mathrm{GeV}$
Track selection efficiency	5.0	4.3	3.6	2.4	1.2	0.3
Photon selection efficiency	5.0	4.3	4.0	2.6	1.8	1.5
Electron ID	0.7	0.4	0.7	1.3	2.0	2.8
Muon ID	3.5	2.8	2.3	1.7	0.9	0.4
Hadron ID	1.0	1.0	0.9	0.9	1.3	0.8
Bremsstrahlung	0.5	0.4	0.3	0.2	0.2	0.3
K_L^0 efficiency	1.7	1.5	1.3	0.9	0.6	0.2
K_L^0 energy deposition	1.4	1.3	0.9	0.6	0.2	0.0
Slow π^0 efficiency	0.8	0.9	1.3	1.2	1.6	1.8
Composites efficiency	0.5	0.5	0.4	0.3	0.4	0.5
Beam energy correction	0.3	0.2	0.2	0.4	0.4	0.1
B counting	1.1	1.1	1.1	1.1	1.1	1.1
Total detector modeling	8.4	7.2	6.3	4.7	3.9	3.9
$B \to X_c l \nu$ simulation	1.6	1.4	1.5	1.5	1.6	1.7
Inclusive D decays	4.7	4.4	3.8	2.9	2.4	1.4
Final State Radiation	2.3	1.7	1.1	0.8	0.7	0.6
Total background simulation	5.3	4.9	4.3	3.4	3.0	2.3
$B \to X_u l \nu$ simulation	2.7	2.8	2.6	2.5	2.5	2.4
Shape Function uncertainties	1.2	0.9	0.7	0.3	0.4	0.8
Total signal simulation	3.0	3.0	2.7	2.5	2.5	2.6
TOTAL	10.3	9.2	8.1	6.3	5.5	5.2

Table 7.11: Summary of systematic uncertainties for different requirements on lepton energy for $s_{\mathrm{h}}^{\max} < 4.0\,\mathrm{GeV}^2$. The total systematic uncertainty was computed as the quadratic sum of the detector modeling, background and signal simulation uncertainties.

Source of Systematics	$\sigma(\Delta\mathcal{B})[\%]$ $E_e > 1.7\,\mathrm{GeV}$	$\sigma(\Delta\mathcal{B})[\%]$ $E_e > 1.8\,\mathrm{GeV}$	$\sigma(\Delta\mathcal{B})[\%]$ $E_e > 1.9\,\mathrm{GeV}$	$\sigma(\Delta\mathcal{B})[\%]$ $E_e > 2.0\,\mathrm{GeV}$	$\sigma(\Delta\mathcal{B})[\%]$ $E_e > 2.1\,\mathrm{GeV}$	$E_e > 2.2\,\mathrm{GeV}$
Track selection efficiency	5.8	5.1	4.2	3.3	1.8	0.5
Photon selection efficiency	6.5	5.4	5.3	3.6	3.1	2.1
Electron ID	0.6	0.3	0.5	1.7	2.5	2.6
Muon ID	3.8	3.1	2.6	1.9	1.0	0.4
Hadron ID	1.2	1.2	1.2	1.1	1.6	0.8
Bremsstrahlung	0.5	0.4	0.3	0.3	0.3	0.3
K_L^0 efficiency	1.7	1.5	1.2	0.8	0.6	0.2
K_L^0 energy deposition	1.4	1.2	0.7	0.5	0.1	0.1
Slow π^0 efficiency	0.9	0.9	1.4	1.5	1.8	2.1
Composites efficiency	0.7	0.6	0.5	0.4	0.5	0.6
Beam energy correction	0.5	0.6	0.5	0.5	0.7	0.1
B counting	1.1	1.1	1.1	1.1	1.1	1.1
Total detector modeling	10.0	8.5	7.7	6.0	5.3	4.3
$B \to X_c l \nu$ simulation	2.4	2.2	1.9	1.6	1.4	1.6
Inclusive D decays	5.7	5.3	4.8	3.6	3.1	1.5
Final State Radiation	2.7	2.3	1.6	1.2	1.1	0.7
Total background simulation	6.8	6.2	5.4	4.1	3.7	2.3
$B \to X_u l \nu$ simulation	2.6	2.7	2.4	2.5	2.5	2.3
Shape Function uncertainties	2.1	1.7	1.5	1.0	0.9	0.6
Total signal simulation	3.3	3.2	2.9	2.7	2.7	2.4
TOTAL	12.5	11.0	9.8	7.8	6.9	5.5

8 Results

8.1 Measurement of $\Delta\mathcal{B}(B \to X_u e\overline{\nu}_e)$

The partial branching fraction $\Delta\mathcal{B}(B \to X_u e\overline{\nu}_e)$ is extracted in the $E_e - s_\mathrm{h}^\mathrm{max}$ signal region using the procedure described in section 6.1. A summary of the input parameters used for the $\Delta\mathcal{B}(B \to X_u e\overline{\nu}_e)$ calculation is provided in Table 8.1. The values obtained for both data and Monte Carlo simulation are quoted for various requirements on the lepton energy for $s_\mathrm{h}^\mathrm{max} < 3.52\,\mathrm{GeV}^2$ and $s_\mathrm{h}^\mathrm{max} < 4.00\,\mathrm{GeV}^2$. Using equation (6.5), the systematic uncertainties summarized in Tables 7.10 and 7.11 as well as input parameters from Table 8.1, the inclusive $B \to X_u e\overline{\nu}_e$ partial branching fractions are measured. The values are listed in Table 8.2.

Using requirements $E_e > 2.0\,\mathrm{GeV}$ and $s_\mathrm{h}^\mathrm{max} < 3.52\,\mathrm{GeV}^2$ obtained from the optimization procedure (see section 4.8.3), the partial branching fraction is measured to be

$$\Delta\mathcal{B}(B \to X_u e\overline{\nu}_e) = (3.33 \pm 0.18_\mathrm{stat} \pm 0.21_\mathrm{syst}) \times 10^{-4}, \tag{8.1}$$

where the first error corresponds to the statistical and the second error to the systematic uncertainties. This result can not be compared directly to the $\Delta\mathcal{B}$ obtained in the previous analysis [1] because of a different rest frame used in the calculation of the unfolded partial branching fraction. In this analysis $\Delta\mathcal{B}$ was computed in $\Upsilon(4S)$ rest frame. As an alternative, the B meson rest fame can be used to extract the unfolded partial branching fraction, which was performed in previous analysis [1]. Since there is no possibility to convert the results obtained in this analysis from $\Upsilon(4S)$ to the B rest frame, this analysis was repeated for $E_e > 2.0\,\mathrm{GeV}$, $s_\mathrm{h}^\mathrm{max} < 3.52\,\mathrm{GeV}^2$ and the partial branching fraction is extracted using the target region defined in terms of the unsmeared kinematic variables $\tilde{E}_e$ and $\tilde{s}_\mathrm{h}^\mathrm{max}$ in the B meson rest frame. To be consistent with the previous analysis the target region is selected by requiring $\tilde{E}_e > 1.9\,\mathrm{GeV}$ and $\tilde{s}_\mathrm{h}^\mathrm{max} < 3.5\,\mathrm{GeV}^2$. The unfolded partial branching fraction is then evaluated to be

$$\Delta\tilde{\mathcal{B}}(B \to X_u e\overline{\nu}_e) = (4.57 \pm 0.24_\mathrm{stat} \pm 0.32_\mathrm{syst}) \times 10^{-4}, \tag{8.2}$$

which is in very good agreement with the result from previous analysis

$$\Delta\tilde{\mathcal{B}}'(B \to X_u e\overline{\nu}_e) = (4.51 \pm 0.41_\mathrm{stat} \pm 0.62_\mathrm{syst}) \times 10^{-4}. \tag{8.3}$$

Using different rest frames for the analysis cuts ($\Upsilon(4S)$) and for the definition of the target region (B meson), results in higher sensitivity to the Shape Function parameter uncertainty. As a consequence, the partial branching fraction was measured in B meson rest frame (8.2) with a Shape Function parameter uncertainty of 3.1% where the corresponding uncertainty of $\Delta\mathcal{B}$ in the $\Upsilon(4S)$ rest frame (8.2) is 0.3%, as shown in Table 7.10.

Table 8.1: Data and Monte Carlo yields and efficiencies used for computing the signal partial branching fraction for different requirements on lepton energy for $s_{\mathrm{h}}^{\mathrm{max}} < 3.52\,\mathrm{GeV}^2$ and $s_{\mathrm{h}}^{\mathrm{max}} < 4.00\,\mathrm{GeV}^2$. Note that the errors shown are purely statistical.

		lower bound on E_e in [GeV **]**					
		1.7	1.8	1.9	2.0	2.1	2.2
$s_{\mathrm{h}}^{\mathrm{max}} < 3.52\,\mathrm{GeV}^2$							
	$N_{\mathrm{cand}}^{\mathrm{data}}$	26311 ± 280	22712 ± 270	18184 ± 260	13149 ± 247	8376 ± 236	4815 ± 223
	$N_{\mathrm{bkg}}^{\mathrm{MC}}$	18712 ± 78	15458 ± 71	11588 ± 61	7535 ± 49	3890 ± 35	1398 ± 21
	F_{SB}^{corr}	0.989 ± 0.006	0.990 ± 0.008	0.997 ± 0.011	0.987 ± 0.018	1.035 ± 0.044	0.893 ± 0.186
	F_{Dlnu}^{corr}	1.035 ± 0.011	1.014 ± 0.013	0.995 ± 0.016	0.995 ± 0.016	0.995 ± 0.016	0.995 ± 0.016
	f_u	0.196 ± 0.000	0.186 ± 0.000	0.171 ± 0.000	0.152 ± 0.000	0.127 ± 0.000	0.096 ± 0.000
	$\varepsilon_{\mathrm{sig}}$	16.786 ± 0.115	17.004 ± 0.119	17.267 ± 0.125	17.347 ± 0.133	17.033 ± 0.145	16.630 ± 0.164
	$\varepsilon_{\overline{\mathrm{sig}}}$	0.538 ± 0.010	0.470 ± 0.009	0.385 ± 0.008	0.295 ± 0.007	0.212 ± 0.006	0.113 ± 0.004
$s_{\mathrm{h}}^{\mathrm{max}} < 4.00\,\mathrm{GeV}^2$							
	$N_{\mathrm{cand}}^{\mathrm{data}}$	39403 ± 317	33585 ± 304	26413 ± 289	18384 ± 272	11020 ± 255	5664 ± 239
	$N_{\mathrm{bkg}}^{\mathrm{MC}}$	30449 ± 99	25151 ± 90	18876 ± 78	12144 ± 63	6176 ± 45	2138 ± 26
	F_{SB}^{corr}	0.989 ± 0.006	0.990 ± 0.008	0.997 ± 0.011	0.987 ± 0.018	1.036 ± 0.044	0.893 ± 0.186
	F_{Dlnu}^{corr}	1.035 ± 0.011	1.014 ± 0.013	0.995 ± 0.016	0.995 ± 0.016	0.995 ± 0.016	0.995 ± 0.016
	f_u	0.232 ± 0.001	0.218 ± 0.001	0.198 ± 0.001	0.174 ± 0.000	0.142 ± 0.000	0.105 ± 0.000
	$\varepsilon_{\mathrm{sig}}$	16.590 ± 0.106	16.773 ± 0.109	16.986 ± 0.115	16.955 ± 0.123	16.547 ± 0.134	16.128 ± 0.154
	$\varepsilon_{\overline{\mathrm{sig}}}$	0.508 ± 0.010	0.430 ± 0.009	0.335 ± 0.008	0.248 ± 0.007	0.165 ± 0.005	0.080 ± 0.004

Table 8.2: Unfolded partial branching fraction results with statistical and systematical uncertainties for various requirements on lepton energy for $s_{\mathrm{h}}^{\mathrm{max}} < 3.52\,\mathrm{GeV}^2$ and $s_{\mathrm{h}}^{\mathrm{max}} < 4.00\,\mathrm{GeV}^2$.

		lower bound on E_e in [GeV]					
		1.7	1.8	1.9	2.0	2.1	2.2
$s_{\mathrm{h}}^{\mathrm{max}} < 3.52\,\mathrm{GeV}^2$							
	$\Delta\mathcal{B} \times 10^{-4}$	4.371	4.216	3.837	3.330	2.603	2.231
	Δ_{stat}	0.182	0.181	0.180	0.175	0.180	0.217
	Δ_{syst}	0.450	0.388	0.311	0.210	0.143	0.116
	Δ_{tot}	0.485	0.428	0.359	0.273	0.230	0.246
$s_{\mathrm{h}}^{\mathrm{max}} < 4.00\,\mathrm{GeV}^2$							
	$\Delta\mathcal{B} \times 10^{-4}$	5.413	5.148	4.588	3.908	2.918	2.473
	Δ_{stat}	0.231	0.230	0.230	0.225	0.241	0.309
	Δ_{syst}	0.677	0.566	0.450	0.358	0.270	0.136
	Δ_{tot}	0.715	0.611	0.505	0.423	0.362	0.338

8.2 Stability Studies

To test the stability of the extracted results, the measured partial branching fraction $\Delta\mathcal{B}(B \to X_u e \overline{\nu}_e)$ was extracted by varying the cuts in the refined selection. Figures from 8.1 to 8.3 show corresponding results for $\Delta\mathcal{B}$. In these Figures, the top plot shows the measured $\Delta\mathcal{B}$ values depending on the cut value, and the bottom plot displays the relative differences of these values with respect to the nominal measurement as $\Delta\mathcal{B}^i/\Delta\mathcal{B}^{\mathrm{nomi}} - 1$, where i denotes the given scan point.

The neural network output as well as the $cos\Theta_{\mathrm{miss}}$ scans show a very stable behavior. There is also no significant variation in the partial branching fraction as a function of $E_{\mathrm{miss}} - |P_{\mathrm{miss}}|$, however the nominal value is measured to be a little smaller compared to the other scan points.

The scan versus $cos\Theta_{\mathrm{e-T}}$ is sensitive to the continuum subtraction. Figure 8.3 displays the behavior of the partial branching fraction measurements as a function of the cut on $|cos\Theta_{\mathrm{e-T}}|$. The results for scan points above 0.8 tend to the smaller values compared to the nominal value at $|cos\Theta_{\mathrm{miss}}| \approx 0.6$. This behaviour can not be explained even the systematic uncertainties are included in the ploting of the $\Delta\mathcal{B}$ dependency on the $cos\Theta_{\mathrm{e-T}}$ (plot b) in Figure 8.3). The requirements on $cos\Theta_{\mathrm{e-T}}$, as mentioned in section 4.8, were optimized to reduce the amount of continuum events which mainly contribute at ± 1. Hence, in the region where the influence of the continuum events is suppressed ($cos\Theta_{\mathrm{miss}} < 0.7$) the behavior of $\Delta\mathcal{B}$ is very stable.

The most important variables in this analysis are E_e and $s_{\mathrm{h}}^{\mathrm{max}}$. The scans versus these variables are sensitive to the modeling of $B \to X_u e \overline{\nu}_e$ decays and also to mis-modeling of backgrounds. The measured unfolded partial branching fraction depends on the chosen $q^2 - E_e$ phase space region expressed by parameter f_u, as described in section 6.1. Therefore, for the stability scans versus E_e and $s_{\mathrm{h}}^{\mathrm{max}}$ the total branching fraction was considered:

$$\mathcal{B}\left(B\rightarrow X_u e\overline{\nu}_e\right)=\frac{N_{\text{cand}}^{\text{data}}-F_{SB}^{corr}N_{\text{bkg}}^{\text{MC}}}{2N_{B\bar{B}}F_{D^0e\nu}^{corr}\varepsilon_u}=\frac{\Delta\mathcal{B}(B\rightarrow X_u e\overline{\nu}_e)}{f_u} \tag{8.4}$$

The corresponding results are shown in Figures 8.4 and 8.5. The small variation observed in the branching fraction as a function of E_e and $s_{\text{h}}^{\text{max}}$ is clearly consistent with the statistical uncertainties.

In Figure 8.4 the behaviour of $\mathcal{B}$ has been also shown for the case if the signal efficiency correction factor is evalueted independing of the requirement on E_e in the $B\rightarrow X_u e\overline{\nu}_e$ event selection. In other plots for each scan point a separate correction factor, $F_{D^0e\nu}^{corr}$, was computed (see chapter 5).

Overall, the results of $\Delta\mathcal{B}(B\rightarrow X_u e\overline{\nu}_e)$ as well as of $\mathcal{B}(B\rightarrow X_u e\overline{\nu}_e)$ as a function of the important requirements are very stable.

8.3 Extraction of $|V_{ub}|$ and Outlook

The CKM matrix element $|V_{ub}|$ can be extracted from the partial rate, $\Delta\Gamma=\Delta\mathcal{B}(B\rightarrow X_u e\overline{\nu}_e)/\tau_B$, as

$$|V_{ub}|=\sqrt{\frac{\Delta\Gamma}{\zeta}}=\sqrt{\frac{\Delta\mathcal{B}(B\rightarrow X_u e\overline{\nu}_e)}{\zeta\tau_B}}, \tag{8.5}$$

where ζ is the normalized theoretical rate, $\Delta\Gamma/|V_{ub}|^2$, and τ_B is the average B lifetime. The computation of the theoretical rate, ζ, depends on the underlying theoretical description for inclusive $B\rightarrow X_u e\overline{\nu}_e$ decays.

In this analysis the unfolded partial branching fraction is measured in the $\Upsilon(4S)$ rest frame. This requires a corresponding computation of ζ which needs to be performed in the same rest frame as the $\Delta\mathcal{B}$ measurement. Currently, such a calculation is in progress [52] and will soon be available. Unfortunately, all other available calculations [24, 74] were performed in B rest frame. Therefore, to determine the CKM matrix element $|V_{ub}|$ an alternative $\Delta\tilde{\mathcal{B}}(B\rightarrow X_u e\overline{\nu}_e)$ (8.2) has been measured. In this analysis, the $|V_{ub}|$ determination is based on the $B\rightarrow X_u e\overline{\nu}_e$ model described in Ref. [24].

The theoretical rate, ζ, is calculated from the expressions for the triple differential $B\rightarrow X_u l\nu$ decay rate and for the $B\rightarrow X_s\gamma$ photon spectrum [75]. The leading terms in the HQE are computed at next-to-leading order, and the effects from subleading Shape Functions were including in the higher-order corrections. The heavy quark parameters, $m_b(\text{SF})=4.631^{+0.041}_{-0.035}\,\text{GeV}$ and $\mu_\pi^2(\text{SF})=0.272^{+0.056}_{-0.076}\,\text{GeV}$ were translated from the kinetic scheme to the shape-function scheme [27] from the values obtained from fits to $B\rightarrow X_c l\nu$ and $B\rightarrow X_s\gamma$ moments [76]. The theoretical rate for $\tilde{E}_e>1.9\,\text{GeV}$ and $\tilde{s}_{\text{h}}^{\text{max}}<3.5\,\text{GeV}^2$ is computed to be

$$\zeta=(16.52^{+2.07}_{-1.58}{}_{\text{HQE}}{}^{+2.05}_{-1.95}{}_{\text{theo}})\ \text{ps}^{-1}, \tag{8.6}$$

where the HQE error is due to uncertainties in the parameters m_b and μ_π^2 and the theoretical error contains uncertainties from subleading Shape Functions (3.8%), weak annihilation

(7.6%) and variation in the matching scales (9.0%). After substituting ζ and $\Delta\tilde{\mathcal{B}}$ into equation (8.5), $|V_{ub}|$ is determined to be

$$|V_{ub}| = (4.19 \pm 0.18_{\text{exp}}{}^{+0.26}_{-0.20}{}_{\text{HQE}}{}^{+0.26}_{-0.25}{}_{\text{theo}}) \times 10^{-3}, \tag{8.7}$$

where the first error refers to experimental contributions, the second to heavy quark parameter uncertainties, and the third to theoretical uncertainties in the calculation of the rate ζ.

The obtained result for $|V_{ub}|$ is in very good agreement with previous determinations and is consistent with result calculated as average from input of various experiments, as shown in Figure 8.6. The $q^2 - E_e$ approach, compared to the other analysis methods (e. g. hadronic mass or endpoint analyses), results in higher sensitivity to the effects of the subleading SF and weak annihilation due to the portion of the $B \to X_u e \overline{\nu}_e$ phase space probed. As a consequence, the $|V_{ub}|$ result obtained in this analysis has larger theoretical uncertainty, whereas the experimental error is significantly smaller compared with results from other analysis methods. Once the calculation of the rate ζ for different E_e and $s_{\mathrm{h}}^{\mathrm{max}}$ in the $\Upsilon(4S)$ rest frame will become available, the CKM matrix element $|V_{ub}|$ can be determined for each measured partial branching fraction from Table 8.2. The final result for $|V_{ub}|$ will then quoted by analysing the experimental and theoretical uncertainties and choosing the $|V_{ub}|$ value with smallest total uncertainty.

The determination of $|V_{ub}|$ is limited primarily by the precision of calculated theoretical rate ζ. The corresponding theoretical uncertainties can be reduced using larger $B \to X_u e \overline{\nu}_e$ phase-space region for the extraction of the partial branching fraction. Furthermore, the theoretical comunity is very active and new results are being published continuously. Hence, the set of results (see Table 8.2) obtained in this analysis provides the full experimental input for a future determination of $|V_{ub}|$ from improve theoretical calculations.

a)

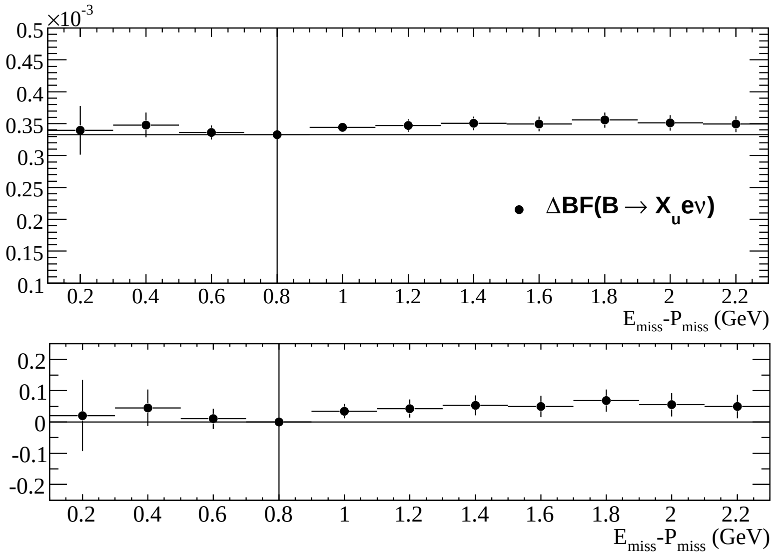

b)

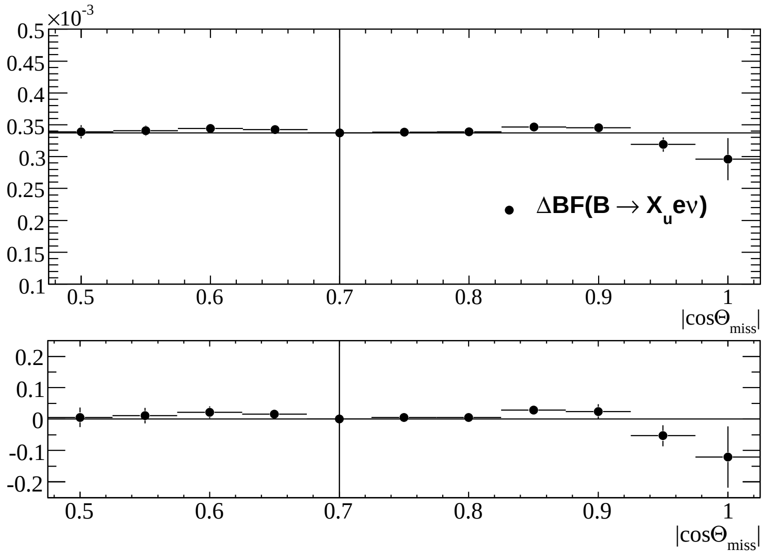

Figure 8.1: The behavior of the partial branching fraction measurement (solid points) as a function of a) the bound on $E_{\mathrm{miss}} - |P_{\mathrm{miss}}|$ and b) the bound on $|cos\Theta_{\mathrm{miss}}|$. The relative differences with respect to the nominal requirements (denoted by a vertical line) are shown in the lower plots. The errors are purely statistical and were computed from the residual difference in the yields with respect to the nominal values.

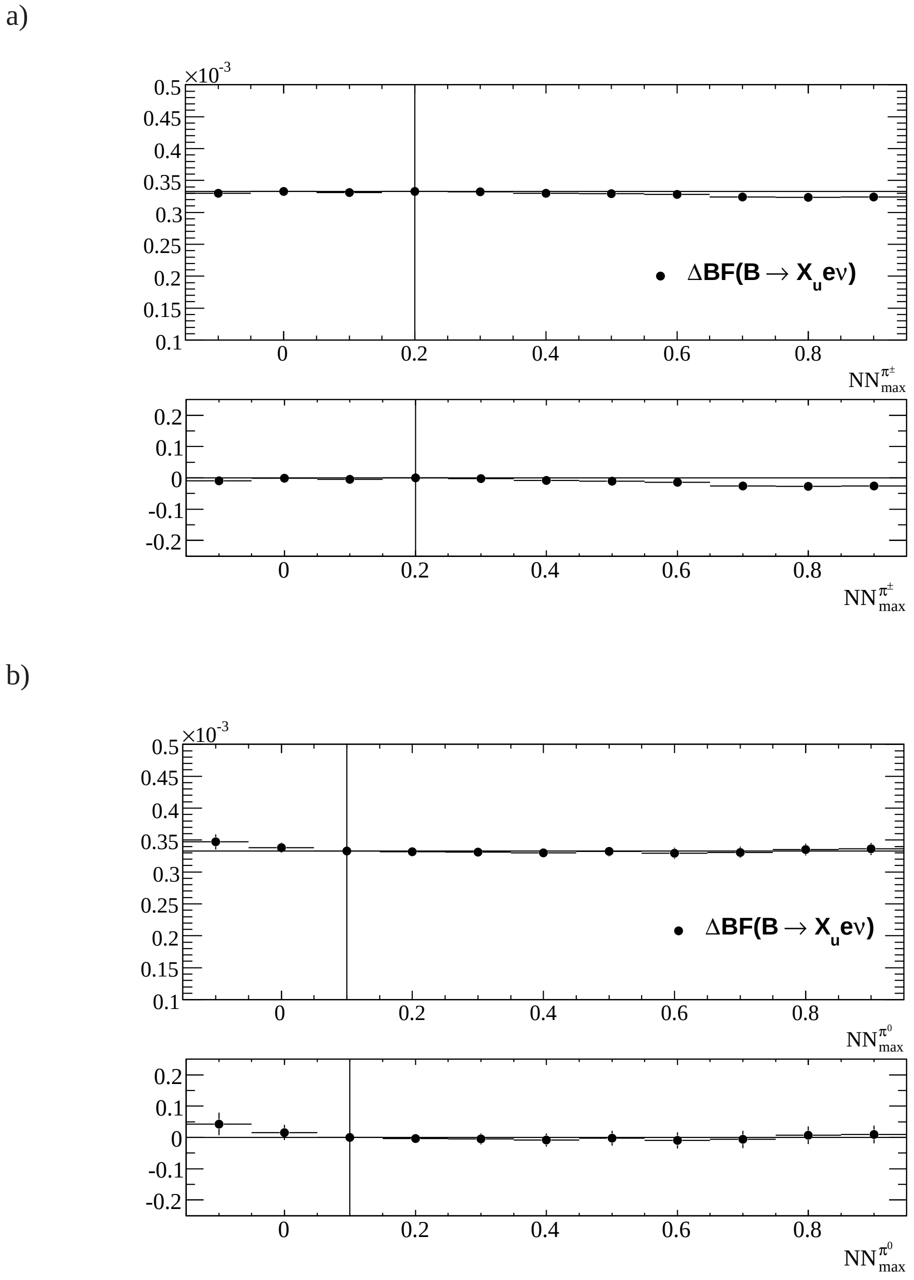

Figure 8.2: The behavior of the partial branching fraction measurement (solid points) as a function of a) the upper bound on $NN^{\pi^\pm}_{\text{max}}$ and b) the upper bound on $NN^{\pi^0}_{\text{max}}$. The plots follow the same conventions as those of figure 8.1.

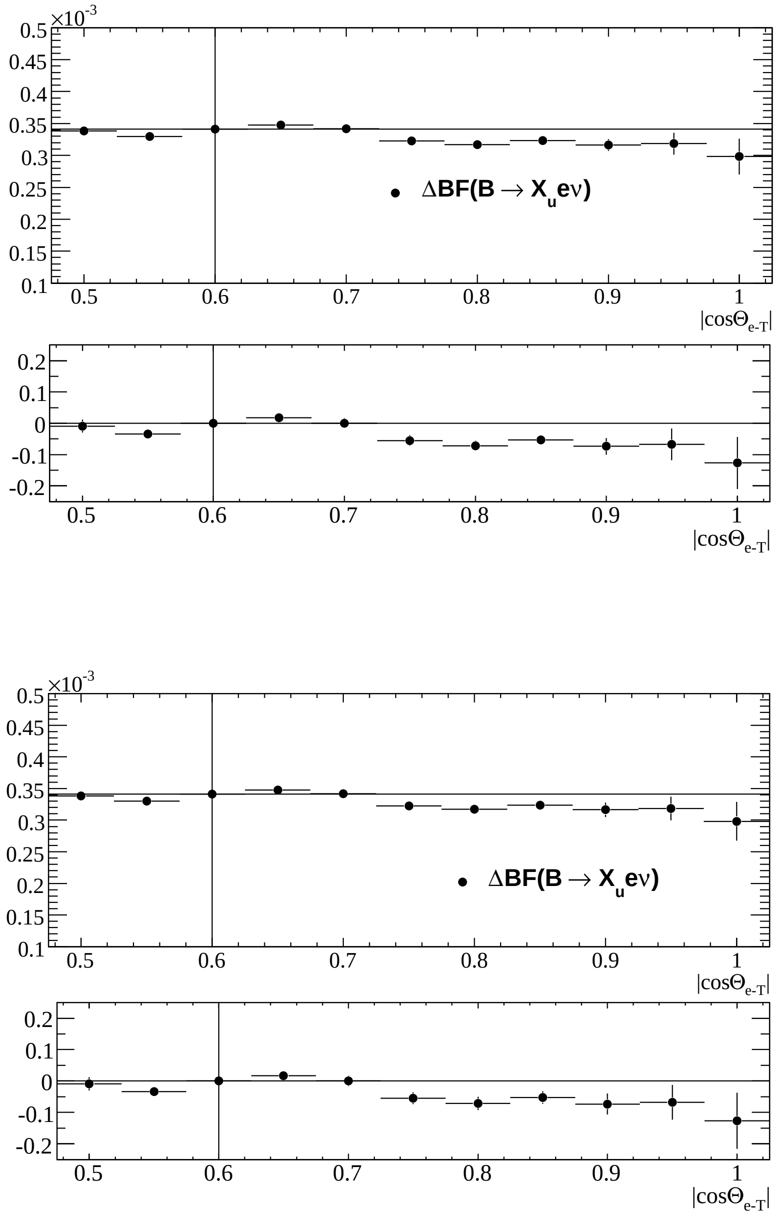
a)

b)

Figure 8.3: The behavior of the partial branching fraction measurement (solid points) as a function of $|cos\Theta_{\mathrm{e-T}}|$ a) icluding only uncorrelated statistical uncertainties and b) including uncorrelated statistical as well as the systematic uncertainties. The errors shown are computed for each scan point with respect to the errors of the nominal values.

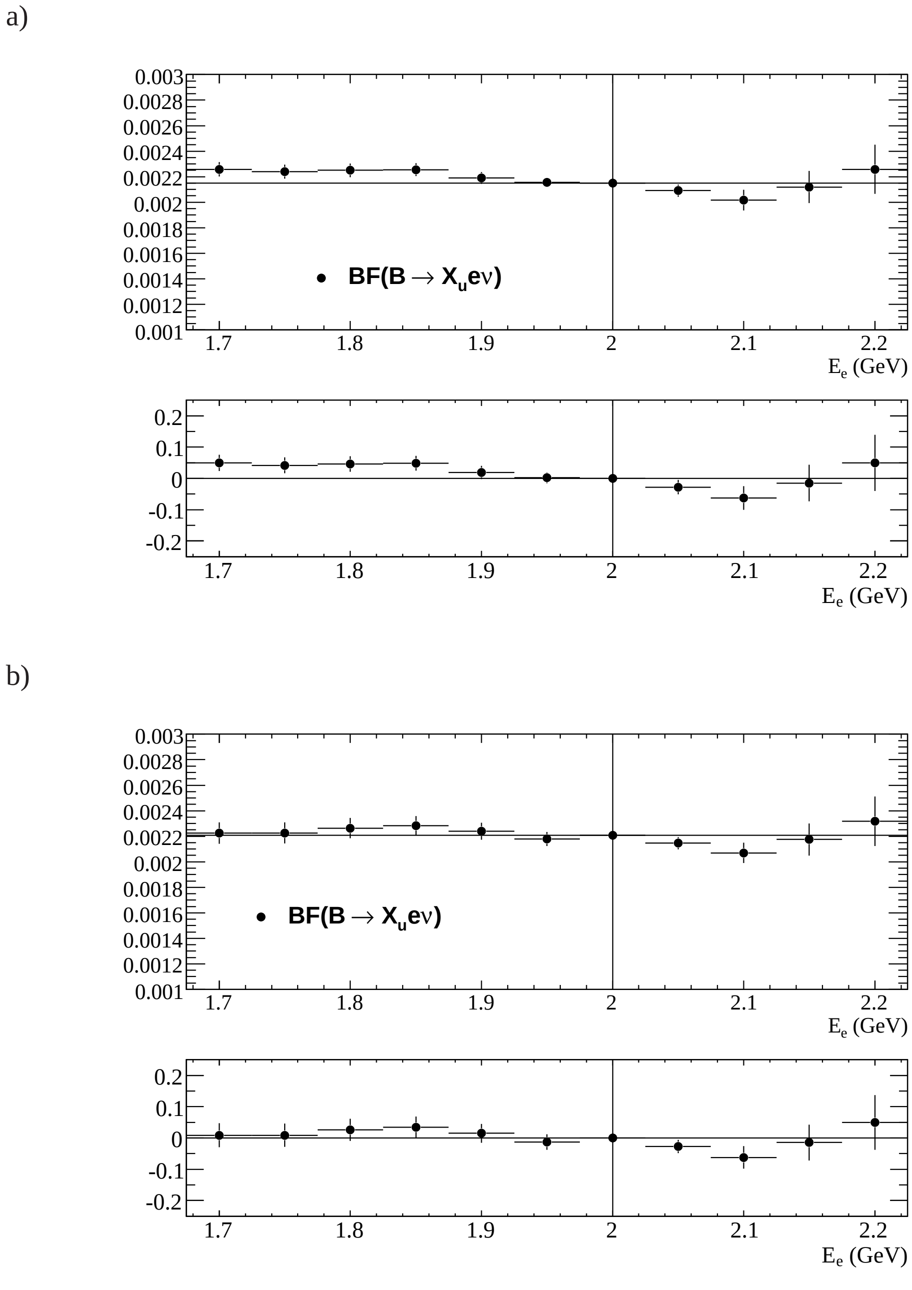

Figure 8.4: The behavior of the $B \to X_u e \overline{\nu}_e$ branching fraction ($\mathcal{B} = \Delta\mathcal{B}/f_u$) measurement (solid points) as a function of the lower bound on E_e a) using only one signal effciency correction factor obtained for $E_e > 1.4\,\mathrm{GeV}$ and b) using signal efficiency correction factors computed for each scan point, as described in section 5.3. These plots follow the same convention as those of figure 8.1.

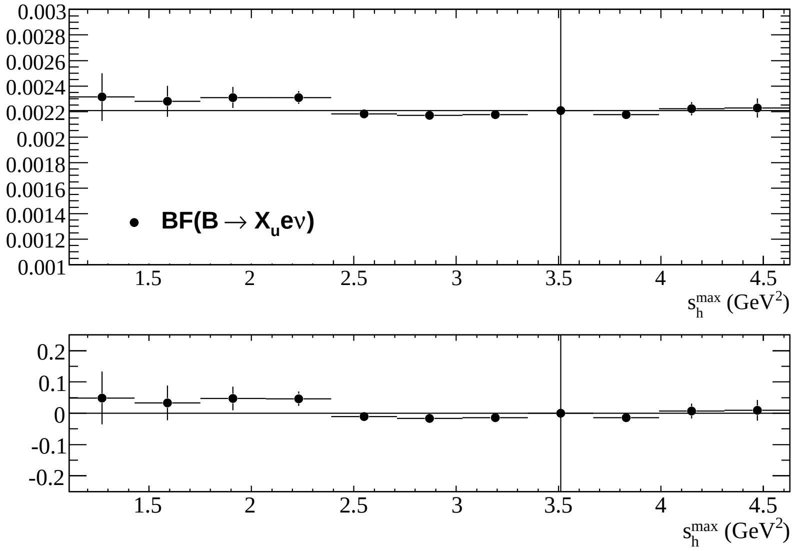

Figure 8.5: The behavior of the $B \to X_u e \overline{\nu}_e$ branching fraction ($\mathcal{B} = \Delta\mathcal{B}/f_u$) measurement (solid points) as a function of the upper bound on $s_{\mathrm{h}}^{\mathrm{max}}$. These plots follow the same convention as those of figure 8.1.

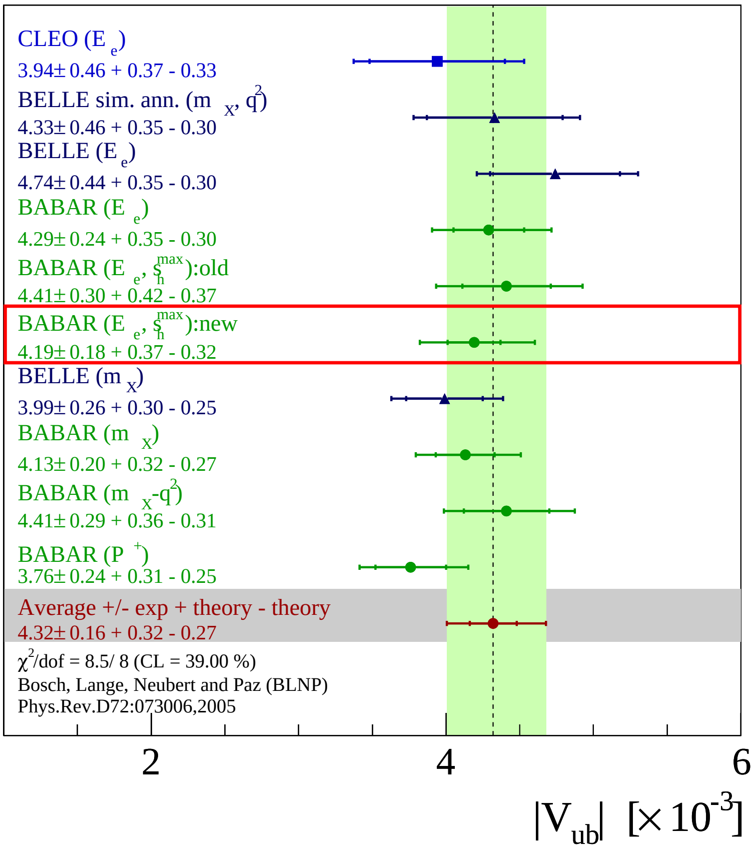

Figure 8.6: Comparison between inclusive $|V_{ub}|$ determinations based on the $B \longrightarrow X_u e \overline{\nu}_e$ model described in Ref. [24]. The $|V_{ub}|$ value obtained in this analysis is denoted as "new" and is surrounded by a red box. The previous $|V_{ub}|$ determination using $q^2 - E_e$ approach is labeled as "old". All shown $|V_{ub}|$ values correspond to the latest HFAG [76] results and are determined using as input the heavy quark parameter $m_b(\mathrm{SF}) = 4.631^{+0.041}_{-0.035}$ GeV and $\mu_\pi^2(\mathrm{SF}) = 0.272^{+0.056}_{-0.076}$ GeV obtained from global fit to both the $B \longrightarrow X_c l \nu$ and $B \longrightarrow X_s \gamma$ moments. The result from this analysis was not included in the average.

9 Summary and Conclusion

A measurement of the partial branching fraction, $\Delta\mathcal{B}(B \to X_u e \overline{\nu}_e)$, and the CKM matrix element $|V_{ub}|$ was presented. The results obtained are in very good agreement with previous inclusive $|V_{ub}|$ determinations in particular with the $|V_{ub}|$ value determined in a prevoius analyisis [1].

This analysis is based on a data sample of 454.2 million $B\overline{B}$ pairs collected with the BABAR detector at the PEP-II asymmetric energy e^+e^--storage rings. Inclusive semileptonic $B \to X_u e \overline{\nu}_e$ decays are identified using $q^2 - E_e$ technique reconstructing the electron energy, E_e, and the invariant mass squared of the electron-neutrino pair, q^2. The final hadronic state, X_u, consists of a sum of many hadronic channels, each of which contains at least one u quark. The neutrino kinematics is deduced from the decay products of both B mesons.

The dominant $b \to c$ background was suppressed by selecting the $q^2 - E_e$ phase space region where the production of $B \to X_c l \nu$ events is kinematically suppressed. In addition, a special technique is developed to identify and to remove $B \to D^* \ell \nu$ decays which represent the main part of the $B \to X_c l \nu$ background. The remaining $B\overline{B}$ background contribution is subtracted using Monte Carlo simulation.

Various sources of systematic uncertainties associated with the measurement of the $B \to X_u e \overline{\nu}_e$ partial branching fraction are investigated. The main contribution arises from the impact of the reconstruction efficiencies for neutral and charged particles, and the uncertainties on the branching fraction of inclusive D decays.

The partial branching fraction was measured in the $\Upsilon(4S)$ rest frame to be

$$\Delta\mathcal{B}(E_e > 2.0\,\text{GeV}, s_\text{h}^\text{max} < 3.52\,\text{GeV}^2) = (3.33 \pm 0.18_\text{stat} \pm 0.21_\text{syst}) \times 10^{-4}$$

The corresponding $\Delta\tilde{\mathcal{B}}$ in B meson rest frame was evaluated to be

$$\Delta\tilde{\mathcal{B}}(\tilde{E}_e > 1.9\,\text{GeV}, \tilde{s}_\text{h}^\text{max} < 3.5\,\text{GeV}^2) = (4.57 \pm 0.24_\text{stat} \pm 0.32_\text{syst}) \times 10^{-4}$$

The CKM matrix element $|V_{ub}| = \sqrt{\Delta\tilde{\mathcal{B}}/(\zeta\tau_B)}$ is determined based on the $B \to X_u e \overline{\nu}_e$ model described in Ref. [24], in which the theoretical rate, ζ, is calculated from the expressions for the triple differential $B \to X_u l \nu$ decay rate and for the $B \to X_s \gamma$ photon spectrum. The leading terms in the HQE are computed at next-to-leading order, and the effects from subleading Shape Functions were included in the higher-order corrections. The heavy quark parameters, $m_b(\text{SF}) = 4.631^{+0.041}_{-0.035}\,\text{GeV}$ and $\mu_\pi^2(\text{SF}) = 0.272^{+0.056}_{-0.076}\,\text{GeV}$ were translated to the shape-function scheme [27] from coresponding values obtained from fits to $B \to X_c l \nu$ and $B \to X_s \gamma$ moments [76]. Using the calculated rate, ζ, and the measured partial branching fraction, $\Delta\tilde{\mathcal{B}}$, $|V_{ub}|$ was determined to be

$$|V_{ub}| = (4.19 \pm 0.18_\text{exp}{}^{+0.26}_{-0.20}{}_\text{HQE}{}^{+0.26}_{-0.25}{}_\text{theo}) \times 10^{-3},$$

where the first error refers to experimental contributions, the second to heavy quark parameter uncertainties, and the third to theoretical uncertainties in the calculation of the rate ζ. As the theoretical community is very active and new results are being published continuously, the presented branching fraction results with relative small experimental uncertainties can be used to extract $|V_{ub}|$ in the future with more precision. In particular, some systematic uncertainities such as the tracking and photon efficiency uncertainties can still be reduced and the requirements on E_e and $s_{\mathrm{h}}^{\max}$ can be then relaxed to $E_e > 1.7\,\mathrm{GeV}$ and $s_{\mathrm{h}}^{\max} < 4.0\,\mathrm{GeV}^2$. This will be also result in smaller theoretical uncertainties.

Bibliography

[1] Fortin, D. *et al.*, *Measurement of* $|V_{ub}|$ *from semileptonic B decays using the lepton energy and* q^2, *BABAR* Analysis Document 664.

[2] Glashow, S. L., *Partial Symmetries of Weak Interactions*, Nucl. Phys. 22(1961):579–588.

[3] Weinberg, S., *A Model of Leptons*, Phys. Rev. Lett. 19(1967)(21):1264–1266.

[4] Salam, A., *Weak and Electromagnetic Interactions* (1968), Originally printed in *Svartholm: Elementary Particle Theory, Proceedings Of The Nobel Symposium Held 1968 At Lerum, Sweden*, Stockholm 1968, 367-377.

[5] Griffiths, D. J., *Introduction to Elementary Particles* (John Wiley & Sons, Inc., New York, 1987), ISBN 3-05-501627-0.

[6] Schmüser, P., *Feynman-Graphen und Eichtheorien für Experimentalphysiker* (Springer-Verlag, Berlin, Germany / Heidelberg, Germany / London, UK / etc., 1988), ISBN 3-540-18797-9.

[7] Higgs, P. W., *Broken Symmetries, Massless Particles and Gauge Fields*, Phys. Lett. 12(1964):132–133.

[8] Higgs, P. W., *Broken Symmetries and the Masses of Gauge Bosons*, Phys. Rev. Lett. 13(1964):508–509.

[9] Higgs, P. W., *Spontaneous Symmetry Breakdown Without Massless Bosons*, Phys. Rev. 145(1966):1156–1163.

[10] Wolfenstein, L., *Parametrization of the Kobayashi-Maskawa Matrix*, Phys. Rev. Lett. 51(1983):1945.

[11] Barberio, E. *et al.*, (Heavy Flavor Averaging Group (HFAG)), *Results on Time-Dependent CP Violation, and Measurements Related to the Angles of the Unitarity Triangle: Summer 2008 (ICHEP2008, USA and CKM2008, Italy)*. Available from: `http://www.slac.stanford.edu/xorg/hfag/triangle/summer2008/index.shtml`.

[12] Charles, J. *et al.*, (CKMfitter Group), *CP Violation and the CKM Matrix: Assessing the Impact of the Asymmetric B Factories*, Eur. Phys. J. C 41(2005):1–131, hep-ph/0406184. Available from: `updatedresultsandplotsat:http://ckmfitter.in2p3.fr/`.

[13] Scora, D. and Isgur, N., *Semileptonic Meson Decays in the Quark Model: An Update*, Phys. Rev. D52(1995):2783, hep-ph/9503486.

[14] Neubert, M., *Heavy Quark Symmetry*, Phys. Rept. 245(1994):259, hep-ph/9306320.

[15] Richman, J. and Burchat, P., *Leptonic and Semileptonic Deacys of Charm and Bottom Hadrons*, Rev. Mod. Phys. 67(1995):893, hep-ph/9508250.

[16] Caprini, I., Lellouch, L., and Neubert, M., *Dispersive Bounds on the Shape of* $B \to D^{(*)} l \nu$ *Form Factors*, Nucl. Phys. B530(1998):153, hep-ph/9712417.

[17] Hashimoto, S. *et al.*, Phys. Rev. D66(2002):014503.

[18] Manohar, A. V. and Wise, M. B., Phys. Rev. D49(1994):1310.

[19] Block, B., *et al.*, Phys. Rev. D49(1994):3356.

[20] Neubert, M., Phys. Rev. D49(1994):3392.

[21] Bauer, C. W. and Manohar, A. V., Phys. Rev. D70(2004):034024.

[22] Buchmüller, O. and Flächer, H., *Fit to Moments of Inclusive* $B \to X_c \ell \nu$ *and* $B \to X_s \gamma$ *Decay Distributions using Heavy Quark Expansions in the Kinetic Scheme*, Phys. Rev. D 73(2006):073008, hep-ph/0507253.

[23] Fazio, F. D. and Neubert, M., JHEP 06(1999):017.

[24] Lange, B. O., Neubert, M., and Paz, G., *Theory of Charmless Inclusive B Decays and the Extraction of* V_{ub}, Phys. Rev. D 72(2005):073006, hep-ph/0504071.

[25] Kagan, A. L. and Neubert, M., *(GEANT4 Collab.)*, Eur. Phys. J. C7(1999):5.

[26] Lange, B. O., Neubert, M., and Paz, G., Nucl. Phys. B699(2004):335, hep-ph/0402094.

[27] Neubert, M., *Theory of Charmless Inclusive B Decays and the Extraction of* V_{ub}, Phys. Lett. B612(2005):13.

[28] Kowalewski, R. and Menke, S., Phys. Lett. B541(2002):29.

[29] Harrison, P. F., e. and Quinn, Helen R., e., (BABAR Collaboration), *The BABAR physics book: Physics at an asymmetric B factory*, SLAC-R-504 (1998), Papers from Workshop on Physics at an Asymmetric B Factory (BaBar Collaboration Meeting), Rome, Italy, 11-14 Nov 1996, Princeton, NJ, 17-20 Mar 1997, Orsay, France, 16-19 Jun 1997 and Pasadena, CA, 22-24 Sep 1997.

[30] Aubert, B. *et al.*, (BABAR Collaboration), *A Measurment of the Total Width, the Electronic WIdth, and the Mass of the* $\Upsilon(10580)$ *Resonance*, SLAC-PUB-10439 .

[31] Aubert, B. *et al.*, (BABAR Collaboration), *The BaBar Detector*, Nucl. Instrum. Meth. A 479(2002):1–116, hep-ex/0105044.

[32] Benelli, G., *et al.*, *The BABAR LST Detector High Voltage System: Design and Implementation*, IEEE Nucl. Sci. Symp. Conf. Rec. 2(2006):1145–1148.

[33] Agostinelli, S. *et al.*, *(GEANT4 Collab.)*, Nucl. Instr. Meth. A506(2003):250.

[34] Barberio, E. *et al.*, (Heavy Flavor Averaging Group (HFAG)), *Updates of Semileptonic Results for PDG 2008* (Summer 2008). Available from: `http://www.slac.stanford.edu/xorg/hfag/semi/pdg08/home.shtml`.

[35] *BABAR* Collaboration, *Semileptonic Analysis Working Group*. Available from: `http://babar-hn.slac.stanford.edu:5090/HyperNews/get/semi_lept_decays/769.html`.

[36] Sjostrand, T., Comput. Phys. Commun. 82(1994):74.

[37] Volk, A., *WebTool*. Available from: `https://babar.fzk.de:5090/~volk/`.

[38] Aubert, B. *et al.*, (*BABAR* Collaboration), *Measurements of the Semileptonic Decays $\bar{B} \to D\ell\bar{\nu}$ and $\bar{B} \to D^*\ell\bar{\nu}$ Using a Global Fit to $DX\ell\bar{\nu}$ Final States* (2008), arXiv:0809.0828 [hep-ex].

[39] Fox, G. and Wolfram, S., Nucl. Phys. B149(1979):413.

[40] Aubert, B. *et al.*, Phys. Rev. D67(2003):031101.

[41] Aubert, B. *et al.*, (*BABAR* Collaboration), *Measurement of the Inclusive Electron Spectrum in Charmless Semileptonic B Decays Near the Kinematic Endpoint and Determination of $|V_{ub}|$*, Phys. Rev. D73(2006):012006, hep-ex/0509040.

[42] Pegna, D. L. *et al.*, *TrkFixup: using the Mini to improve the quality of BaBar tracks used in analysis*, *BABAR* Analysis Document 1628.

[43] Fortin, D. *et al.*, *Particle selection criteria optimized for visible energy measurement*, *BABAR* Analysis Document 633.

[44] M.Mazur and J.Richman, *Measurement of the exclusive branching fractions $B \to D^{(*)}\tau\nu$*, *BABAR* Analysis Document 1111.

[45] Drescher, A. *et al.*, Nucl. Instr. Meth. A237(1985):464.

[46] *BABAR* Collaboration, *Standard Reconstruction Software*. Available from: `http://slac.stanford.edu/BFROOT/dist/releases/current/SimpleComposition/SmpJPsiProdSequence.tcl`.

[47] *BABAR* Collaboration, *Particle ID group*. Available from: `http://www.slac.stanford.edu/BFROOT/www/Physics/Tools/Pid/Selectors/r18a/PidLHElectronSelector_details.html`.

[48] *BABAR* Collaboration, *Particle ID group*. Available from: `http://www.slac.stanford.edu/BFROOT/www/Physics/Tools/Pid/Selectors/r18a/VeryTightNNKaonMicroSelection_details.html`.

[49] *BABAR* Collaboration, *Particle ID group*. Available from: `http://www.slac.stanford.edu/BFROOT/www/Physics/Tools/Pid/Selectors/r18a/NNVeryTightMuonSelection_details.html`.

[50] BABAR Collaboration, *Particle ID group*. Available from: `http://www.slac.stanford.edu/BFROOT/www/Physics/Tools/Pid/Selectors/r18a/VeryTightLHProtonSelection_details.html`.

[51] *TMVA Toolkit for Multivariate Data Analysis with ROOT*. Available from: `http://tmva.sourceforge.net/`.

[52] Tackmann, F., private communication.

[53] Amsler, C. *et al.*, (Particle Data Group (PDG)), *Review of Particle Physics*, Physics Letters B 667(2008):1. Available from: `http://pdg.lbl.gov`.

[54] Lopes Pegna, D. and Lüth, V., (Semileptonic Analysis Working Group (BABAR)), *$B \to X_c \ell \nu$ Reweighting 2007* (August 2007), Corrections made on the second url. Available from: `http://www.slac.stanford.edu/BFROOT/www/Physics/Analysis/AWG/Semileptonic/Reweighting2007.html,http://babar-hn.slac.stanford.edu:5090/HyperNews/get/semi_lept_decays/779.html`.

[55] Aubert, B. *et al.*, (BABAR Collaboration), *Determination of $|V_{ub}|$ from Measurements of the Electron and Neutrino Momenta in Inclusive Semileptonic B Decays*, Phys. Rev. Lett. 98(2007):0911801, hep-ex/0612020.

[56] Aubert, B. *et al.*, (BABAR Collaboration), *Determination of the form factors for the decay $B^0 \to D^{*-} l^+ \nu_l$ and of the CKM matrix element $|V_{cb}|$*, Phys. Rev. D77(2008):032002.

[57] *Tracking Efficiency Task Force [R22/SP8]* (Summer 2007). Available from: `http://www.slac.stanford.edu/BFROOT/www/Physics/TrackEfficTaskForce/TrackingTaskForce-2007-R22.html`.

[58] *Tau31 Tracking Efficiency Study For 2004*, BABAR Analysis Document 931.

[59] *Soft Pion Study*. Available from: `http://www.slac.stanford.edu/BFROOT/www/Organization/CollabMtgs/2007/detFeb07/Thur3/lopes.pdf`.

[60] Allen, M. *et al.*, *A Measurement of π^0 Efficiency Using $\tau \to \rho \nu$ and $\tau \to \pi \nu$ Decays* (2004), BABAR Analysis Document #870.

[61] BABAR Collaboration, *Particle ID group*. Available from: `http://www.slac.stanford.edu/BFROOT/www/Physics/Tools/Pid/pid.html`.

[62] Bona, M., Cavoto, G., *et al.*, *A study of K_L identification and efficiencies*, BABAR Analysis Document 1191.

[63] Brandt, T. and Lüth, V., *Measurement of Iclusive Lepton Spectrum in B Meson Decay and Determination of Semileptonic Branching Ration and $|V_{cb}|$* , BABAR Analysis Document 216.

[64] J. Dingfelder, M. K., private communication.

[65] Eckmann, R. and Schwitters, R., *Measurement of the branching fraction of charmless semi-leptonic B-decays and determination of |Vub| using the kaon multiplicity distribution to subtract the charm background*, *BABAR* Analysis Document 1297.

[66] Brandt, T. and Schubert, K. R., *Measurement of the Inclusive Electron Spectrum, Moments and Branching Fraction for Semileptonic B meson Decays*, *BABAR* Analysis Document 636.

[67] Bernlochner, F., *et al.*, *On the effects of additional Bremsstrahlung due detector geometry uncertainties on Monte Carlo simulated electron energy spectra*, *BABAR* Analysis Document 1911.

[68] Richter-Was, E., Phys. Lett. B303(1993):163.

[69] Dingfelder, J. (July 13, 2007), *BABAR* Hypernews Forum for Review of SemiLep-03/02. Available from: `http://babar-hn.slac.stanford.edu:5090/HyperNews/get/rev-SemiLep-03-02/30/1.html`.

[70] Bernlochner, F., *et al.*, *On the QED radiative corrections of semileptonic B decays*, *BABAR* Analysis Document 2022.

[71] Golubev, V., *Beam Energy Correction to MC*, *BABAR* Collaboration talk. Available from: `http://www.slac.stanford.edu/BFROOT/www/Organization/CollabMtgs/2008/detOct08/Tues1a/vladimir.pdf`.

[72] Hearty, C., *Hadronic Event Selection and B-Counting for Inclusive Charmonium Measurements*, *BABAR* Analysis Document 30.

[73] Fortin, D., *Determination of the CKM element* $|V_{ub}|$, Dissertation, Univesity of Victoria (2005).

[74] Andersen, J. and Gardi, E., *Inclusive spectra in charmless semileptonic B decays by Dressed Gluon Exponentiation*, JHEP 0601(2006):097, hep-ph/0509360.

[75] Nuebert, M., *Mathematica Notebook*. Available from: `http://www.slac.stanford.edu/BFROOT/www/Physics/Analysis/AWG/Semileptonic/InclusiveBeauty_v1.1.nb`.

[76] Barberio, E. *et al.*, (Heavy Flavor Averaging Group (HFAG)), *Updates of Semileptonic Results for ICHEP08 2008*. Available from: `http://www.slac.stanford.edu/xorg/hfag/semi/ichep08/gbl_fits/kinetic/index.html`.

Danksagung

An dieser Stelle möchte ich mich beim Prof. Dr. Schubert und Prof. Dr. Michael Kobel bedanken, die es mir ermöglicht haben, im Rahmen der *BABAR* Kollaboration meine Doktorarbeit anzufertigen.

Ein ganz besonderer Dank geht an Prof. Dr. Lacker, der eigentlicher Initiator der Analyse und die jenige Person, die mich im Laufe der Jahre sehr intensiv betreut hat und immer wieder mit Rat und Tat mir zur Seite stand.

Ausserdem bedanke ich mich beim Dr. Rainer Schwierz fü die Betreuung und Wartung der Institutsrechner. Beim ZIH Supporting-Team bedanke ich mich fü eine grossartige Untestützung, die mir esrt ermöglicht hat, meine Analyse am optimalsten zu gestalten.

Versicherung

Hiermit versichere ich, dass ich die vorliegende Arbeit ohne unzulässige Hilfe Dritter und ohne Benutzung anderer als der angegebenen Hilfsmittel angefertigt habe; die aus fremden Quellen direkt oder indirekt übernommenen Gedanken sind als solche kenntlich gemacht. Die Arbeit wurde bisher weder im Inland noch im Ausland in gleicher oder ähnlicher Form einer anderen Prüfungsbehörde vorgelegt.

Die vorliegende Arbeit wurde am Institut für Kern- und Teilchenphysik der Technischen Universität Dresden unter wissenschaftlicher Betreuung von Prof. Dr. Michael Kobel angefertigt.

Es haben keine früheren erfolglosen Promotionsverfahren stattgefunden.

Ich erkenne die Promotionsordnung der Fakultät Mathematik und Naturwissenschaften an der Technischen Universität Dresden vom 20. März 2000, in der Fassung der vom Fakultätsrat am 19.06.2002 und 12.07.2002 beschlossenen und mit Erlass des Sächsischen Staatsministeriums für Wissenschaft und Kunst vom 18.03.2003 genehmigten Änderungen gemäß Satzung vom 16.04.2003, an.

Dresden, den 08.04.2009

Alexei Volk